SEARCH FOR THE FAMILON IN TWO-BODY B MESON DECAYS

By

István Dankó

Dissertation

Submitted to the Faculty of the

Graduate School of Vanderbilt University

in partial fulfillment of the requirements

for the degree of

DOCTOR OF PHILOSOPHY

in

Physics

December, 2001

Nashville, Tennessee

Approved

Prof. Steven E. Csorna

Prof. Thomas W. Kephart

Prof. Paul D. Sheldon

Prof. Norman H. Tolk

Prof. Thomas J. Weiler

Szüleimnek a támogatásukért;

feleségemnek, Andreának, és

gyermekeimnek, Dórának és Dávidnak

a szeretetükért és bátorításukért.

ACKNOWLEDGMENTS

First of all, I would like to express my gratitude to my adviser, Steven Csorna, for his guidance and encouragement throughout my graduate years at Vanderbilt University. He introduced me to B meson physics, taught me a lot about experimental particle physics and helped me to find the research topic that turned into this dissertation. He has been always very supportive not only in my work but in many other aspects of my life during the years my family and I spent in Nashville, TN.

I indebted to many people, teachers and colleagues, who were instrumental in my education and shaped my career from elementary school to graduate school. I am also thankful to my fellow graduate students, Szabolcs Márka and his wife Zsuzsa who have been good friends for many years since high school; and influenced me to come to Vanderbilt to pursue a graduate degree in particle physics. They helped me through the first couple of months in Nashville, when I had to miss my family; and the long study sessions with Zsuzsa made it much easier for me to complete the core classes and prepare for the qualifying exam successfully.

I fail to find words to express my gratitude to my parents, especially to my mother, for their continued support and encouragement. I would also like to thank my wife, Andrea, who always has supported whatever ambitions I have pursued, helped me in the bad times and shared many wonderful times with me. I am truly blessed to have my wonderful children, Dóra and Dávid, who have brought lots of fun, laughter and happiness to my life.

This work would not have been possible without the CLEO collaboration. I acknowledge the effort of all my CLEO colleagues who built and improved the detector; developed and maintained the analysis software library. I am grateful to my paper committee and Karl

Ecklund who provided valuable advice and helped shepherd this analysis into its final form. The hard work of all staff members in the Cornell Electron Storage Ring was inevitable in order to provide us with excellent luminosity and running conditions.

This work was supported by a grant from the National Science Foundation. I would also like to thank the Soros Foundation-Hungary for providing partial financial support during the first two years of my graduate study.

TABLE OF CONTENTS

LIST OF TABLES

LIST OF FIGURES

CHAPTER I

THE STANDARD MODEL

I.1 The elementary particles

According to our present knowledge, the world around us is built up from a few elementary particles, which are hold together by four basic interactions [1]. The building blocks are spin-$\frac{1}{2}$ fermions of two types: quarks and leptons, while the interactions are transmitted by bosons with integer spin. These particles are regarded elementary in the sense that they are point like without internal structure[1] up to the present limit of $10^{-18} - 10^{-19}$ m.

The known leptons are the electron (e^-), the muon (μ^-) and the tau-lepton (τ^-) with electric charge[2] $Q = -1$, and the corresponding neutrinos ν_e, ν_μ and ν_τ with electric charge $Q = 0$. The six leptons can be arranged into three families or generations:

$$\begin{pmatrix} \nu_e \\ e^- \end{pmatrix} \qquad \begin{pmatrix} \nu_\mu \\ \mu^- \end{pmatrix} \qquad \begin{pmatrix} \nu_\tau \\ \tau^- \end{pmatrix}$$

Each generation of leptons is associated with a conserved quantum number, the lepton number (L_e, L_μ, L_τ), which is $+1$ for leptons and -1 for anti-leptons. The properties of leptons are summarized in Table. I.1.

The existence of a non-zero neutrino mass is a long standing question in particle physics. In the last couple of years, researchers at the Super-Kamiokande detector in Japan and the Sudbury Neutrino Observatory in Canada achieved a major breakthrough at this front by finding evidence for the flavor oscillation of neutrinos produced in the upper atmosphere [2]

[1] However, there are attempts to describe the quarks and leptons as composites of more fundamental ingredients, such as preons, in order to better understand some of their properties.

[2] All charges are given in units of the elementary charge $e = 1.6 \times 10^{-19}$C.

Table I.1: The properties of leptons.

Name	Spin [$\hbar$]	Charge [e]	L_e	L_μ	L_τ	Mass [MeV/c^2]
e^-	1/2	-1	1	0	0	0.511
ν_e	1/2	0	1	0	0	~ 0
μ^-	1/2	-1	0	1	0	105.6
ν_μ	1/2	0	0	1	0	< 0.17
τ^-	1/2	-1	0	0	1	1777
ν_τ	1/2	0	0	0	1	< 18.2

and in the sun [3], respectively. Since the effect depends on the difference in the squared mass of the neutrino species involved in the oscillation, this result implies a non-zero but tiny mass for the neutrinos.

Like the leptons, the quarks also have six different types or flavors. They are called up (u), down (d), charm (c), strange (s), top (t) and bottom (b) and can be also arranged into three generations:

$$\begin{pmatrix} u \\ d \end{pmatrix} \qquad \begin{pmatrix} c \\ s \end{pmatrix} \qquad \begin{pmatrix} t \\ b \end{pmatrix}$$

The electric charge of the up-type quarks (u, c, t) is $Q = +2/3$, while the down-type quarks (d, s, b) have $Q = -1/3$. The quarks have a conserved quantum number analog to the lepton number called baryon number (B), which is $B = 1/3$ for quarks and $B = -1/3$ for anti-quarks without distinction between the generations. The quarks have an additional degrees of freedom, the color, which can be of three types. The color was first proposed as an ad hoc quantum number in order to solve the problem related to the existence of hadrons, such as $\Delta^{++} \sim \mid uuu >$, built up from the same quarks having symmetric space-flavor-spin wavefunction in apparent contradiction with the Pauli principle but later they proved to be more fundamental as the source of the strong interaction. Properties of the quarks are

shown in Table I.2. In addition to the 12 fermions there are 12 corresponding antiparticles associated with each of them.

Table I.2: The properties of quarks.

Name	Spin [$\hbar$]	Charge [e]	B	Mass [MeV/c^2]
u	$1/2$	$2/3$	$1/3$	~ 5
d	$1/2$	$-1/3$	$1/3$	~ 7
c	$1/2$	$2/3$	$1/3$	1270 ± 50
s	$1/2$	$-1/3$	$1/3$	150 ± 30
t	$1/2$	$2/3$	$1/3$	$(174 \pm 17) \times 10^3$
b	$1/2$	$-1/3$	$1/3$	4250 ± 100

In contrast to the leptons, all evidence point to the fact that quarks can not exist as isolated free particles in nature but they are confined into the experimentally observed matter particles, the hadrons. Hadrons are colorless (color singlet) particles consisting of either three quarks with different colors ($\mid qqq >$), called baryons, or a quark and anti-quark ($\mid q\bar{q} >$), called mesons. From the properties of the quarks, it follows that all hadrons have integer electric charge ($Q = 0, \pm 1, \pm 2$), and that the baryons have half-integer spin ($S = 1/2$ or $S = 3/2$) and $B = 1$ baryon number (or $B = -1$ for anti-baryons), while the mesons have integer spin ($S = 0$: pseudoscalar or $S = 1$: vector) and $B = 0$ baryon number.

The four fundamental interactions are the gravitational, electromagnetic, weak and strong forces. In classical physics, these interactions are mediated by a continuous physical entity, called field, which has momentum, energy and other properties. Apart from the gravitational field[3], the other three interaction fields can be quantized in terms of creation and destruction

[3]Gravity is different from the other three interactions since the gravitational "field" is the feature of the space-time and lacks the properties characteristic for the other fields. Therefore, attempts to quantize the

operators in quantum field theory and the interaction can be interpreted as the exchange of spin-1 bosons (intermediate vector bosons or gauge bosons), which are the quanta of the field and carry the properties associated with the field.

The electromagnetic, the weak and the strong interactions are mediated by the photon (γ), the three weak bosons ($W^{\pm}$, Z^0) and the eight gluons (g_α, $\alpha = 1, ..8$), respectively. The properties of the vector bosons are summarized in Table I.3. It is well known that the range of the interactions is inversely proportional to the mass of the intermediate boson. Hence, the electromagnetic interaction has an infinite range because the mass of the photon is zero. In contrast, the weak interaction has a short range ($\sim 10^{-16} m$) because of the heavy mass of the W and Z bosons. The mass of the gluons is zero, however, the range of the strong interaction is not infinite as it is expected but approximately 10^{-15} m due to an extra physical property, the quark confinement resulting from the self-interaction of the gluons. Since the gluons carry color charge (in fact they are bicolor particles) they interact not just with the quarks but also with each other. The weak bosons are also self-interacting while the photons are not.

Table I.3: The properties of the vector bosons.

Name	Spin [$\hbar$]	Charge [e]	Mass [MeV/c^2]
Photon (γ)	1	0	$< 2 \times 10^{-19}$
$W^{\pm}$	1	± 1	80.4×10^3
Z^0	1	0	91.2×10^3
Gluon (g_α, $\alpha = 1, ...8$)	1	0	0

gravitational field in the same fashion as the other fields has failed so far. However, it is expected that the gravitational interaction would be mediated by spin-2 bosons, called gravitons, since the gravitational field is described by a second-rank energy-momentum tensor in general relativity.

The nuclear force, which binds colorless protons and neutrons into nuclei, is the result of a residual strong interaction between the quark constituents of the nucleons. This is somewhat similar to the residual electrical interaction that gives rise to the force that binds electrically neutral atoms into molecules. The long range part of the nuclear forces can be described very accurately as the exchange of mesons (π, ρ and ω) between the nucleons.

As we have seen, three generations of fermions (leptons and quarks) are known to exist, however, there is no any known physical principle that would forbid adding more generations with the same properties but presumably heavier mass. Additional charged leptons or quarks could easily escape detection if they are very heavy[4]. However, if additional neutrinos would exist with mass less than $M_Z/2$, then the Z^0 boson would decay to them with the same rate as it decays to other neutrino species. Results from collider experiments measuring the invisible partial decay width of the Z^0 resonance [4] confirm that there are indeed only three light neutrinos and three corresponding fermion generations. In addition, the abundance of the light elements predicted by the Big Bang Nucleosynthesis theory is consistent with the observations only if three neutrino species are considered [5].

I.2 Symmetries of the Standard Model

All known phenomena related to the elementary particles and their interactions are extremely well described in the theoretical framework of the Standard Model (SM), which has successfully passed very precise tests (see for example [6, 7, 8]). The SM is a gauge field theory, which combines quantum field theory with the symmetry principles of the interactions. The relevant symmetry of the SM is

$$SU(3)_C \otimes SU(2)_L \otimes U(1)_Y,$$

[4]The t quark was discovered only in 1995

which includes the symmetry group of the strong interactions, $SU(3)_C$, and the symmetry group of the unified electroweak interactions, $SU(2)_L \otimes U(1)_Y$.

$SU(N)$ is the group of unitary transformations in the N-dimensional complex vector space, which leave the inner product unchanged and have determinant $+1$. These transformations can be represented by $N \times N$ complex matrices or $2N^2$ real numbers. The unitary requirement ($U^\dagger = U^{-1}$) imposes N^2 conditions, leaving N^2 independent number to represent the transformations. The extra condition on the determinant of the matrix implies that these transformations can be fully represented by $N^2 - 1$ real numbers. Any transformation of the $SU(N)$ group can be written in terms of $N^2 - 1$ generators (T_k) and the same number of continuous parameters (Θ_k):

$$U = \exp(-i\vec{\Theta}\vec{T}) = \exp\left(-i \sum_{k=1}^{N^2-1} \Theta_k T_k\right). \tag{I.1}$$

The generators of the group span a vector-space, called algebra, with the commutation relations as an additional operation:

$$[T_i, T_j] = i f_{ijk} T_k, \tag{I.2}$$

where the elements of the f_{ijk} antisymmetric tensor are the structure constants of the algebra. The generators can be represented by traceless Hermitian matrices, which are the three 2×2 Pauli matrices ($T_k = \frac{\sigma_k}{2}$, $k = 1, 2, 3$) in case of $SU(2)$ and the eight 3×3 Gell-Mann matrices ($T_k = \frac{\lambda_k}{2}$, $k = 1, ...8$) in case of the $SU(3)$ group [10]. We say that a physical system has a symmetry group if the Hamiltonian (or Lagrangian) of the system is invariant under the transformations represented by the group.

In $SU(3)_C$, the subscript C refers to colors, which act as the source of the strong interaction, just like the electric charge is the source of the electric field. The 3 refers to the three

color states, which are in the fundamental representation of the group having dimension three.

$SU(2)_L \otimes U(1)_Y$ [11] is the combination of the weak isospin group, $SU(2)_L$, where the L refers to the left-handed character of the weak interactions, and the weak hypercharge group $U(1)_Y$. The source of the charged weak interaction is the third component of the weak isospin, T_3, and operates only on left-handed particles[5] with negative helicity (ie. with the spin aligned opposite to the momentum). The left-handed particles are arranged in doublets with weak isospin $T = 1/2$ and $T_3 = \pm 1/2$ in each generation, so that the neutrinos (up-type quarks) are the weak isospin partners of the corresponding electrons (d-type quarks), e.g.

$$\begin{pmatrix} \nu_e \\ e_\nu \end{pmatrix}_L \qquad \begin{pmatrix} u \\ d \end{pmatrix}_L .$$

The right handed particles form isospin singlets with $T = T_3 = 0$. Right-handed neutrinos (and left-handed anti-neutrinos) do not exist in the minimal SM, therefore there are three right-handed particles in each generation, e.g.

$$e_R \qquad u_R \qquad d_R.$$

The source of the $U(1)_Y$ group is the so called weak hypercharge (Y), which is related to the electric charge (Q) and the weak isospin via the Gell-Mann-Nishijima relation:

$$Q = T_3 + \frac{Y}{2}. \tag{I.3}$$

The quantum number Y is equal to $B - L$ ($2Q$) for left (right) handed particles and it is conserved since T_3 and Q are conserved. The weak and electromagnetic interactions are

[5]The left-handed and right-handed fields are defined by the help of the chirality operator $\gamma^5 = -i\gamma^0\gamma^1\gamma^2\gamma^3$, e.g.

$$e_L = \frac{1}{2}(1 - \gamma_5)e \qquad e_R = \frac{1}{2}(1 + \gamma_5)e.$$

unified in that sense that the symmetry group $U(1)_Q$ generated by the electric charge and associated with the electromagnetic interactions is a subgroup of the total electroweak group:

$$U(1)_Q \subset SU(2)_L \otimes U(1)_Y.$$

Altogether 15 different fermion states exist in each generation: 2 (1) left (right) handed leptons and 2×3 (2×3) left (right) handed quarks[6]. These 15 states fall into five separate multiplets under the $SU(3)_C \otimes SU(2)_L \otimes U(1)_Y$ symmetry. For the first generation these multiplets are

$$\begin{pmatrix} u_L^g & u_L^b & u_L^r \\ d_L^g & d_L^b & d_L^r \end{pmatrix}_{1/3} \quad \left(u_R^g u_R^b u_R^r\right)_{4/3} \quad \left(d_R^g d_R^b d_R^r\right)_{-2/3} \quad \begin{pmatrix} \nu_L \\ e_L \end{pmatrix}_{-1} \quad e_{R-2},$$

where the superscripts g, b and r refer to the different color states of the quarks. The color $SU(3)$ group acts horizontally, while the weak $SU(2)$ vertically and the weak hypercharges are as indicated.

I.3 Principle of local gauge invariance

Continuous symmetries can be classified as global or local gauge symmetries depending on whether the continuous parameters of the transformation are or are not functions of the space time coordinates. Continuous symmetries play a crucial role in nature. For example, if a physical system is invariant under a global symmetry transformation then, according to Noether's theorem, there exist a current and an associated charge that are conserved. In addition, by promoting the global symmetry to local, the originally free theory transforms into an interacting theory containing new vector boson fields, the so called gauge fields [9].

[6]The factor of 3 comes from the three different colors.

The number of these gauge boson fields is equal to the number of the generators of the symmetry group: one in case of $SU(1)$, three for $SU(2)$ and eight for $SU(3)$.

In order to outline how the gauge principle works, we start with the Lagrangian density of a free fermion with mass m described by the Dirac field ψ (the Dirac conjugate field is defined as $\bar{\psi} = \psi^\dagger \gamma^0$):

$$\mathcal{L}_{\text{free}} = \bar{\psi} \left(i\gamma^\mu \partial_\mu - m \right) \psi. \tag{I.4}$$

It is obvious that the above Lagrangian is invariant under global unitary transformations, U, defined by Eq. I.1, which transform the field as

$$\psi(x) \to \psi' = U\psi(x) \tag{I.5}$$

since U is independent of x:

$$\bar{\psi}' \left(i\gamma^\mu \partial_\mu - m \right) \psi' = \bar{\psi} U^\dagger \left(i\gamma^\mu \partial_\mu - m \right) U\psi = \bar{\psi} U^\dagger U \left(i\gamma^\mu \partial_\mu - m \right) \psi = \bar{\psi} \left(i\gamma^\mu \partial_\mu - m \right) \psi. \tag{I.6}$$

Now, we can require invariance under local instead of global gauge transformations when the transformations are allowed to depend on the space-time coordinate x: $U(x)$. In this case the kinetic term is no longer invariant under the $\psi(x) \to \psi'(x) = U(x)\psi(x)$ transformation:

$$\bar{\psi}' \left(i\gamma^\mu \partial_\mu \right) \psi' = \bar{\psi} U^\dagger \left(i\gamma^\mu \partial_\mu \right) U\psi = \bar{\psi} \left[i\gamma^\mu \partial_\mu + i\gamma^\mu (U^\dagger \partial_\mu U) \right] \psi. \tag{I.7}$$

The most economic way to make the Lagrangian invariant under local gauge transformations is replacing the derivative ∂_μ with the covariant derivative D_μ, which is required to transform as the ψ field itself (Eq. I.5):

$$D_\mu \psi \to D_\mu \psi' = U D_\mu \psi. \tag{I.8}$$

To achieve this we have to introduce gauge fields, which transform properly under the local gauge transformations and interact with the fermion fields.

This principle has played a crucial role in building a consistent theory of the SM. The gauge theory based on the local transformations of the $U(1)_Q$ group is called Quantum Electrodynamics (QED), which is the most successful theory in particle physics. The gauge theory based on local color transformations of $SU(3)_C$ is Quantum Chromodynamics (QCD) [12], while the gauge theory based on the local transformations of the group $SU(2)_L \otimes U(1)_Y$ is called Electroweak Theory [13, 14]. The SM is the gauge theory based on the total local symmetry of the combined group $SU(3)_C \otimes SU(2)_L \otimes U(1)_Y$.

The covariant derivative, which transforms properly under local gauge transformations of the total $SU(3)_C \otimes SU(2)_L \otimes U(1)_Y$ group of the SM, can be written as

$$D_\mu = \partial_\mu + \frac{ig'}{2} B_\mu Y + \frac{ig}{2} \sum_{k=1}^{3} W_\mu^k \sigma_k + \frac{ig_s}{2} \sum_{k=1}^{8} G_\mu^k \lambda_k, \tag{I.9}$$

where

- B_μ is the vector field associated with the weak-hypercharge boson of $U(1)_Y$,
- $W_\mu^k (k = 1, 2, 3)$ are the vector fields associated with the three weak bosons of $SU(2)_L$,
- $G_\mu^k (k = 1, ..8)$ are the vector fields associated with the eight gluon fields of $SU(3)_C$.

The new kinetic term, $i\bar{\psi}\gamma^\mu D_\mu \psi$, in the Lagrangian contains the interactions between the fermion fields and the new vector bosons. For instance, the strong interaction between the quarks and gluons is described by the Lagrangian

$$\mathcal{L}_{\text{int}}^s = -g^s G_\mu^k \mathcal{J}_k^\mu = -g^s G_\mu^k \bar{\psi}\gamma^\mu \frac{\lambda_k}{2} \psi \ , \tag{I.10}$$

where $\mathcal{J}_k^\mu$ is the conserved current implied by the global $SU(3)_C$ symmetry. The strength of the interactions is proportional to the parameter g_s, called the coupling constant.

In order to include the propagation of the boson fields in the Lagrangian we have to add a local gauge invariant kinetic term for each boson field:

$$\mathcal{L}_{\text{boson}} = -\frac{1}{4} F_{\mu\nu} F^{\mu\nu}. \tag{I.11}$$

The second rank field strength tensors, $F_{\mu\nu}$'s, are given as

$$\partial_\mu B_\nu - \partial_\nu B_\mu \tag{I.12}$$

$$\partial_\mu W^k_\nu - \partial_\nu W^k_\mu + g\epsilon^{klm} W^l_\mu W^m_\nu \tag{I.13}$$

$$\partial_\mu G^k_\nu - \partial_\nu G^k_\mu + g f^{klm} G^l_\mu G^m_\nu \tag{I.14}$$

for the three different boson types, where ϵ^{klm}'s and f^{klm}'s are the structure constants of the $SU(2)$ and $SU(3)$ algebra, respectively. As we can see there is an important difference between the first field strength tensor and the last two. The latter ones contain an extra term which leads to three- and four-boson terms in the boson kinetic term given by Eq. I.11. These represent the self interaction of the weak and strong interaction bosons characteristic for any non-Abelian gauge theory, such as those represented by the $SU(2)_L$ and $SU(3)_C$ groups.

The self interaction of the gluons result in the antiscreening of the color charge at large distances by the vacuum, which causes the strong interaction to get weaker and weaker at short distances (large energies), in contrast to the strength of the electromagnetic interaction that gets stronger at short distances due to the screening of the electric charge at large distances [7]. This property is called asymptotic freedom and explains why the quarks inside

[7] The screening around an electric charge is the result of the vacuum polarization effect caused by virtual electron-positron pairs created and annihilated continuously by the field. Because of this effect, one experiences an effective charge smaller than the bare charge at large distances. If the electric charge is probed at shorter distances (higher energies), one penetrates the shielding deeper and observes more of the bare charge. The color charge is surrounded by virtual $q\bar{q}$ pairs, which has a similar screening effect as the e^+e^-

a hadron appear quasi free despite the fact they are tightly bound, and why it is so difficult to separate a quark from a hadron (quark confinement[8]).

The gauge fields W_μ^k and B_μ do not represent the physical gauge bosons of the electroweak theory: $W_\mu^\pm$, Z_μ^0 and A_μ. The latter ones can be obtained from the former ones by the following relations

$$\begin{aligned} W_\mu^\pm &= \tfrac{1}{\sqrt{2}}(W_\mu^1 \mp i W_\mu^2) \\ Z_\mu^0 &= \cos\Theta_W W_\mu^3 - \sin\Theta_W B_\mu \\ A_\mu &= \sin\Theta_W W_\mu^3 + \cos\Theta_W B_\mu, \end{aligned} \tag{I.15}$$

where Θ_W, is the weak angle, which defines the rotation in the neutral sector ($\sin^2\Theta_W = 0.2255 \pm 0.0021$). Then the interactions of the electroweak bosons with the fermions can be expressed as

$$\mathcal{L}_{\rm int}^{\rm EW} = -\frac{g}{\sqrt{2}}(W_\mu^+ \mathcal{J}_+^\mu + W_\mu^- \mathcal{J}_-^\mu) - \frac{g}{\cos\Theta_W} Z_\mu^0 J_{NC}^\mu - e A_\mu \mathcal{J}_{\rm em}^\mu, \tag{I.16}$$

where the weak coupling constant $g = e/\sin\Theta_W$. The charged weak currents are given by

$$\mathcal{J}_+^\mu = \sum_f \bar{\psi}_{fL} \gamma^\mu \sigma_+ \psi_{fL} \qquad \mathcal{J}_-^\mu = \sum_f \bar{\psi}_{fL} \gamma^\mu \sigma_- \psi_{fL}, \tag{I.17}$$

where the summation runs over the left-handed lepton and quark weak isospin doublets, and $\sigma_\pm$ are the isospin raising and lowering operators:

$$\sigma_+ = \frac{1}{2}(\sigma_1 + i\sigma_2) = \begin{pmatrix} 0 & 1 \\ 0 & 0 \end{pmatrix} \quad , \qquad \sigma_- = \frac{1}{2}(\sigma_1 - i\sigma_2) = \begin{pmatrix} 0 & 0 \\ 1 & 0 \end{pmatrix}. \tag{I.18}$$

pairs has on the the electric charge. However, gluon-gluon pairs are also produced around the color charge because of the gluon self-interaction and they have an opposite effect: it causes the interaction to grow at large distances. This antishielding has a larger contribution than the shielding due to the $q\bar{q}$ pairs and makes the coupling decrease at small distances.

[8]The larger the distance among the quarks the more energy needed to separate them further. The increased energy of the color field between the separated quarks transforms into mass producing new quark-antiquark pairs, which then recombine with the old quarks to form hadrons instead of free quarks.

The neutral weak current and electromagnetic current are written as

$$\mathcal{J}^{\mu}_{\rm NC} = \sum_{f} g^{f}_{L} \bar{\psi}_{fL} \gamma^{\mu} \psi_{fL} + \sum_{f \neq \nu} g^{f}_{R} \bar{\psi}_{fR} \gamma^{\mu} \psi_{fR} \tag{I.19}$$

$$\mathcal{J}^{\mu}_{\rm em} = \sum_{f} Q_{f} \bar{\psi}_{fL} \gamma^{\mu} \psi_{fL} + \sum_{f \neq \nu} Q_{f} \bar{\psi}_{fR} \gamma^{\mu} \psi_{fR}, \tag{I.20}$$

where the sum runs over left-handed doublets and right-handed singlets and the couplings depend on the third component of the weak-isospin and the charge of the fermion as well as the weak angle:

$$g_{L} = T_{3} - Q \sin\Theta_{W} \quad , \quad g_{R} = -Q \sin\Theta_{W}. \tag{I.21}$$

As we mentioned earlier, the three weak bosons, $W^{\pm}$ and Z^{0}, are different from the other gauge bosons in that they are massive particles. However, the requirement of local gauge invariance does not allow addition of mass terms, such as $M^{2}_{W} W_{\mu} W^{\mu}$, to the Lagrangian. These two facts together indicates that the $SU(2)_{L} \otimes U(1)_{Y}$ group is not a symmetry of the vacuum. In contrast, the photon and gluons being massless reflects that $U(1)_{Q}$ and $SU(3)_{C}$ are good symmetries of the vacuum. The spontaneous symmetry breaking of the SM Lagrangian

$$SU(3)_{C} \otimes SU(2)_{L} \otimes U(1)_{Y} \rightarrow SU(3)_{C} \otimes U(1)_{Q}$$

by means of the Higgs Mechanism provides the proper masses to the weak bosons and the fermions. We outline this in the next section.

I.4 Spontaneous symmetry breaking: Goldstone bosons and the Higgs mechanism

A physical system has a spontaneously broken symmetry if the interactions governing the dynamics of the system possesses the symmetry, that is the Lagrangian describing the system is invariant under the symmetry transformations, but the dynamics of the system leads to a

degenerate set of ground states (lowest energy states; also called *vacuum* states), which are not invariant under that symmetry. Of course, only one of these equivalent vacuum states is manifested, and therefore, it conceals the symmetry of the theory.

This phenomenon can be illustrated by the infinitely extended ferromagnet near the Curie temperature, T_C. The interactions between the spins or magnetic dipole moments are invariant under spatial rotation. Above the Curie temperature, the orientation of the spins are disordered in the absence of an external magnetic field and the medium displays an exact rotational symmetry: the average magnetization is zero and there is no preferred direction in space. In contrast, for temperatures below T_C, the system has a non-zero spontaneous magnetization since the interactions between the neighboring magnetic moments favors the parallel alignment of spins. Since the direction of the spins are arbitrary, there are infinite possible ground states, each corresponding to one possible spatial direction and having the same energy. However, none of these states are rotationally invariant since there is a privileged direction. The spontaneous symmetry breaking manifests itself when the system chooses one among these infinite possible non-invariant ground states.

Other examples can be found in systems that goes through second order phase-transitions such as superconductors, where Cooper pairs of electrons are formed below the critical temperature and the density of the Cooper pairs plays the same role as the direction of spontaneous magnetization of the ferromagnet in the above example. Ginzburg and Landau provided a phenomenological theory of superconductivity [15] and this was the precursor of the theory adopted later in the SM.

An important consequence of spontaneous symmetry breaking is the appearance of massless particles as it is described by the Goldstone Theorem [16]:

> If the Lagrangian of a theory is invariant under a continuous symmetry that is

not a symmetry of the physical vacuum, $\mid 0 >$, then there must exist one massless spin-zero (scalar or pseudoscalar) boson associated to each broken generator T of the original symmetry group, which does not leave the vacuum invariant[9] (i.e. $T \mid 0 > \neq 0$). These modes, called *Nambu-Goldstone bosons* or simply *Goldstone bosons*, are the zero-energy excitations that connect possible distinct vacuum states (the state $T \mid \ 0 >$ is an eigenstate of the Hamiltonian with the same eigenvalue (E_0) as the vacuum since $HT \mid 0 >= TH \mid 0 >= E_0 T \mid 0 >$).

Since this theorem plays an important role in this thesis, we provide a formal proof in Appendix A.

We should note that, the Nambu-Goldstone boson arising from the spontaneous break-down of a continuous symmetry is massless only if the symmetry is exact. If there is a small explicit symmetry breaking, either already in the Lagrangian or due to quantum mechanical effects such as anomalies, then the Goldstone boson acquires a small mass and it is called pseudo Nambu-Goldstone boson.

An example for Nambu-Goldstone bosons in particle physics is the spontaneous chiral symmetry breaking of the strong interaction Lagrangian, which implies the existence of three Goldstone bosons identified with the three pions. The fact that the pions have a non-zero mass is the consequence of the soft extra explicit break down of the chiral symmetry due to the non-zero mass of the quarks.

The Goldstone Theorem holds for spontaneously broken global symmetries only. If the spontaneously broken symmetry is a local gauge symmetry the Higgs Mechanism operates

[9]This means that

$$\exp(i\Theta T) \mid 0 > \approx (I + i\Theta T) \mid 0 > \neq \mid 0 > .$$

[17]: The would-be Goldstone bosons associated to the global symmetry breaking do not manifest explicitly in the physical spectrum but instead they combine with the normally massless gauge bosons and provide the gauge bosons with mass. The number of gauge bosons that acquire mass is equal to the number of these would-be Goldstone bosons.

In order to implement the Higgs Mechanism in the Standard Model we have to introduce a complex $SU(2)$ doublet field[10], the so called Higgs field (with hypercharge $Y = 1$):

$$\Phi = \begin{pmatrix} \phi^+ \\ \phi^0 \end{pmatrix}; \qquad \phi^{+(0)} = \frac{1}{\sqrt{2}} \left(\phi_1^{+(0)} + i\phi_2^{+(0)} \right). \tag{I.22}$$

The interaction of this field with the the gauge particles is described by the kinetic term of the Lagrangian

$$\mathcal{L}_H = (D_\mu \Phi)^\dagger (D^\mu \Phi) - V(\Phi). \tag{I.23}$$

The effective self-interaction potential of the Higgs field is given by

$$V(\Phi) = \mu^2 \Phi^\dagger \Phi + \lambda (\Phi^\dagger \Phi)^2, \tag{I.24}$$

where μ and $\lambda > 0$ are parameters. The presence of the covariant derivative

$$D_\mu = \partial_\mu + \frac{ig'}{2} B_\mu Y + \frac{ig}{2} \vec{W}_\mu \vec{\sigma} \tag{I.25}$$

instead of the normal derivative in the kinetic term ensures local gauge invariance of the Lagrangian under $SU(2)_L \otimes U(1)_Y$ rotations.

The lowest energy state (vacuum) must be constant everywhere so that the kinetic term is zero and it can be obtained from the condition

$$\delta V(\Phi) = \Phi^\dagger \left[\mu^2 + 2\lambda (\Phi^\dagger \Phi) \right] \delta\Phi = 0 \tag{I.26}$$

[10]The minimal supersymmetric extension of the Standard Model assumes two complex doublets.

for any variation $\delta\Phi$. Depending on the sign of the parameter μ^2 there are two possible distinct cases:

If $\mu^2 > 0$, the effective potential has a unique minimum at $\Phi = 0$. The vacuum (lowest energy state) preserves the $SU(2)_L \otimes U(1)_Y$ symmetry of the Lagrangian. The particle spectrum consists of four massive scalar mesons ($\phi_1^{+(0)}$, $\phi_2^{+(0)}$), each with mass μ, and four massless gauge bosons (W_μ^k, B_μ).

If $\mu^2 < 0$, the potential has a local maximum at $\Phi = 0$ and the absolute minimum of the potential now occurs when[11]

$$\mid \Phi \mid^2 = \mid \phi^+ \mid^2 + \mid \phi^0 \mid^2 = \frac{-\mu^2}{2\lambda} \equiv \frac{v^2}{2}. \tag{I.27}$$

However, the vacuum must be neutral ($\phi^+ = 0$), and therefore, has the form

$$\Phi_0 = \begin{pmatrix} 0 \\ \\ \phi^0 \end{pmatrix}, \qquad \mid \phi^0 \mid = \frac{v}{\sqrt{2}}. \tag{I.28}$$

which corresponds to a continuum of distinct states being degenerate in energy. In addition, the vacuum of the system must be uniquely represented by a particular phase. Either of these vacuum states violates the original $SU(2)_L \otimes U(1)_Y$ symmetry since $\sigma_k \Phi_0 \neq 0$ and $Y\Phi_0 = +1\Phi_0 \neq 0$. At the same time they possess $U(1)_Q$ symmetry because

$$Q\Phi_0 = \left(T_3 + \frac{Y}{2}\right)\Phi_0 = \frac{1}{2}(\sigma_3 + Y)\Phi_0 = \begin{pmatrix} 1 & 0 \\ \\ 0 & 0 \end{pmatrix}\begin{pmatrix} 0 \\ \\ \phi^0 \end{pmatrix} = \begin{pmatrix} 0 \\ \\ 0 \end{pmatrix} \tag{I.29}$$

With a suitable definition of the coordinates, we can chose a vacuum state, such that $\phi^0 = v$ and the small fluctuations around this vacuum state can be parameterized as

$$\Phi = \exp(i\vec{\zeta}(x)\vec{\sigma}) \begin{pmatrix} 0 \\ \\ v + h(x) \end{pmatrix}. \tag{I.30}$$

[11]The quantity v is called the vacuum expectation value of the scalar field Φ. It can be expressed as $v = (\sqrt{2}G_F)^{-1/2} \approx 246$ GeV, where G_F is the Fermi constant, the low energy coupling strength of the weak interaction.

The three real fields ζ are excitations of the field along the potential minimum; they connect the distinct vacuum states. These fields correspond to the massless Goldstone bosons of the global $SU(2)$ symmetry. However, in local gauge theory these unphysical fields can be eliminated by the local gauge transformation:

$$\Phi \rightarrow \Phi' = \exp(-i\vec{\zeta}(x)\vec{\sigma})\Phi, \tag{I.31}$$

which implies the appropriate transformations of the gauge fields. Therefore, the three would-be Goldstone bosons entirely disappear from the Lagrangian and they reappear only as the longitudinal component of the three massive weak-bosons associated with $SU(2)$. The forth gauge boson, the photon, remains massless reflecting the invariance of the vacuum under $U(1)_Q$. Finally, the $h(x)$ field becomes massive with mass $M_H = \sqrt{2} \mid \mu \mid$ through self-interaction and shows up in the spectrum as an extra scalar particle called the Higgs boson.

The discovery of the massive $W^{\pm}$ and Z^0 gauge bosons at CERN in $p\bar{p}$ collisions in 1983 [18] was the first experimental evidence for the spontaneous symmetry breaking of the electroweak interactions. However, the symmetry breaking sector of the Standard Model is not experimentally confirmed yet since the search for the Higgs boson has failed so far because of its large mass. However, the ALEPH collaboration reported [19] the observation of a 3σ excess beyond the expected background in the data collected during the extended run of the LEP (Large Electron-Positron Collider) at CERN in year 2000. This excess is mainly due to three events which are consistent with the production of the Standard Model Higgs boson with a mass around 114 GeV/c^2. The task to find conclusive evidence for the existence of the Higgs boson remains for the current experimental run of the upgraded Tevatron $p\bar{p}$ collider at Fermilab and/or the future LHC (Large Hadron Collider), which is

under construction at CERN and will start to operate around 2006.

The fermions can also interact with the scalar Higgs field (Yukawa coupling), which provides them with mass. In case of the quarks the Lagrangian of the interaction is given by

$$\mathcal{L}^q_{\rm YW} = -g^u_{\rm YW}\left[\bar{q}_L\bar{\Phi}u_R + \bar{u}_R\bar{\Phi}^\dagger q_L\right] - g^d_{\rm YW}\left[\bar{q}_L\Phi d_R + \bar{d}_R\Phi^\dagger q_L\right], \tag{I.32}$$

where $\bar{\Phi} = i\sigma_2\Phi^*$, while for leptons it is

$$\mathcal{L}^\ell_{\rm YW} = -g^\ell_{\rm YW}\left[\bar{\ell}_L\Phi e_R + \bar{e}_R\Phi^\dagger\ell_L\right] \tag{I.33}$$

Note that, no mass term appears for the neutrinos in the Standard Model. The coupling strengths g^f_{YW} are fundamental parameters of the Standard Model[12] and their values are chosen to give the proper mass for the fermions.

I.5 Quark mixing

The previously outlined theory of electroweak interactions displays a symmetry between the leptons and quarks: the three generations of leptons and the three generations of quarks have identical charged current weak interactions. The Lagrangian describing the charged current weak interactions (Eq. I.16) for leptons takes the form

$$\mathcal{L}^\ell_{\rm EW} = -\frac{g}{\sqrt{2}}[(\bar{\nu}_{eL}\gamma^\mu e_L + \bar{\nu}_{\mu L}\gamma^\mu\mu_L + \bar{\nu}_{\tau L}\gamma^\mu\tau_L)W^+_\mu + h.c.], \tag{I.34}$$

where $h.c.$ is the hermition conjugate of the first three terms. We can see that the charged current weak interactions operate on the disconnected weak-isospin lepton doublets, as required by the separate conservation of the family lepton numbers.

[12]The Standard Model contains 18 parameters, that are necessary to fit all the observed data at low energy. Half of these parameters are related to the masses of the 6 quarks and the 3 charged leptons. Other parameters are the mass of the Z^0 weak boson (M_W is not independent from M_Z and $\sin^2\Theta_W$), the Higgs boson's mass, the electromagnetic coupling constant (α), the strong coupling constant ($\alpha_s(M_Z)$), the weak angle ($\sin^2\Theta_W$) and four parameters related to the quark mixing matrix (see next section).

If one now replaces the lepton fields in the above Lagrangian with the corresponding quark fields from the same generation (i.e. $\nu_e \rightarrow u$, $e \rightarrow d$ etc.) then the Lagrangian of charged current weak interactions for quarks arose. However, there is a significant difference between the two fermion species: the quarks bear color charge in contrast to the leptons and consequently interact strongly besides the electroweak coupling. As a result, the quark weak eigenstates do not coincide with the mass eigenstates defined by the total Hamiltonian including the strong interactions. However, the weak eigenstates can be expressed as linear combinations of the mass eigenstates. The mixing was first parameterized for three generations by Kobayashi and Maskawa [20] in terms of a 3×3 complex unitary matrix V operating on the charge $Q = -1/3$ quark mass eigenstates (d, s, b):

$$\begin{pmatrix} d' \\ s' \\ b' \end{pmatrix} = \begin{pmatrix} V_{ud} & V_{us} & V_{ub} \\ V_{cd} & V_{cs} & V_{cb} \\ V_{td} & V_{ts} & V_{tb} \end{pmatrix} \begin{pmatrix} d \\ s \\ b \end{pmatrix}. \tag{I.35}$$

This relationship is the generalization of the four-quark mixing, which was parameterized by a single real number, the Cabibbo angle (Θ_C) [21]

$$\begin{pmatrix} d' \\ s' \end{pmatrix} = \begin{pmatrix} \cos\Theta_C & \sin\Theta_C \\ -\sin\Theta_C & \cos\Theta_C \end{pmatrix} \begin{pmatrix} d \\ s \end{pmatrix}. \tag{I.36}$$

This means that, the weak interaction really operates on the following weak-isospin quark doublets:

$$\begin{pmatrix} u \\ d' \end{pmatrix} \qquad \begin{pmatrix} c \\ s' \end{pmatrix} \qquad \begin{pmatrix} t \\ b' \end{pmatrix},$$

and then the Lagrangian of the charged current weak interaction in the quarks sector is

$$\mathcal{L}^q_{\rm EW} = -\frac{g}{\sqrt{2}}[(\bar{u}_L\gamma^\mu d'_L + \bar{c}_L\gamma^\mu s'_L + \bar{t}_L\gamma^\mu b'_L)W^+_\mu + h.c.]. \tag{I.37}$$

If we use Eq. I.35 to express the weak eigenstates then the first term in Eq. I.37 reads as

$$-\frac{g}{\sqrt{2}}\bar{u}_L\gamma^\mu d'_L W^+_\mu = -\frac{g}{\sqrt{2}}(V_{ud}\bar{u}_L\gamma^\mu d_L + V_{us}\bar{u}_L\gamma^\mu s_L + V_{ub}\bar{u}_L\gamma^\mu b_L)W^+_\mu. \qquad \text{(I.38)}$$

That is the u quark couples to the s and b quarks, too, and not exclusively to the d quark. The same holds for the c and t quarks. As we can see from this example, the relative strength of the charged current weak coupling between the up-type quarks and the down-type quarks is proportional to the corresponding matrix element of V. In contrast to the charge current interactions, the neutral current weak interactions among the quarks are diagonal similarly to the case of the lepton sector since the mixed-quark terms cancel each other (GIM mechanism [14]). This feature of the model implies the absence of flavor-changing neutral weak-currents (e.g. $s \to d$), which is experimentally confirmed at the current precision.

In contrast to the case of two particle generations where one real parameter is sufficient to parameterize the elements of the Cabibbo matrix (see Eq. I.36), we need nine parameters, three real angles and six imaginary phases, to fully describe the Cabibbo-Kobayashi-Maskawa quark-mixing matrix. Five out of the six phases are removable leaving only one imaginary phase. Within the framework of the Standard Model, CP violation[13] can occur only if this remaining phase is non-zero. The four remaining parameters are fundamental constants of the Standard Model and their accurate measurement is very important. A great deal of effort has been invested into the precise measurement of the individual matrix elements, which can be determined from weak decays of the relevant quarks or, in some cases, from deep inelastic neutrino scattering.

[13]According to the CPT theorem, the combined application of charge conjugation (C), parity reversal (P) and time reversal (T) is an exact symmetry of any local field theory, such as the Standard Model. The strong and electromagnetic interactions preserve all three symmetries separately, while the weak interaction violates both C and P. In 1964, a small CP symmetry violation was discovered in K^0 decays. This year, the Belle (at KEK-B, Japan) and the BaBar (at PEP-II, SLAC) collaborations announced the long anticipated observation of non-zero CP violation in the $B^0 - \bar{B}^0$ system [22].

Several parametrizations of the CKM matrix exist in the literature. Among these, the most favored is that proposed by Wolfenstein [23]:

$$V \approx \begin{pmatrix} 1-\lambda^2/2 & \lambda & A\lambda^3(\rho - i\eta) \\ -\lambda & 1-\lambda^2/2 & A\lambda^2 \\ A\lambda^3(1-\rho-i\eta) & -A\lambda^2 & 1 \end{pmatrix}, \tag{I.39}$$

in which A, ρ and η are real number close to unity. $\lambda \equiv \sin\Theta_C \approx 0.22$ is an expansion parameter and terms of order $\lambda^4 \approx 10^{-3}$ or higher are dropped. This parametrization demonstrates that the CKM matrix is close to diagonal and consequently the off-diagonal charged weak couplings among the quarks are highly suppressed (Cabibbo suppression).

The unitarity constraint on V ($V^\dagger V = VV^\dagger = I$) imposes six normalization conditions on the rows and columns of the matrix (corresponding to the diagonal elements of I). The off-diagonal places in $V^\dagger V = VV^\dagger = I$ give six orthogonality conditions for two different rows or columns of the matrix, such as

$$V_{ud}V_{ub}^* + V_{cd}V_{cb}^* + V_{td}V_{tb}^* = 1 \tag{I.40}$$

between the first and third columns. Each of these equations require three complex quantities to vanish and therefore can be represented by a triangle, the so called unitarity triangle, in the complex plane. All six triangle have the same area, which is non-zero if CP violation occurs. Since V_{cb} and V_{cd} are real to a very good approximation, we can choose to orient the *db*-triangle corresponding to Eq. I.40 so that $V_{cd}V_{cb}^*$ lies along the real axis. This triangle shown in Fig. I.1 has attracted the most attention due to the relative accessibility of its sides and angles to experiments. The combination of these measurements can be used to test unitarity and the validity of the Standard Model.

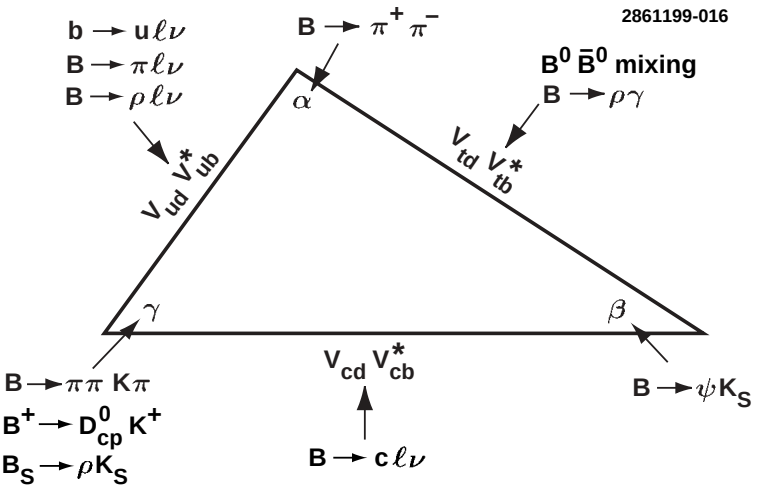

Figure I.1: The *db* unitarity triangle represented by Eq. I.40. The experiments that can be used to determine its sides and angles and check the consistency of the Standard Model are shown.

CHAPTER II

SPONTANEOUS FAMILY SYMMETRY BREAKING AND FAMILONS

II.1 Family (flavor) symmetry

After the muon was discovered and its properties and interactions were found to be identical to those of the electron except for corrections resulting from its heavier mass, Isidor Rabi asked the famous question: "Who ordered that?". Since that time a bunch of additional (elementary) particles have been discovered and were eventually arranged in three identical fermion families based on their interaction properties. In the limit of vanishing mass, the three fermion generations are indistinguishable with respect to the strong and electroweak interactions. Rabi's question is now replaced by an equally difficult one: Why do fermions repeat themselves three times, only to have a different mass spectrum?

The total Lagrangian of the Standard Model can be written as

$$\mathcal{L}_{\rm SM} = \mathcal{L}_{\rm free} + \mathcal{L}_{\rm int} + \mathcal{L}_{\rm YW}, \tag{II.1}$$

where $\mathcal{L}_{\rm free}$ is the Lagrangian of the free fermions (and gauge fields), $\mathcal{L}_{\rm int}$ is the Lagrangian describing interaction between the fermions and the gauge fields, and $\mathcal{L}_{\rm YW}$ is the Yukawa interaction between the fermions and the Higgs field, which provides the fermions with mass. In order to understand the problem of particle families better, we imagine that we can turn on the terms of the above Lagrangian separately one after the other. In the absence of gauge and Yukawa interactions, the Standard Model Lagrangian has a $U(45)$ global symmetry, which represents the freedom of being able to interchange any of the 15 fermion states of the three families with one another. If we now add the gauge interactions to the free Lagrangian, then

the 15 states in each family are divided into five multiplets (see section I.2) and the $U(45)$ symmetry of the Lagrangian is broken to $U(3)^5$ corresponding to interchanging fermions of a given multiplet from one family to another. When the Yukawa couplings are also turned on, the fermions are endowed with mass and the family (flavor) symmetry is lost: the flavor group $U(3)^5$ is explicitly broken to $U(1)_B \otimes U(1)_L$.

The main objective of particle physics for over half a century has been to understand the origin of the fermion mass hierarchy and weak mixing pattern, which in the Standard Model is simply parameterized in terms of many fundamental, however arbitrary, coupling constants, that are merely fit to the data. This problem is not solved by the "vertical" extensions of the Standard Model either: these theories can successfully unify the apparently separate gauge interactions and bring some order to the scattered multiplets of quarks and leptons within each family[1] but they can not bring us closer to the ultimate understanding of the family structure of particles.

It seems appealing to extend the model by assuming that there exist a subgroup of the flavor group, which is an exact symmetry of the total Lagrangian but it is not manifest in the vacuum since the observed particle masses are different from one family to the other. This spontaneously broken "horizontal" symmetry can be discrete, continuous and local,

[1]These unification theories are very attractive from this point of view: in the $SU(5)$ [24] extension the 15 particle states are organized into only two representations of the symmetry group. A more promising extension of $SU(5)$ to the larger $SO(10)$ group [25] makes possible to unite all fermions of a family into a single multiplet. In fact, this single representation can accommodate 16 fermion states, that is one more than the 15 degrees of freedom of the Standard Model family. The quantum numbers of this extra family member is identical to those of a massive right-handed neutrino, which was proposed to solve the problem of the non-vanishing neutrino mass in the Standard Model. As we saw before, the Standard Model in its conventional form does not allow non-zero neutrino mass (see section I.4) in growing contradiction to the recent observation of the neutrino oscillation mentioned in section I.1. However, a singlet right-handed very massive fermion, which is consistent with all symmetries and requirements of the Standard Model, can generate small mass for the observed neutrinos via the so called "see-saw" mechanism [26].

continuous and global, or it might be a combination of these. Among these, the most attractive is the possibility of a spontaneously broken continuous global family symmetry, which implies the existence of massless Nambu-Goldstone bosons (see section I.4), called *familons* [27]. However, spontaneously broken global symmetries were considered unacceptable in any realistic model for a long time since the massless Goldstone bosons could potentially mediate neutral current processes and would give rise to non-relativistic long-range r^{-1} potential. Later, it turned out that Goldstone bosons associated with a global symmetry broken at a very large energy scale will couple weakly to matter and need not to be feared [28]. Thus continuous global symmetries can be considered as a candidate for the spontaneously broken family (flavor) symmetry [27, 29] and we explore this possibility in this thesis.

The idea of spontaneously broken continuous global symmetries and the existence of the associated Goldstone bosons is not unprecedented in particle physics. A spontaneous violation of global $U(1)$ lepton-number symmetry was proposed in extensions of the Standard Model in order to generate mass for the neutrinos. This model leads to massive right-handed Majorana neutrinos and the mass for the left-handed neutrinos is generated by the coupling of this extra neutrino to leptons through the Higgs field ("see-saw" mechanism). The Nambu-Goldstone boson associated with this model is the majoron, which has several varieties depending on the different schemes for breaking the lepton-number symmetry [30].

A spontaneously broken continuous global symmetry would also provide solution for an other deficiency of the Standard Model: the so called strong CP problem [31]. In the strong interaction Lagrangian, there is a term[2]

$$\mathcal{L} = \Theta \frac{\alpha_s}{8\pi} G_{a\mu\nu} \tilde{G}_a^{\mu\nu} \tag{II.2}$$

[2]Here $G_{\mu\nu}$ stands for the gluon field strength tensor.

that violates P and T (and CP as well). Since this term contributes to the electric dipole moment of the neutron, the strong experimental bound on d_n requires that $\Theta < 10^{-9}$, even though any value is equally likely because it is a free parameter. To solve this problem, Peccei and Quinn proposed an additional global (pseudo) symmetry $U(1)_{\rm PQ}$ that can set the Θ parameter to zero [32]. Since this symmetry is spontaneously broken by the vacuum, there is an associated pseudo Nambu-Goldstone boson, the almost massless axion[3], in the theory [33].

Reiss [29] and Wilczek [27] suggested the possibility that the Peccei-Quinn (PQ) symmetry might be a small part of a larger flavor symmetry group and therefore the strong CP problem would be automatically solved in this case. Also, Chang and Senjanovic [34] found that, the PQ symmetry is a very natural consequence of a theory based on the combination of the "vertical" $SO(10)$ local gauge symmetry and a "horizontal" $SU(N)$ global family symmetry. Furthermore, this theory favors three families ($N = 3$) if the lepton-number breaking is tied to the family and PQ symmetry breaking.

Finally, we would like to mention a cosmological motivation as well. A massive unstable neutrino (typically the tau-neutrino) was advocated in several cosmological scenarios related to big-bang nucleosynthesis [35] and large scale structure formation [36] in order to obtain reasonable agreement between theory and observations. However, visible neutrino decays to photons or electrons are severely constrained by observation of supernova SN 1987A since these decays would have increased the visible luminosity of the supernova with respect to its

[3]The small mass of the axion is the consequence of the small explicit breaking of the symmetry due to quantum mechanical anomalies with the gluons. In the original theory, the spontaneous symmetry breaking was assumed at the electroweak scale $v \sim 246$ GeV, which resulted in too strong axion coupling and too large mass which was excluded experimentally. One possible way to save the idea is to bring up the Peccei-Quinn symmetry breaking scale so that the coupling of the axion to fermionic matter is suppressed to a level, that is not in violation with existing limits. These models are called invisible axion models and two types of them were discussed widely in the literature: the DFSZ or GUT axion and the KSVZ or hadronic axions.

neutrino luminosity. In addition, ν_τ decay to three neutrinos is also excluded since no flavor violating τ decays, which would be implied by $SU(2)_L$ gauge invariance, were observed. On the other hand, the tau-neutrino decaying to a lighter neutrino and a massless boson such as the familon would solve the problem.

II.2 Familon Interaction

Familons, the massless Nambu-Goldstone bosons associated with a spontaneously broken family symmetry, couple derivatively to the flavor current [28]. At low energies, the coupling can be described by the effective Lagrangian [27, 28, 37]

$$\mathcal{L}_f = \frac{1}{F}(\partial_\mu f^a)\mathcal{J}^{a\mu}, \tag{II.3}$$

where f^a are the familon fields, $\mathcal{J}^{a\mu}$ are the flavor currents and F is the energy scale at which the global flavor symmetry is spontaneously broken and the familon is generated. The index a distinguishes the independent familon fields associated with the broken generators T^a of the family symmetry group[4].

The most general flavor current composed of two fermion fields is an arbitrary mixture of vector and axial-vector currents

$$\mathcal{J}^{a\mu} = \bar{\psi'}_i\gamma^\mu(g_V + g_A\gamma^5)T^a_{ij}\psi'_j, \tag{II.4}$$

written in terms of the fermion flavor eigenstates, ψ'_i and ψ'_j, with i and j being the flavor indices [5]. The second quantized ψ_j represents the annihilation operator of fermion j, while $\bar{\psi}_i$ refers to the creation of fermion i. g_V and g_A are relative coupling constants of the vector and axial-vector currents, respectively, for which $g_V^2 + g_A^2 = 1$. The details of the

[4]Of course, the number of the independent familons is one if the broken family symmetry is $U(1)$.

[5]Since the familon is neutral it can couple to two quarks with the same charge only (either two u-type or two d-type quarks). Therefore, the flavor indices are generational indices as well.

interactions depend on the particular family symmetry group that is broken. For example, if the Lagrangian has $O(N)$ symmetry, then the generators T_{ij} are anti-symmetric tensors, which can not generate flavor-diagonal interactions. However, flavor-diagonal interactions can also occur in this particular case due to the quark mixing effects discussed in section I.5.

Let's assume that, the flavor eigenstates ψ' are related to the mass eigenstates ψ by $\psi' = V\psi$, where V is a 3×3 unitary matrix, such as the CKM matrix in case of the down-quark sector. Then the $\mathcal{J}^{a\mu}$ current is given in the mass-eigenstate basis by

$$\mathcal{J}^{a\mu} = \bar{\psi}_i \gamma^\mu (g_V + g_A \gamma^5) V^\dagger T^a_{ij} V \psi_j. \tag{II.5}$$

In the following, we will denote the transformed matrix $V^\dagger T^a_{ij} V$ as T^a_{ij}. If we substitute the above form of the flavor current to Eq. II.3, the familon interaction can be written as

$$\mathcal{L}_f = \frac{1}{F} (\partial_\mu f^a) \bar{\psi}_i \gamma^\mu (g_V + g_A \gamma^5) T^a_{ij} \psi_j. \tag{II.6}$$

By partial integration it takes the form

$$\begin{aligned} \mathcal{L}_f &= -\frac{1}{F} f^a \partial_\mu \left[\bar{\psi}_i \gamma^\mu (g_V + g_A \gamma^5) T^a_{ij} \psi_j \right] \\ &= -\frac{1}{F} f^a \left[\left(\partial_\mu \bar{\psi}_i \right) \gamma^\mu (g_V + g_A \gamma^5) T^a_{ij} \psi_j + \bar{\psi}_i \gamma^\mu (g_V + g_A \gamma^5) T^a_{ij} \left(\partial_\mu \psi_j \right) \right] \\ &= -\frac{1}{F} f^a \left[\left(\partial_\mu \bar{\psi}_i \right) \gamma^\mu (g_V + g_A \gamma^5) T^a_{ij} \psi_j + \bar{\psi}_i (g_V - g_A \gamma^5) T^a_{ij} \gamma^\mu \left(\partial_\mu \psi_j \right) \right], \end{aligned} \tag{II.7}$$

where in the last step we used the anticommutation relation $\{\gamma^\mu, \gamma^5\} = 0$, that is $\gamma^\mu \gamma^5 = -\gamma^5 \gamma^\mu$. Now we can substitute the Dirac equation of the fermion field and its conjugate:

$$i\gamma^\mu \partial_\mu \psi = m\psi \qquad -i\gamma^\mu \partial_\mu \bar{\psi} = m\bar{\psi}, \tag{II.8}$$

to get

$$\begin{aligned} \mathcal{L}_f &= -\frac{i}{F} f^a \left[m_i \bar{\psi}_i (g_V + g_A \gamma^5) T^a_{ij} \psi_j - m_j \bar{\psi}_i (g_V - g_A \gamma^5) T^a_{ij} \psi_j \right] \\ &= -\frac{i}{F} f^a \bar{\psi}_i \left[g_V (m_i - m_j) + g_A (m_i + m_j) \gamma^5 \right] T^a_{ij} \psi_j. \end{aligned} \tag{II.9}$$

However, this form of the Lagrangian is valid only for on-shell fermions, such as external leptons, while in hadronic matrix elements and processes including off-shell fermions, the most general form given by Eq. II.6 must be used.

Equation II.9 demonstrates an important property of the familon interactions, namely that, in the fermion mass eigenstate basis, the flavor conserving couplings ($\psi_i = \psi_j$) of the familon are always axial-vector type, while the flavor changing couplings may have both vector and axial-vector parts. Since the long-range potentials arise as a consequence of flavor conserving interactions between nucleons or electrons, the long-range potential mediated by familons must be axial-vector type. In the $r \to \infty$ limit (or $q \to 0$, where q is the momentum transferred to the familon) the potential resulting from the familon exchange is a spin-dependent tensor potential $V(r) \sim [\mathbf{s}_1 \cdot \mathbf{s}_2 - 3(\mathbf{s}_1 \cdot \hat{\mathbf{r}})(\mathbf{s}_2 \cdot \hat{\mathbf{r}})]r^{-3}$ [28]. A family symmetry breaking scale $F \geq 10 - 100$ GeV ensures the invisibility of the non-relativistic potential conveyed by the familon in "fifth-force" experiments [38].

As we can see, the strength of the familon interaction is inversely proportional to F, the family symmetry breaking scale: the larger F, the weaker the interaction. However, the coupling strength depends also on the relative couplings $g_{V(A)}$ and the matrix elements T_{ij}. Therefore, it is convenient to define a normalized family symmetry breaking scale by

$$F_{ij} = \frac{F}{\sqrt{(g_V T_{ij})^2 + (g_A T_{ij})^2}} \tag{II.10}$$

and similarly with only vector or axial-vector type interaction by

$$F_{ij}^V = \frac{F}{g_V T_{ij}} \qquad \text{and} \qquad F_{ij}^A = \frac{F}{g_A T_{ij}}. \tag{II.11}$$

We can determine these quantities experimentally in a model independent manner but we have to make an assumption about the structure of the broken family symmetry (the generators T) in order to extract the value of F itself.

II.3 Previous experimental and astrophysical constraints

The coupling strength of familons to matter and therefore the family symmetry breaking scale can be constrained from astrophysical considerations. For example, any light and weakly coupled Nambu-Goldstone boson such as the familon could carry away a large amount of energy from the interior of stars. In order to be consistent with the standard stellar evolution scenario, the coupling of the Goldstone bosons must be bounded. Unfortunately, this type of calculations can bound only the flavor-diagonal (axial-vector) interactions of the familons with the electrons and the nucleons since second and third generation particles are absent in almost all astrophysical objects. Results of detailed calculations [39] in various stellar objects, such as the Sun, red giants, white dwarfs and neutron stars, led to a family breaking scale larger than $10^7 - 10^9$ GeV with the best limit on $F_{ee}^A \geq 7 \times 10^9$ GeV.

Somewhat better and more reliable constraints on the familon coupling to the first and second generation particles can be obtained from laboratory experiments. As described in the previous section, familons may be produced in flavor changing processes, that can lead to decays like $K \to \pi f$ or $\mu \to e(\gamma) f$, which were studied experimentally with very high sensitivity. The results of these measurements and the resulting family symmetry breaking scales were summarized by Feng *et al.* [37] and reproduced in Table II.1. As we see the

Table II.1: Experimental bounds on the normalized family symmetry breaking scale defined by Eq.'s II.10 and II.11 for the first two generations [37].

Decay	Branching Ratio	F_{ij}
$K^+ \to \pi^+ X^0$	$\mathcal{B} < 3 \times 10^{-10}$ [40]	$F_{sd}^V > 3.4 \times 10^{11}$ GeV
$\mu^+ \to e^+ X^0$	$\mathcal{B} < 2.6 \times 10^{-6}$ [41]	$F_{\mu e}^V > 5.5 \times 10^9$ GeV
$\mu^+ \to e^+ \gamma X^0$	$\mathcal{B} < 1.1 \times 10^{-9}$ [42]	$F_{\mu e} > 3.1 \times 10^9$ GeV

strongest bound on any family symmetry breaking scale is derived from the $K^+ \to \pi^+ X^0$ decay, where X^0 denotes any neutral massless weakly-interacting particle. However, this limits only the vector coupling of the familon since the matrix element $< \pi \mid \bar{d}\gamma^\mu\gamma_5 s \mid K >$ is zero (see details in next section) and so the axial-vector component does not play a role in this decay. On the other hand, $\mu \to e(\gamma)f$ decays has the advantage that both vector and axial-vector couplings come into play and enables us to derive the combined symmetry breaking scale $F_{\mu e}$ as it is the case in [42]. The slightly better limit obtained by [41] bounds only the family symmetry breaking scale with vector coupling ($F^V_{\mu e}$) since the experimenters measured the positrons emerging from polarized muons in a direction opposite to the muon polarization and assumed isotropic positron emission, which holds with the parity conserving vector coupling ($\bar{\mu}\gamma^\mu e$) only.

We now compare these bounds to those available in the third generation. Since all three neutrino species can be found in the core of a supernova, bound on the familon coupling to ν_τ can be obtained by supernova observation (e.g. the supernova SN 1987A in the Large Magellanic Cloud). If the familons emitted by the tau-neutrinos would carry away a substantial amount of the energy, then it would alter the duration of the neutrino pulse and effect the agreement between the theory and observation. The possible effect of the familons were calculated in [43] and the bound on F were deduced in [37] for diagonal and off-diagonal ν_τ coupling. The lower bound on[6] $F^L_{\nu_\tau\nu_\tau}$ is around 2×10^3 GeV at the maximum allowed value of the tau-neutrino mass of 18.2 MeV and it becomes less stringent with decreasing mass.

[6]For neutrinos, it is more convenient to write the familon interaction Lagrangian given by Eq. II.6 in the form

$$\mathcal{L}_f = \frac{1}{F}(\partial_\mu f^a)\bar{\psi}_i\gamma^\mu \left[(g_V + g_A)\frac{1+\gamma^5}{2} + (g_V - g_A)\frac{1-\gamma^5}{2}\right] T^a_{ij}\psi_j, \tag{II.12}$$

where $(1+\gamma^5)/2$ and $(1-\gamma^5)/2$ are the left and right-handed projection operators. Since neutrinos are left handed only, therefore only the first component plays a role in their interactions and we can place a bound only on $F^L_{ij} = F/(g_L T_{ij})$, where $g_L = g_V + g_A$.

The lower limit on the off-diagonal $F^L_{\nu_\tau\nu_\mu}$ scale is smaller by a factor of 1.2.

The astrophysical bounds on the first generation of particles can also be used to infer constraints on flavor diagonal familon couplings to all other particles because the latter ones can induce familon couplings to the electrons or nucleons at loop level [37]. Dominant contribution to the induced coupling is from $Z^0 - f$ mixing, where the Z^0 couples to the e, or u or d quark, and the Z^0 and f are coupled through a loop of a third generation particle. Although these induced couplings are suppressed by loop factors, the first generation couplings are strong enough to give promising bounds on familon couplings to the third generation. This kind of coupling is proportional to the mass square of the particle in the loop, therefore, the best limit can be deduced on the coupling to the top quark:

$$F^R_{tt} > 1.2 \times 10^9 \text{GeV}. \tag{II.13}$$

The bounds on the familon coupling to the b quark and the tau-lepton are

$$\begin{aligned} F^R_{bb} &> 6.1 \times 10^5 \text{GeV} \\ F^R_{\tau\tau} &> 2.5 \times 10^4 \text{GeV}. \end{aligned} \tag{II.14}$$

By taking into account flavor mixing effects, Feng *et al.* [37] also inferred bounds on familon coupling to the third generation quarks from bounds on the first generation obtained from supernova observation:

$$\begin{aligned} F^L_{bb} &> 3 \times 10^4 \text{GeV} \\ F^L_{bs} &> 3 \times 10^6 \text{GeV} \\ F^L_{bd} &> 1 \times 10^7 \text{GeV} \\ F^L_{tt} &> 7 \times 10^5 \text{GeV} \end{aligned} \tag{II.15}$$

Although, some of the bounds derived from astrophysical considerations are fairly stringent, we have to note that they are strongly model-dependent.

More reliable bounds on the family symmetry breaking scale including the third generation were derived by Feng *et al.* [37] from considering familon contributions to neutral meson mixing and existing bounds on rare leptonic decays of B mesons. In the case, when the spontaneously broken family symmetry group is real (e.g $O(N)$ group), then the same real familon field couples to the quark current and its hermition conjugate:

$$\mathcal{L}_f = i\frac{T_{bd}}{F}(\partial_\mu f)[\bar{d}\gamma^\mu(g_V + g_A\gamma_5)b - \bar{b}\gamma^\mu(g_V + g_A\gamma_5)d], \tag{II.16}$$

and therefore contribute to neutral $B^0 - \bar{B}^0$ mixing. The contribution of the familon interaction to the mass splitting is

$$\Delta M^{(f)}_{B^0} \equiv \mid M_{B^0} - M_{\bar{B}^0} \mid \approx \frac{5}{6}\frac{f^2_{B^0} m_{B^0}}{(F^A_{bd})^2}, \tag{II.17}$$

where f_{B^0} is the familon decay constant (see Appendix B). Vector like familon interactions does not contribute to the mass splitting in the heavy quark approximation when $M_{B^0} \approx m_b$. Assuming that the familon contribution is responsible to the total mass splitting and taking $f_{B^0} \approx 175$ MeV, then the resulting conservative lower bound on the family symmetry breaking scale with axial coupling is

$$F^A_{bd} > 6.4 \times 10^5 \text{GeV}. \tag{II.18}$$

Similar bounds can be obtained on F^A_{cu} and F^A_{sd} from the D^0 and K^0 meson mass splitting.

Rare leptonic decays of neutral mesons, such as $B^0 \to \tau^+ e^-$ via familon exchange is possible only if the same familon couples to both quarks and leptons, which is guaranteed in grand unified models, where the quarks and leptons are in the same gauge multiplet. The decay rate is given by [37]

$$\Gamma(B^0 \to \tau^+ e^-) \approx \frac{1}{8\pi}\frac{f^2_{B^0} m^2_\tau (M^2_{B^0} - m^2_\tau)}{(F^A_{bd} F_{\tau e})^2}, \tag{II.19}$$

if we neglect the mass of the lighter lepton. From this type of measurements we can extract bound only on the product $F^A_{bd}F_{\tau e}$. The limits on the flavor scales from current experimental bounds [44] are summarized in Table II.2.

Table II.2: Experimental bounds on the normalized family symmetry breaking scales from rare meson decays [37].

Decay	Branching Ratio	Bound
$B^0 \to \tau^\pm e^\mp$	$\mathcal{B} < 5.3 \times 10^{-4}$	$(F^A_{bd}F_{\tau e})^{1/2} > 3.5 \times 10^3$ GeV
$B^0 \to \tau^\pm \mu^\mp$	$\mathcal{B} < 8.3 \times 10^{-4}$	$(F^A_{bd}F_{\tau \mu})^{1/2} > 3.1 \times 10^3$ GeV
$B^0 \to \mu^\pm e^\mp$	$\mathcal{B} < 5.9 \times 10^{-6}$	$(F^A_{bd}F_{\mu e})^{1/2} > 2.8 \times 10^3$ GeV

A direct experimental bound on the family symmetry breaking scale for the third generation is available in the leptonic sector only. This is based on the measurement of τ decay into a light lepton plus an unobservable particle by the ARGUS collaboration [45]. The results are given in Table II.3. As we can see these bounds on the family symmetry breaking scale

Table II.3: Experimental bounds on the normalized family symmetry breaking scales from $\tau \to \ell X^0$ decays [37].

Decay	Branching Ratio	Bound
$\tau^- \to \mu^- X^0$	$\mathcal{B} < 4.6 \times 10^{-3}$	$F_{\tau\mu} > 3.6 \times 10^6$ GeV
$\tau^- \to e^- X^0$	$\mathcal{B} < 2.6 \times 10^{-3}$	$F_{\tau\mu} > 4.4 \times 10^6$ GeV

are significantly lass stringent for the third generation couplings than for those involving the first two generations (Table II.1).

The lack of experimental bound is more pronounced in the hadronic sector since no

bounds involving the third generation quarks have been reported yet. However, the ALEPH collaboration reported a preliminary limit on the $b \to s\nu\bar{\nu}$ branching ratio $\mathcal{B}(b \to s\nu\bar{\nu}) < 7.7 \times 10^{-4}$ [46], which was scaled by Feng *et al.* [37] to get a limit on the inclusive decay $b \to sf$:

$$\mathcal{B}(b \to sf) < 1.8 \times 10^{-3}. \tag{II.20}$$

This corresponds to a bound on the normalized family symmetry breaking scale of

$$F_{bs} > 6.1 \times 10^{7}\text{GeV}. \tag{II.21}$$

II.4 The goal of the analysis

As we saw in the previous section, constraints on transitions mediated by familons between the first and second generations were studied extensively in contrast to the third generation where existing experimental bounds are much weaker (in the leptonic sector) or do not exist at all (in the hadronic sector). At the same time, models have been proposed [47] in which the strength of the familon coupling to the fermions is related to the mass hierarchy of the particle generations, and therefore familons most strongly coupled to the third generation.

The familon interactions described by the Lagrangian Eq. II.6 can induce the flavor changing decay of the b quark to d or s quark $b \to (d, s)f$, which can lead to the decay of the B meson via the tree level diagram shown on Fig. II.1. As we will see in the next section, the B decay to a pseudoscalar meson plus a familon, $B \to hf$ where h stands for π or K meson, is governed by only the vector-type familon interaction. On the other hand, the decay $B \to Vf$, where V is a vector meson, such as the ρ or K^* meson, goes through axial-vector coupling only.

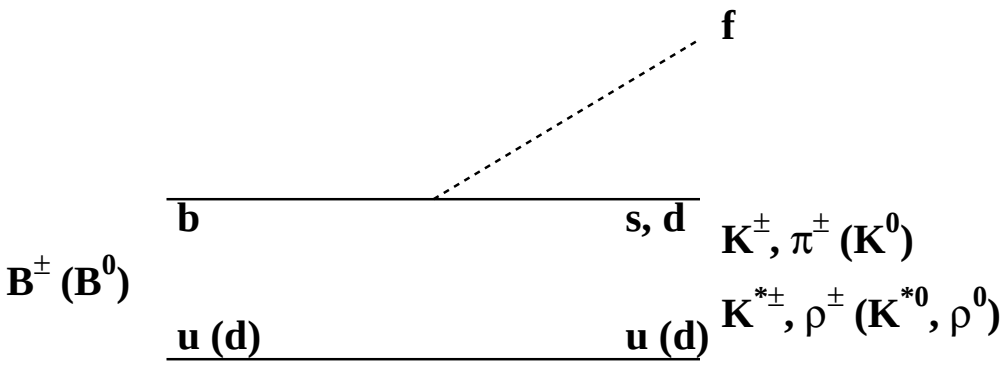

Figure II.1: Feynmann graph of B meson decays via the $b \to (d,s)f$ mechanism.

Although these exclusive B decays have smaller branching fractions than the inclusive $b \to q_d f$ ($q_d = d, s$) decays, they have clear experimental signature due to the simple two-body kinematics. However, the vector mesons, K^* and ρ, are short lived resonances, which decay by the strong interaction: $K^* \to K\pi$ and $\rho \to \pi\pi$. Due to the short lifetime these resonances have a wide mass distribution shown on Fig. II.2 as it is expected from the energy-time uncertainty relation. Because of the wide invariant mass distribution, these decay modes are highly contaminated with combinatoric background, when two unrelated K (π) and π mesons are identified as a K^* (ρ) candidate by accident. In contrast, the $B \to hf$ decays have the advantage that they exhibit a clean experimental signature with a single high energy $\pi^\pm/K^\pm$ meson or a K^0_S present in the final state, which can be detected with high efficiency, without significant background from other B decays. Hence, we expect higher sensitivity for the latter decay modes and we focus on them in this analysis.

We search for the $B^\pm \to h^\pm X^0$ and $B^0 \to K^0_S X^0$ decays, where X^0 represents any massless neutral particle that, like the familon, couples to ordinary matter very weakly. The

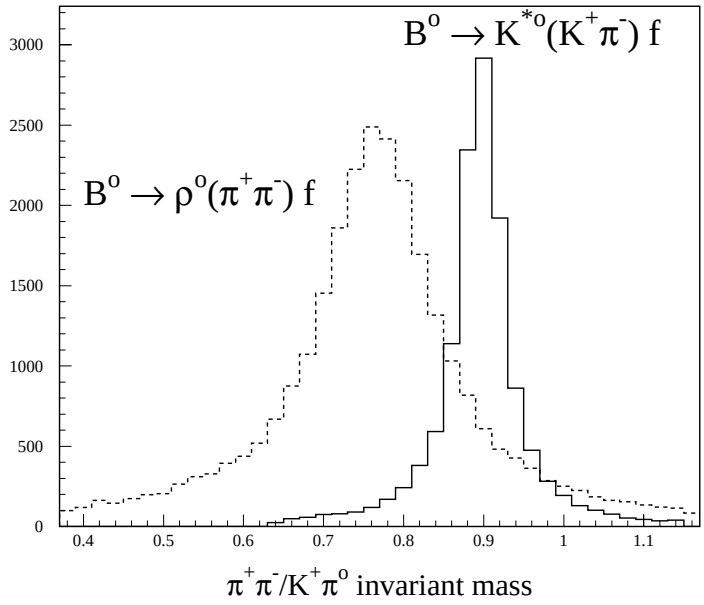

Figure II.2: Invariant mass distribution (in GeV/c^2) of $K^+\pi^-$ (solid histogram) and $\pi^+\pi^-$ pairs (dashed histogram) in Monte-Carlo simulated $B^0 \to K^{*0} f$ and $B^0 \to \rho^0 f$ events.

lack of signal allows us to obtain experimental bound on the vector coupling of the familon to third generation hadrons for the first time. The analysis is sensitive to new physics including any other massless weakly coupled neutral particles as well. However, we would like to emphasize that, it is equally important to study the $B \to Vf$ decays in order to place a constraint on the axial-vector coupling of the familon.

II.5 $B \to hf$ decay rate

In this section we will show that there is a significant difference in the decay mechanism between the two exclusive decays $B \to hf$ ($h = \pi, K$) and $B \to Vf$ ($V = \rho, K^*$) and derive the decay rate for $B \to hf$ decays.

The differential decay rate of a particle with mass M decaying to a two-body final state

is given by (see e.g. [48])

$$d\Gamma = \frac{1}{2M} \mid \mathcal{M} \mid^2 dLIPS^{(2)}, \tag{II.22}$$

where $\mathcal{M}$ is the decay amplitude (interaction matrix element) and $dLIPS^{(2)}$ is the two-body Lorentz Invariant Phase Space element. The later quantity is defined by

$$dLIPS^{(2)} = \frac{1}{16\pi^2}\frac{p_{\text{c.m.}}}{\sqrt{s}}d\Omega, \tag{II.23}$$

where $\sqrt{s}$ is the center of mass energy, which is equal to the mass of the parent particle in case of decay, and $p_{\text{c.m.}}$ is the magnitude of the 3-momentum of either decay products in the center of mass frame. In order to obtain $p_{\text{c.m.}}$ we apply the principle of momentum and energy conservation for the case of a final state consisting of a massive particle (with mass m) and a massless familon:

$$M = \sqrt{p_{\text{c.m.}}^2 + m^2} + p_{\text{c.m.}}, \tag{II.24}$$

which gives

$$p_{\text{c.m.}} = \frac{M^2 - m^2}{2M}. \tag{II.25}$$

Then the differential decay rate is

$$d\Gamma = \frac{1}{64\pi^2}\frac{M^2 - m^2}{M^3} \mid \mathcal{M} \mid^2 d\Omega. \tag{II.26}$$

The decay amplitude is the matrix element of the interaction Lagrangian that governs the decay sandwiched between the initial and final states (here D denotes the daughter meson, which can be either pseudoscalar h or vector V):

$$\begin{aligned}
\mathcal{M} &= - < D(p')f(q) \mid \mathcal{L}_f \mid B(p) > \\
&= -\frac{1}{F} < D(p')f(q) \mid \partial_\mu f \bar{q}_d \gamma^\mu (g_V + g_A\gamma^5) T_{bq_d} b \mid B(p) > \\
&= \frac{i}{F} q_\mu < D(p') \mid \bar{q}_d \gamma^\mu (g_V + g_A\gamma^5) T_{bq_d} b \mid B(p) > \\
&= \frac{i}{F} T_{bq_d} q_\mu \left[g_V < D(p') \mid \bar{q}_d \gamma^\mu b \mid B(p) > + g_A < D(p') \mid \bar{q}_d \gamma^\mu \gamma^5 b \mid B(p) > \right].
\end{aligned} \tag{II.27}$$

In Eq. II.27 p and p' are the 4-momentum of the B meson and the daughter meson D, respectively, $q = p - p'$ is the 4-momentum transfer to the familon, and the q_d stands for the relevant d or s quark field operator depending on the quark content of D.

The transition amplitude $\mathcal{M}$ is different for $B \to hf$ decays containing pseudoscalar meson and for $B \to Vf$ decays with a vector meson in the final state. Let's see first the case of the pseudoscalar meson final state, i.e. $D = h$ in Eq. II.27. Since both h and B are pseudoscalar mesons with $J^P = 0^-$ spin-parity, the axial-vector matrix element must vanish[7] and only the vector current contribute:

$$\mathcal{M}_h = i\frac{T_{bq_d} g_V}{F} q_\mu < h(p') \mid \bar{q}_d \gamma^\mu b \mid B(p) > . \tag{II.28}$$

The matrix element of the vector current can be expressed in terms of two dimensionless form factors $F_0(q^2)$ and $F_1(q^2)$ [50]

$$< h(p') \mid \bar{q}_d \gamma^\mu b \mid B(p) >= (p + p')^\mu F_1(q^2) + \frac{M^2 - m^2}{q^2} q^\mu \left[F_0(q^2) - F_1(q^2)\right], \tag{II.29}$$

where $F_1(0) = F_0(0)$ is required to remove the singularity at $q^2 = 0$. In our case $q^2 = q_\mu q^\mu = E^2 - \vec{q}^2 = m_f^2 = 0$ and hence the second term vanishes. Therefore, the decay amplitude is simply

$$\mathcal{M}_h = i\frac{T_{bq_d} g_V}{F} q_\mu (p + p')^\mu F_1(0) = i\frac{T_{bq_d} g_V}{F} (M^2 - m^2) F_1(0). \tag{II.30}$$

Since $q_\mu = (p - p')_\mu$, we used the identity $(p - p')_\mu (p + p')^\mu = p^2 - p'^2 = M^2 - m^2$ to obtain the second form.

Let's see now the case of decay to a vector meson plus familon $B \to Vf$. In this case the hadronic matrix element of the vector current does not vanish and the two matrix element in

[7] From general considerations of Lorentz invariance follows that the matrix element of an axial-vector current A^μ between two spinless meson having the same intrinsic parity is zero, $< 0^\pm \mid A^\mu \mid 0^\pm >\equiv 0$, see e.g. Chapter 10 in [49]

Eq. II.27 can be parameterized in terms of four independent form factors, $V(q^2)$ and $A_i(q^2)$ with $i = 0, 1, 2$, [50]:

$$\begin{aligned}
< V(p') \mid \bar{q}_d \gamma^\mu b \mid B(p) > &= 2i\epsilon^{\mu\nu\alpha\beta} \frac{\epsilon_\nu p'_\alpha p_\beta}{M+m} V(q^2), \\
< V(p') \mid \bar{q}_d \gamma^\mu \gamma^5 b \mid B(p) > &= (M+m) \left[\epsilon^\mu - \frac{\epsilon \cdot q}{q^2} q^\mu \right] A_1(q^2) \\
&\quad - \epsilon \cdot q \left[\frac{(p+p')^\mu}{M+m} - \frac{M-m}{q^2} q^\mu \right] A_2(q^2) \\
&\quad + 2m \frac{\epsilon \cdot q}{q^2} q^\mu A_0(q^2).
\end{aligned} \tag{II.31}$$

However, the tensors associated with $V(q^2)$, $A_1(q^2)$ and $A_2(q^2)$ are orthogonal to q_μ (see for example Chapter 16 in [49]) so that these terms vanish when we substitute Eq. II.31 to the expression of $\mathcal{M}$ (Eq. II.27), resulting:

$$\mathcal{M}_V = 2im \frac{g_A T_{bq_d}}{F} \epsilon \cdot q A_0(0). \tag{II.32}$$

As we can see, only the vector coupling plays a role in the decay to a pseudoscalar meson $B \to hf$ ($h = \pi, K$), while the decay to a vector meson $B \to Vf$ ($V = \rho, K^*$) goes through axial-vector coupling only. Using these different decay modes we can obtain information separately on the vector and axial-vector components of the familon interaction. Since we focus our attention to the $B \to hf$ decays in this thesis, we derive the partial decay rate for these modes.

By substituting the decay amplitude $\mathcal{M}_h$ (Eq. II.30) in Eq. II.26, the differential decay rate for $B \to hf$ decays reads as

$$d\Gamma(B \to hf) = \frac{1}{64\pi^2} \frac{(M^2 - m^2)^3}{M^3} \frac{\mid F_1(0) \mid^2}{(F^V_{bq_d})^2} d\Omega. \tag{II.33}$$

After integrating over the total solid angle $\int d\Omega = 4\pi$, the partial decay rate is equal to

$$\Gamma(B \to hf) = \frac{1}{16\pi} \frac{(M^2 - m^2)^3}{M^3} \frac{\mid F_1(0) \mid^2}{(F^V_{bq_d})^2}, \tag{II.34}$$

where we used the definition of the normalized family symmetry breaking scale with vectorial coupling, $F^V_{bq_d}$, defined by Eq. II.11.

By measuring the decay rate, which is related to the branching ratio ($\mathcal{B}$) of the decay through the formula

$$\Gamma(B \to hf) = \mathcal{B}\Gamma = \frac{\mathcal{B}}{\tau}, \tag{II.35}$$

where Γ and τ are the total decay rate (decay width) and life-time of the B meson, respectively, we can extract the family symmetry breaking scale with vectorial coupling, $F^V_{bq_d}$. To do this we also need the value of the weak transition form factor $F_1(q^2)$ at zero momentum transfer.

The weak transition form factors are usually calculated by using non-perturbative methods, such as constituent quark models, QCD sum rules or lattice QCD, which makes the theoretical uncertainties quite large. The form factor $F_1(q^2)$ can be parameterized by

$$F_1(q^2) = \frac{F_1(0)}{1 - q^2/M_P^2}, \tag{II.36}$$

where M_P^2 is the pole mass. The results from different calculations are compared in a recent paper by Melikhov and Stech [51]. The values for $F_1(0)$ ranges from $0.25 - 0.36$ in case of $B \to K$ transitions, while they are between 0.27 and 0.305 for $B \to \pi$ transitions. These two ranges are consistent since the two form factors are expected to agree in the flavor symmetric limit. We adapted the value $F_1(0) = 0.25$ resulting from QCD sum rules [52], which gives the most conservative (i.e. the lowest) value of the symmetry breaking scale for a particular decay rate, to extract both F^V_{bd} and F^V_{bs} from our experiment.

CHAPTER III

EXPERIMENTAL APPARATUS

The data analyzed in this study were accumulated by the CLEO II detector located at the Cornell Electron Storage Ring (CESR) at Cornell University in Ithaca, NY. In this chapter the properties of CESR and CLEO are described in some detail.

III.1 The Cornell Electron Storage Ring (CESR)

The Cornell Electron Storage Ring was constructed in 1977-79, and started operation in 1979. CESR is a symmetric[1] electron-positron collider, in which the electrons and positrons travel in opposite direction and collide head-on at the only interaction point on the south side of the ring. The center of mass energy of the collisions ($\sqrt{s} = 2E_{\rm beam}$) can be adjusted between $9 - 12$ GeV but CESR usually operates around the energy of the $\Upsilon(4S)$ resonance at $\sqrt{s} = 10.58$ GeV.

The acceleration of the electrons and positrons to the desired energy is performed separately. First the positron beam is accelerated and stored in the storage ring, followed by the acceleration of the electron beam. The main components of the accelerator system are the linear accelerator (LINAC), the synchrotron and the storage ring itself. They are shown on Fig. III.1 along with the different experimental areas.

The acceleration process starts at the electron source where electrons are emitted from a heated filament. The LINAC pre-accelerates the electrons to 300 MeV energy under the

[1]That is the energy of the electron and positron beam is equal. In this arrangement, all of the kinetic energy of the particles is converted into new matter in the collision and there is no energy loss in the form of recoil motion of the collision products.

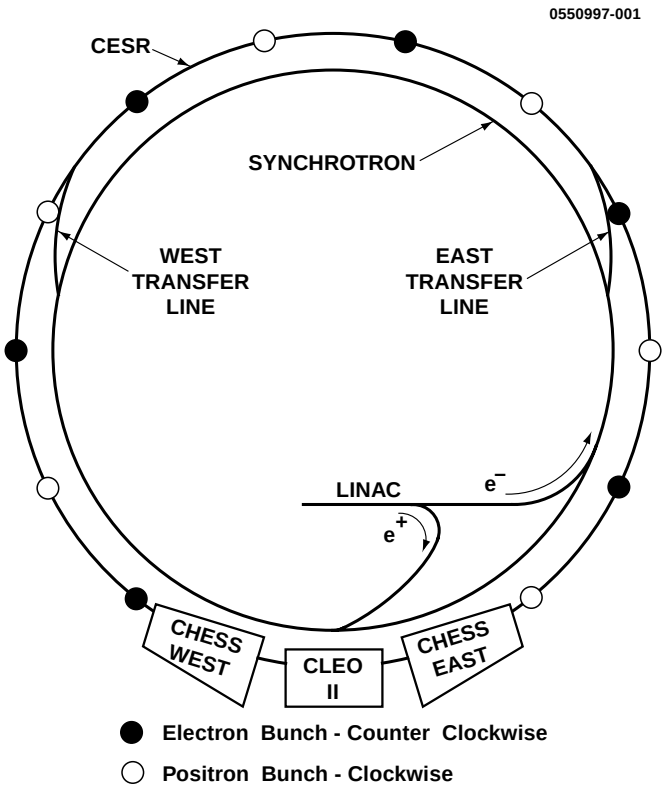

Figure III.1: Layout of the Cornell Electron Storage Ring.

action of a microwave electric field. On the other hand, positrons are produced by pair production at about halfway in the LINAC where the electrons strike a tungsten foil at approximately 140 MeV energy. The positrons are separated from other particles produced in the collision and accelerated up to 200 MeV energy in the remaining length of the LINAC.

In the next step, the electrons or positrons are injected into the synchrotron, in which they travel in a circular orbit under the influence of 192 3 m long bending dipole magnets. Further acceleration is achieved by four linear accelerators placed among the bending magnets. It takes approximately $4,000$ revolutions or about 0.01 s for the particles to reach the required energy around 5 GeV when they are transferred into the storage ring.

The storage ring, which has a circumference of 768 m shares the same tunnel 12 m

underground with the synchrotron. It uses the same guide field principle as the synchrotron to keep the particles on orbit while quadrupole and sextuple magnets are focusing the beams. The particles circulate in the ring about $390,000$ times per second for about an hour, which requires good quality vacuum ($\sim 10^{-9}$ torr) and very precise tuning of the magnets to minimize beam scattering. The energy spread of the beam at 5.3 GeV is $\sim$ 3.8 MeV. Due to the curved orbit, each electron and positron looses approximately 0.5 MeV energy per revolution via synchrotron radiation. The synchrotron radiation, which is emitted in the form of high energy X-rays, is a valuable research tool used by the Cornell High Energy Synchrotron Service (CHESS) facility for material science, biology and other interdisciplinary studies. The lost energy is restored to the beam by 500 MHz radio-frequency cavities placed at a few places among the magnets.

The electrons and positrons are not continuously distributed along the ring but they travel in bunches. Since the electron and positron bunches are counter-rotating in the same ring, two pairs of electrostatic separators yield differential horizontal closed orbits ('pretzel' orbits) to avoid collision outside the interaction region. At the beginning of operations three and later seven nearly equally spaced bunches (shown on Fig. III.1) were directed into head-on collisions. In order to significantly increase the number of bunches in each beam the configuration was changed in 1994 so that the bunches collide with a small horizontal crossing angle of ± 2.1 mrad. Since that time CESR has been operating with nine trains of bunches and has steadily increased the number of bunches in each train from the initial two to the current five. With the total 45 bunches present CESR can produce up to 370 mA current per beam. The successive improvements in the accelerator technology at Cornell were crucial to continuously increase the luminosity of CESR.

The performance of a collider is quantitatively measured by its luminosity $\mathcal{L}$, which is

the coefficient of proportionality between the event rate (R) of a given process and the cross section (σ) of that particular process

$$R = \mathcal{L}\sigma. \tag{III.1}$$

The luminosity depends on the beam parameters, such as the transverse bunch profile, number of particles in the bunches and the collision rate between the bunches. The luminosity at CESR/CLEO is measured by processes like $e^+e^- \rightarrow \mu^+\mu^-$, which are characterized by high and well-known cross section and have high efficiency in the detector. Recently, an instantaneous luminosity of 1.25×10^{33} cm^{-2}s^{-1} has been achieved. However, the most critical quantity is not the instantaneous luminosity but its integrated value over a given time-interval $\int \mathcal{L}dt$, which is measured in nb^{-1}, pb^{-1} or fb^{-1}.[2] Fig. III.2 demonstrates how the monthly integrated luminosity of CESR increased during the course of operation. The best integrated luminosity values delivered by CESR are 73pb^{-1} during a day (in April 2001), 1.55fb^{-1} in the month of December, 2000, and 6.35fb^{-1} in the year of 2000.

[2]They are read as 'inverse nano-/piko-/femto-barn'. Since 1b= 10^{-24}cm^2, they are equivalent to 10^{33}cm^{-2}, 10^{36}cm^{-2} and 10^{39}cm^{-2}, respectively.

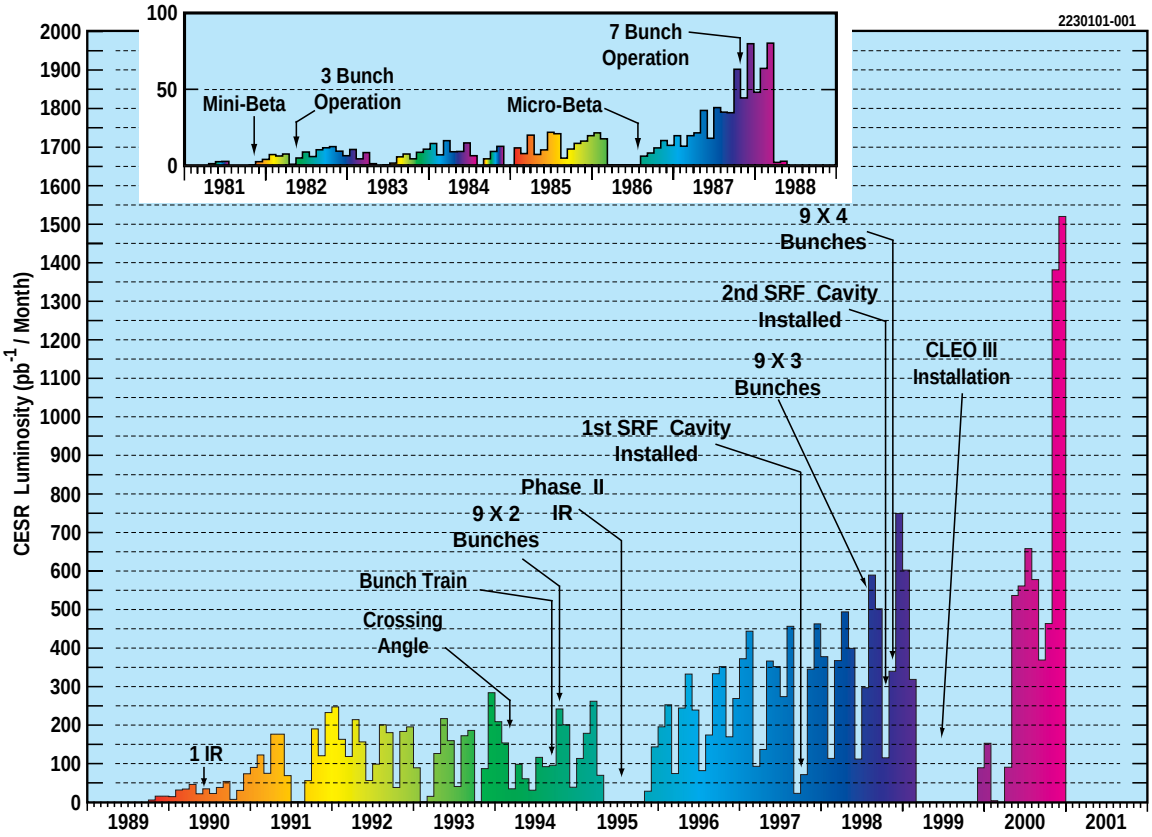

Figure III.2: CESR's monthly integrated luminosity from 1989 – 2001.

III.2 The CLEO II Detector

The first detector at the south interaction region of CESR was installed in September 1979. In the course of numerous upgrades CLEO has received new and improved detector sub-systems and finally reached the status that we call CLEO II [54] in 1989. The purpose of the detector is to measure the momentum, energy, charge, type, starting position and other important parameters of the majority of particles created in the e^+e^- annihilation at the center of the detector.

CLEO II is a multipurpose detector containing more than 25,000 individual detection elements designed to provide excellent charged and neutral particle reconstruction efficiency

and resolution. The main components of the detector are the charged particle tracking system, the time of flight system, the crystal calorimeter, the superconducting coil and the muon tracking system. Vertical cross-section of the detector parallel to the beam line can be seen on Fig. III.3. CLEO II covers approximately 95% of the total solid angle only since it has to provide space for the beam pipe passing through and has to accommodate the rear-earth-cobalt (REC) permanent magnet quadrupoles, which are the final elements of the beam-focusing system near the interaction region.

Unfortunately, the detector is not able to measure all particles created in the e^+e^- annihilation. Charged particles are missed due to the finite solid angle of the detector, the finite efficiency, and interaction with the detector material, which can distort the measurement. However, the main difficulties are associated with neutral particles, whose detection efficiency depends on the particle type very much. The K^0-short can be measured easily trough its decay to a positively and a negatively charged pion at a secondary vertex position distinctive from the primary interaction point from which most of the particles originate. Photons can generally be measured quite accurately in the crystal calorimeter. Similarly, π^0's decaying almost exclusively to two gamma photons are easily detectable, which is important since π^0's make up a large portion of the neutral particle spectrum. On the other hand, detection of neutron and K^0-long is extremely difficult since they decay to charged particles usually outside the fiducial volume of the detector. Finally, neutrinos, which are produced very often in quark and lepton decays are impossible to measure due to their very weak interaction with the detector elements.

A typical $e^+e^- \to \Upsilon(4S) \to B\bar{B}$ event reconstructed with the detector is demonstrated on Fig. III.4.

Trajectories of charged particles are reconstructed using a system of three concentric

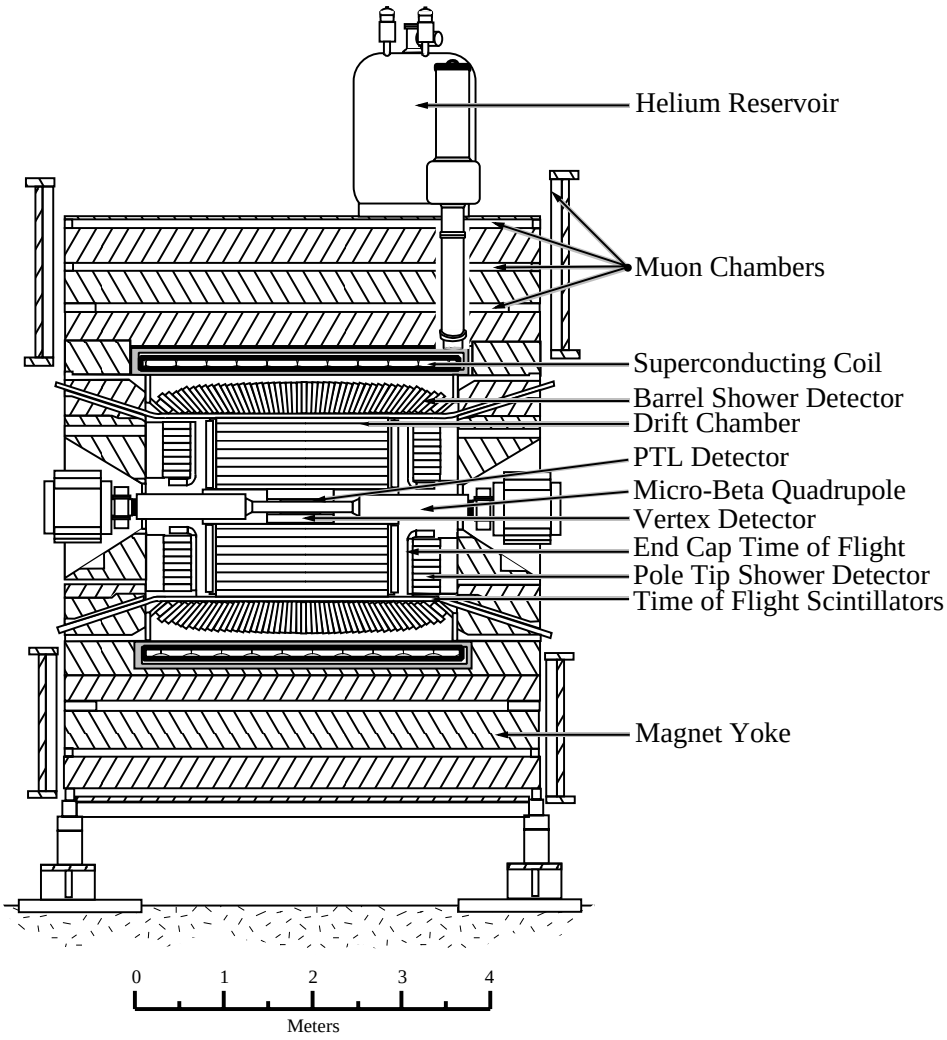

Figure III.3: Side view cross-section of the CLEO II detector.

cylindrical wire chambers: a 6-layer straw-tube chamber, a 10-layer precision drift chamber, and a 51-layer main drift chamber. The main drift chamber also provides a measurement of the specific ionization loss (dE/dx) used for particle identification. The time of flight system measures the flight time of particles, which combined with the momentum also helps in identifying the particle type. Photons are detected in the CsI electromagnetic calorimeter only but charged particles reaching the calorimeter also leave their distinctive signature in

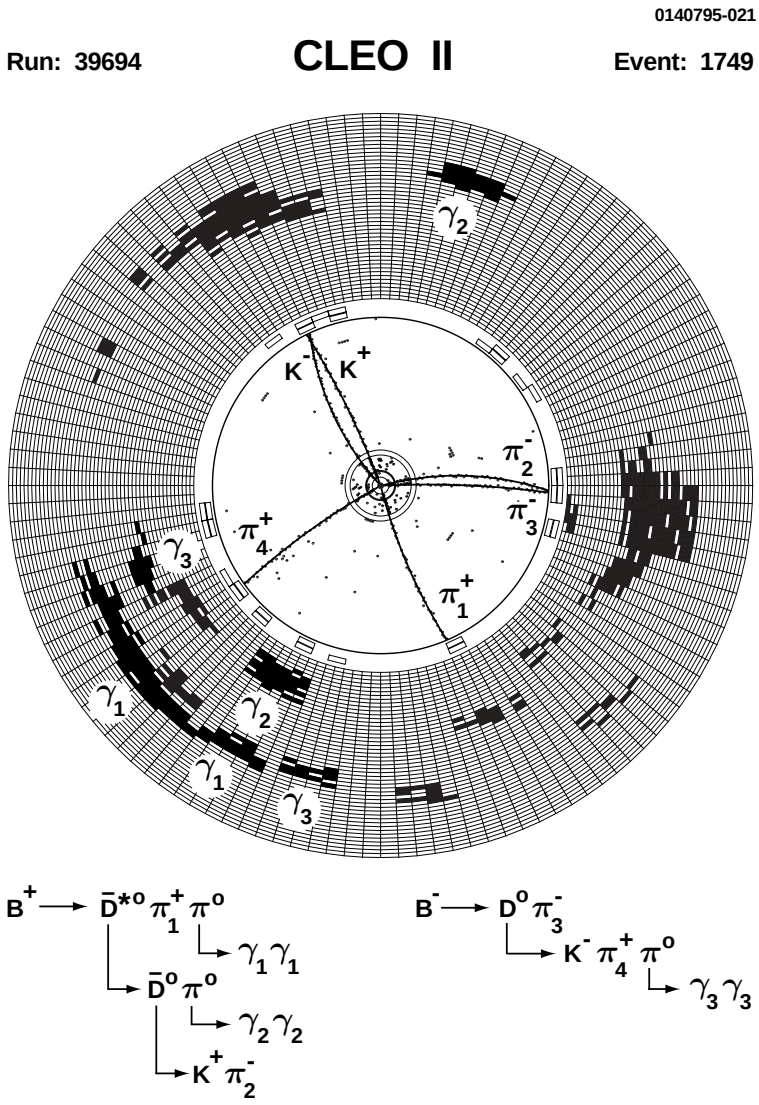

Figure III.4: A reconstructed event in the CLEO II detector.

it. The superconductive magnetic coil outside the crystal calorimeter induces 1.5 T uniform axial magnetic field. Under the influence of this field, charged particles travel on a curved trajectory (helix) through the drift chamber and their momentum and charge can be computed from the curvature of the track. The muon chambers consisting of proportional counters embedded at various depths in the steel absorber distinguish the highly penetrating muons from other charged particles.

The CLEO II detector went through a major upgrade in 1995, when the innermost straw-tube chamber was replaced with a three-layer, double-sided silicon vertex detector [55], and the gas in the main drift chamber was changed from an argon-ethane to a helium-propane mixture. These modifications led to an improved particle identification and momentum resolution. Approximately 2/3 of the data used in this analysis were collected with the upgraded CLEO II.5 detector.

The detector subsystems are described in detail in the following sections.

III.2.1 Tracking Detectors

The three wire chambers of the tracking system rely on the same principle of work but different design specifications make them suitable for different purposes, and therefore, the combined system can achieve a better performance than a single chamber. All three wire chambers have a cylindrical shape with the common axis aligned with the beam line. They are filled with an appropriate gas mixture and contain only hundreds or thousands of thin wires strung parallel to the symmetric axis. The wires are arranged in a cell structure so that each sense (or anode) wire is surrounded by several field (or cathode) wires. The charged particle traveling through the detector leaves a track behind by ionizing the atoms of the gas. The electric field in a cell located along the path of the particle drives the ionization electrons toward the sense wire at the center of the cell. The accelerating primary electrons gain enough energy to produce an avalanche of thousands of electrons through secondary ionization. The electron shower reaches the sense wire within a few nanosecond and produces an electric signal. By measuring the time between the pulse in the wire and the arrival of the particle in the detector and knowing the drift velocity of the electrons in the gas (~ 50 μm/ns) the closest approach of the particle to the sense wire can be determined and the

path of the particle can be reconstructed with high precision in the $r-\phi$ plane (azimuth measurement).

The polar angle measurement (that is measuring the hit location in the z-direction) are usually achieved by the combination of segmented cathode pads made of aluminium foil bonded on Mylar sheets, installed on the inner surface of the chambers, which measures the image charge of the electron avalanche in the adjacent cells. To provide further measurement in the longitudinal direction the charge at both ends of the wires can be measured (charge division measurement) as well since an asymmetric hit on the wire results in different charge measurement at the two ends. The drift chambers provide a uniform acceptance in azimuth for the polar angles $26^\circ < \theta < 154^\circ$ ($|\cos\theta| < 0.9$), however, track reconstruction efficiency is slightly higher for $|\cos\theta| < 0.71$ due to the reduction of layers in the main drift chamber.

Precision Tracking Layer Detector

The innermost wire chamber in CLEO II is the Precision Tracking Layer (PTL) detector, which is installed between the beam pipe and the vertex detector. The 3.5 cm radius beam pipe is made of beryllium to minimize the amount of material in the way of particles entering the detector. It has a thickness of 0.5 mm with a 25 μm silver coating on the inside surface for protecting the detector from synchrotron radiation.

The 50 cm long PTL is a 6-layer straw-tube drift chamber with 64 axial sense wires in each layer. The sense wires are made of 15 μm gold plated tungsten. The field cage for each wire is defined by an aluminized Mylar tube instead of cathode wires. To resolve the left-right ambiguity, that is, to tell which side of the center of the cell the particle passed, the layers are shifted by half a cell in azimuth from layer to layer (see Fig. III.5). The sense wires are kept at +1500 V relative to the field tube. The PTL detector was filled with $50\%-50\%$

argon-ethane (C_2H_6) mixture initially, but later it was operated with di-methyl-ether.

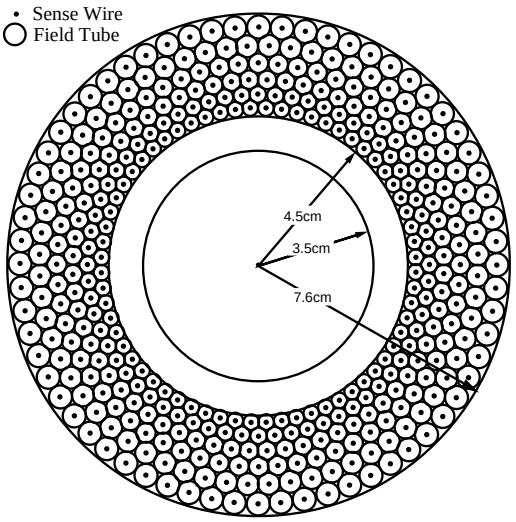

Figure III.5: Cross section of the PTL detector.

The PTL measured the azimuthal direction of the particles near the interaction point with a precision of around 50 μm, which is essential to separate secondary vertices from the primary interaction point. However, it did not provide longitudinal (z) measurement.

Vertex Detector

The Vertex Detector (VD) is an intermediate drift chamber installed between the PTL detector (the SVX later) and the outer main drift chamber. It contains 800 Ni-Cr sense wires and 2272 Al field wires arranged into 10 layers of small hexagonal cells as shown on Fig. III.6. All wires are axial, and are divided into two groups with 64 cells per layer in the first five layers and 96 cells in each of the outer five layers. Sequential layers are off-set by half a cell to resolve left-right ambiguity. The sense wires are kept at voltages +2200 V and

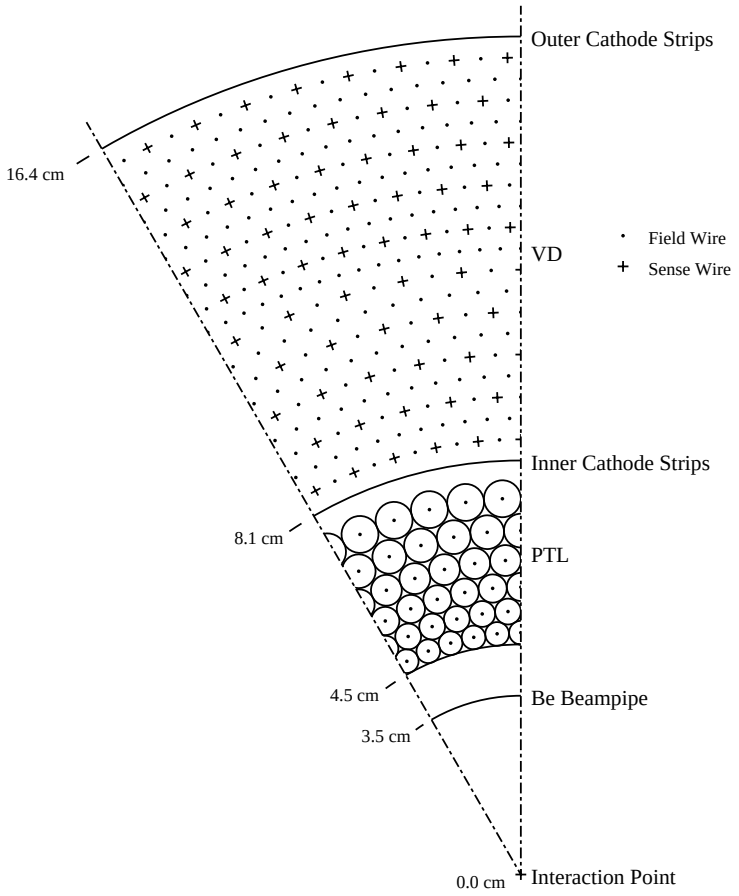

Figure III.6: A section of the VD and PTL detectors.

+2400 V depending on the cell size while the field wires are grounded. The detector operates with 50%− 50% argon-ethane gas mixture at a pressure of approximately 1.4 atmosphere.

The VD is more suitable for early track separation than the main drift chamber because of its smaller cell size. In addition, the momentum of low momentum tracks, which can reach only a few layers in the outer drift chamber due to their high curvature, is better measured in the VD. The precision of the position measurement in the $r-\phi$ plane is around $100-150$ μm. Longitudinal (z) measurement is provided by two layers of segmented cathode

pads divided into 8 azimuthal sections on the inner surfaces of the wire chamber walls (Fig. III.7). Segmentation along the beam direction is $\sim 6-7$ mm. The longitudinal measurement is enhanced by charge division measurement on both ends of the sense wires. These methods give a resolution of ~ 750 μm in the z direction.

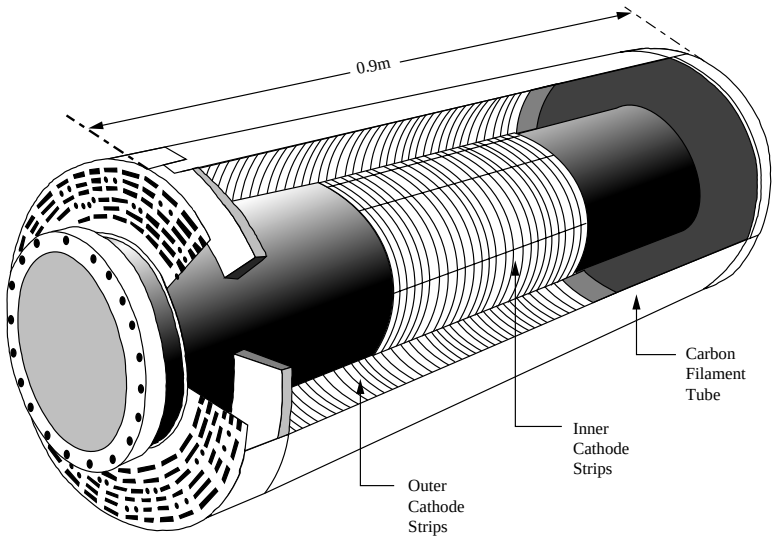

Figure III.7: Cathode strips on the Vertex Detector.

Outer Drift Chamber

The main (or central) Drift Chamber (DR) is a 2 m long, 1.9 m diameter, 51-layer wire chamber containing 12,240 sense wires and 36,240 field wires. The chamber used to operate with a 50%$-$ 50% argon-ethane gas mixture at 1 atmosphere until the CLEO II.5 upgrade when the gas was changed to a 60%$-$ 40% helium-propane mixture. The DR has small rectangular cells with one sense wire in the center surrounded by 8 field wires. The sense

wires are 20 μm diameter gold plated tungsten while the field wires are 110 μm gold plated Al (in the inner 40 layers) or gold plated Co-Be (in the outer 11 layers). Sense wire voltage is kept at +2000 V while the field wires are grounded.

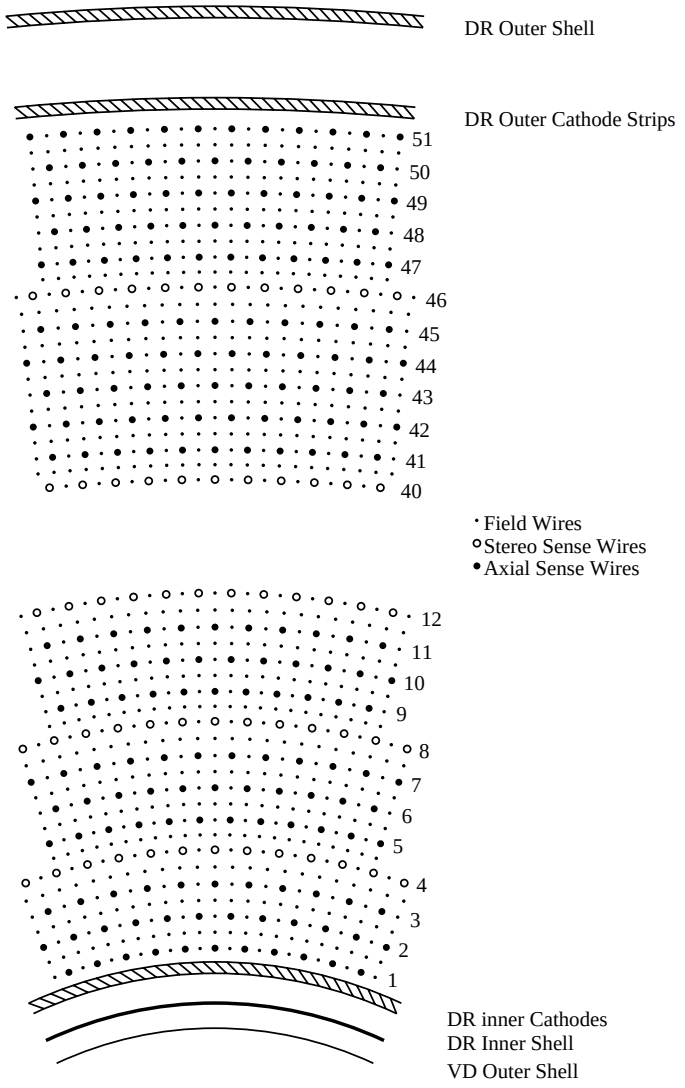

Figure III.8: Wire layer structure in the main Drift Chamber.

Out of the 51 concentric rings of wire, 40 contains axial wires, while 11 contains stereo

wires where one end of the ring is twisted with respect to the other end creating a small stereo angle $3^\circ - 7^\circ$. The axial layers are arranged into groups with three or five sense-wire layers. Each group contains layers with equal number of wires per layer (96 in the first group and 384 in the last one). Adjacent layer groups with different number of wires per layer are separated by a stereo layer. Like in the other two wire chambers, the cells are shifted by half a cell in neighboring axial layers to resolve the left-right ambiguity. The structure of the cells and layers of the DR is shown on Fig. III.8.

The axial sense wires can measure the position of the particle in the $r - \phi$ plane with a precision of $100 - 200$ μm depending on the distance of the track from the sense wire in the cell. The longitudinal (z) position is provided by the stereo sense wires and segmented cathode layers. The inner cathode layer is divided into 16 sections in azimuth while the outer cathode has 8 azimuthal sections. The longitudinal segmentation is 1 cm.

Charged particles are not detected below a momentum of 65 MeV/c because of the material in the particle path. The transverse momentum resolution of the detector is $\delta p_t = 64$ MeV/c at $p_t = 5.28$ GeV/c. Resolution in azimuthal (ϕ) and polar (Θ) angle is $\delta\phi = 1$ mrad and $\delta\Theta = 4$ mrad, respectively.

Besides the position and momentum measurement, the DR also provides particle identification information based on the specific ionization energy loss (dE/dx). The energy loss of a charged particle in the gas of the main drift chamber depends on the particle's velocity. Hence, particles with the same momentum but different mass lose different amount of energy per unit distance when passing through the DR. The pulse height on an anode wire situated along the particle's track is proportional to the energy loss in that particular cell. In order to statistically increase the significance of the measurement, the truncated mean of

all the individual hit pulse heights[3] associated with a particular track is taken as the best estimator of dE/dx for that track. Drift distance, entrance angle and polar angle corrections are applied to each individual hit. Fig. III.9 shows dE/dx as the function of the momentum for different particle types. The separation between the different particle types is very good at low momentum but it diminishes as the momentum increases.

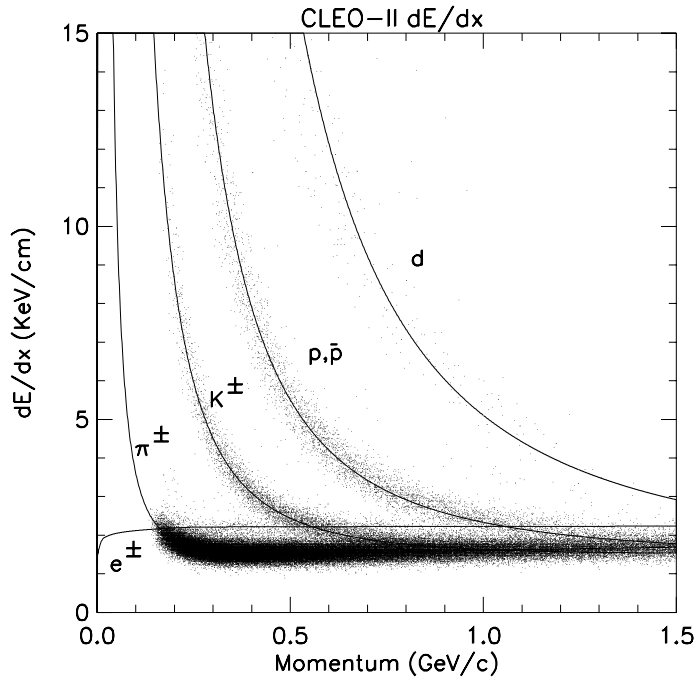

Figure III.9: Ionization energy loss (dE/dx) as the function of the momentum.

[3]The distribution of the individual pulse heights along a given track does not follow a Gaussian distribution. There is an enhancement at the high side of the distribution (Landau tail) due to hard collisions leading to large fluctuations of the mean pulse height. In order to reduce the Landau tail, $30-40$ % of the highest pulse heights are dropped when calculating the mean. At the same time, the lowest 5 % of the pulse heights are also dropped to reduce noise effects.

III.2.2 Silicon Vertex Detector

The innermost wire chamber, the PTL detector, was replaced with a three-layer double-sided Silicon Vertex Detector (SVX) in 1995 during the upgrade of the detector from CLEO II to II.5. At the same time, the radius of the Be beam pipe was reduced to 2.0 cm permitting the placement of the first layer of the SVX detector at a distance of only 2.35 cm from the beam axis. The layout of the SVX is shown on Fig. III.10.

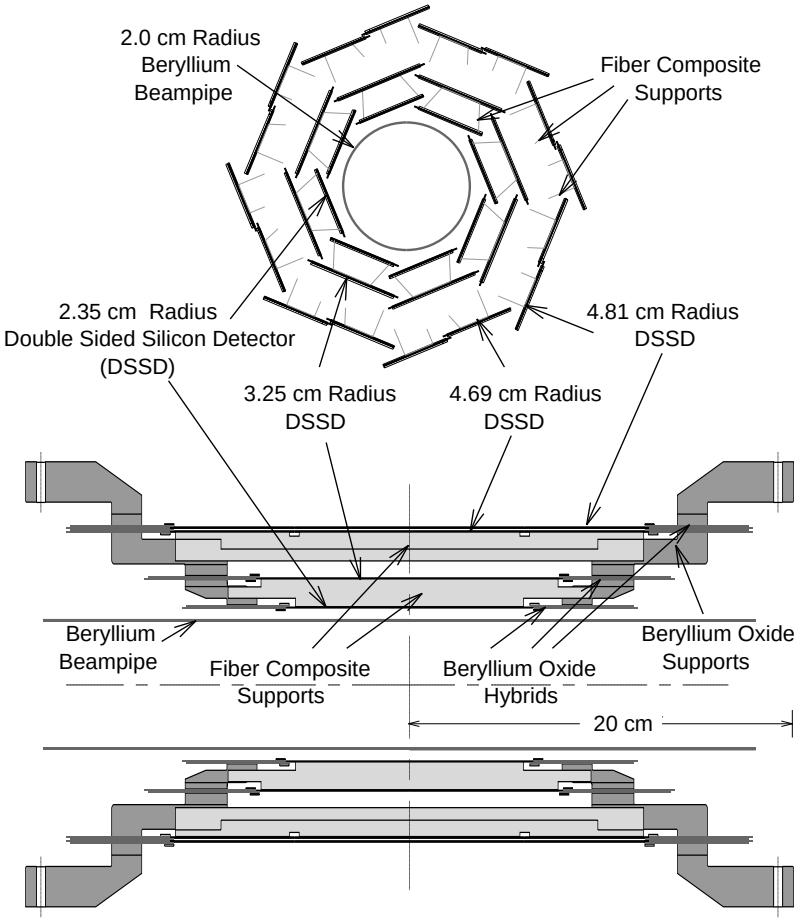

Figure III.10: End view (top) and side view (bottom) of the SVX Detector.

The detector consists of 96 silicon wafers, each of them containing implants on both sides. The inward side has n-implant stripes separated by 105 μm and arranged perpendicular to the beam axis for position measurement in z-direction. The opposite side is covered by p-implant stripes parallel to the beam axis and separated by 112 μm for position measurement in azimuth. When a charged particle crosses a silicon detector, it liberates charge carriers (electron-hole pairs) in the depleted $p-n$ junction, which are collected out on both sides of the wafers by the applied bias voltage. The SVX is inherently more accurate than the PTL detector without introducing significant amount of extra material. The SVX has a position resolution of $12-18$ μm, which leads to precise vertex reconstruction and improved track parameters (such as the Θ polar angle of tracks).

III.2.3 Time-of-Flight Detector

The time-of-flight system (ToF) of the CLEO II detector provides primary trigger for data recording and also used as an alternative tool for particle identification. The ToF measures the flight time of particles produced at the interaction point with a resolution of $\sim$ 140 ps. This time information combined with the momentum of the particle (measured by the drift chamber) gives a constraint on the particle mass and helps in the identification. Separation of different particles is illustrated on Fig. III.11.

The ToF system consists of 64 barrel and 2×28 endcap counters located immediately outside of the main drift chamber and fastened to the inside surface of the crystal calorimeter. The ToF covers 97% of the 4π solid angle. The active material of the counters is Bicron BC-408 plastic scintillator, which produces a flash of light when a charged particle passes through it. The induced light is detected by photo-multiplier tubes (PMT). At each end of the barrel scintillators a bent lucite light guide provides connection to the PMT outside the

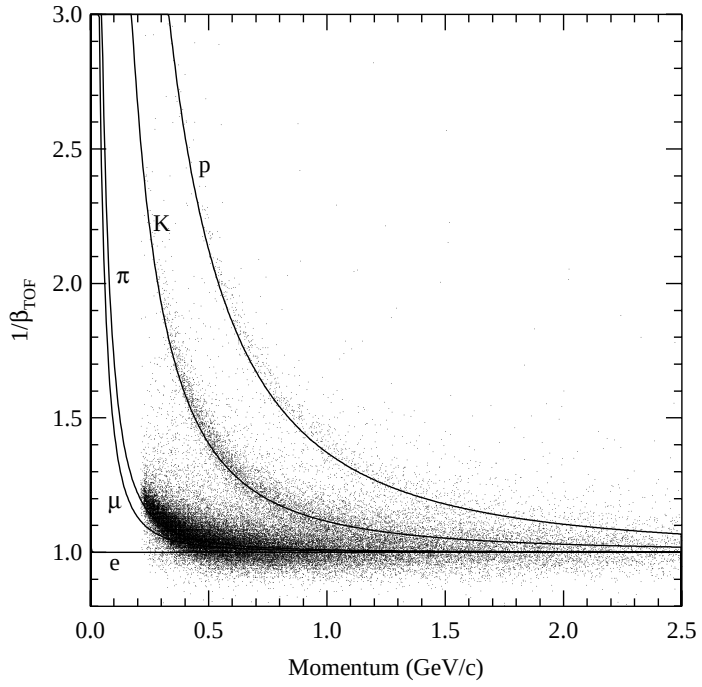

Figure III.11: Time of flight measurement of the particles' speed (β) versus the momentum.

magnetic field. Dimensions of a barrel counter is shown on Fig. III.12. The endcap counters are 4.8 cm thick trapezoidal sectors and each of them is connected directly (without light guide) to a single PMT, which is situated inside the magnetic field with the tube axis parallel to the field.

III.2.4 Electromagnetic Calorimeter

The electromagnetic crystal calorimeter (CC) consists of a barrel and two endcap sections containing 7800 thallium-doped Cesium Iodide (CsI) crystals and covering 95% of the solid angle. The size of each CsI block is 5 cm^2 by 30 cm. In the barrel region the blocks are arranged so that they point toward the interaction point. In order to reduce the material in front of the crystals, the whole calorimeter was placed inside the superconducting solenoid

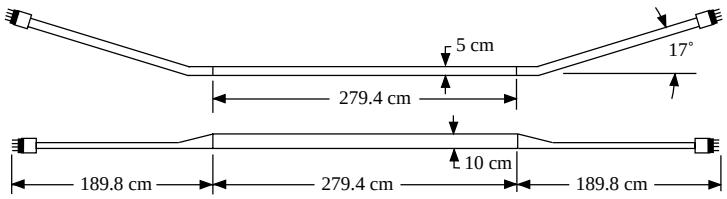

Figure III.12: Barrel time-of-flight counter.

magnet. The barrel region, which covers the polar angle range $45° - 135°$ has the smallest amount of material in front of it. Unfortunately, a larger amount of material (such as the drift chamber endplate and readout electronics) stands between the interaction region and each endcap thereby reducing their effectiveness compared to the barrel region.

Heavy charge particles entering the calorimeter lose some of their energy by ionizing and exciting the atoms of the crystal, which deexcite by emitting light. In contrast, high energy photons and electrons induce an electromagnetic cascade (shower) of secondary electrons and photons via e^+e^- pair production and bremsstrahlung. The energy of the secondary electrons eventually falls below the critical energy when they dissipate energy by ionization and excitation rather than generation of more shower particles. Four silicon photodiodes mounted on a lucite window on the rear face of each crystal convert the scintillation light into electrical signal. A clustering algorithm combines the signals from adjacent crystals in order to correctly reconstruct the total energy deposited by a particular shower. Photons are identified by those showers that are not associated with a charged track in the drift chamber. Typical photon energy resolution at 100 MeV (5 GeV) is 3.8% (1.5%) in the barrel and 5.0% (2.6%) in the endcap region. Angular resolution is 11 mrad (3 mrad) in the barrel and 19 mrad (9 mrad) in the endcap at energy of 100 MeV (5 GeV).

The crystal calorimeter is crucial to find and reconstruct particles that decay into photons. $\pi^0 \to \gamma\gamma$'s and $\eta^0 \to \gamma\gamma$'s are reconstructed with mass resolution $\sim 5 - 6$ MeV.

The information provided by the calorimeter together with the momentum measurements in the drift chamber is also used to distinguish electrons from other charged particles. Electrons, in contrast to heavy hadrons, usually lose all of their energy in the calorimeter. Therefore, the E/p ratio peaks at 1.0 for electrons while it is close to zero for other particles as it is demonstrated on Fig. III.13. This quantity combined with other information, such as the dE/dx measurement, the lateral shape of the shower produced by the particle as well as the distance between the projected track position and the shower location makes powerful electron identification possible.

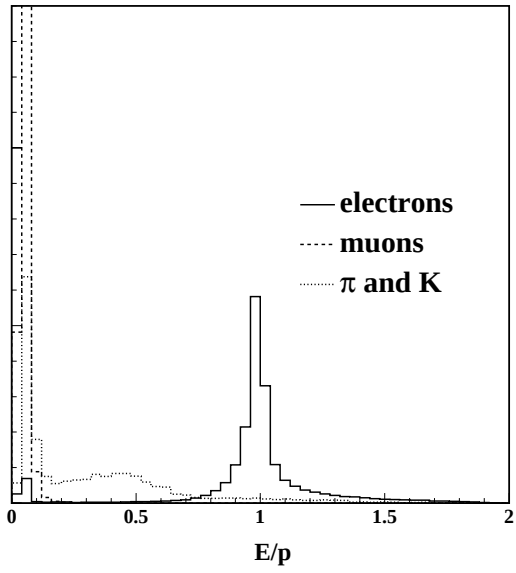

Figure III.13: The ratio of shower energy to momentum for different charged particle types.

III.2.5 Superconducting Magnet and Muon Detector

The CLEO II superconducting solenoid magnet provides a uniform 1.5 T magnetic field parallel to the beam axis. The magnet is installed outside the electromagnetic calorimeter and has a length of 3.5 m and inner diameter of 2.9 m. The two-layer superconducting coil is wound from Cu-NbTi embedded into 5×16 mm^2 pure Al jacket. The operating current is 3.3 kA. The coil is cooled by liquid helium using a self-regulating thermosiphon circulation flow system, which utilizes the buoyancy of lower density heated He to drive the liquid around the circuit.

The magnetic coil is surrounded by three layers of return yoke around the barrel region and pole pieces at each end for the purpose of magnetic flux return. Each layer of return yoke has a thickness of 36 cm and the gap between the layers is 9 cm. The iron of the return yoke and the pole pieces are part of the muon identification system.

Muons unlike other charged particles are highly penetrating and can travel large distances through matter without interaction. Therefore, the muon detectors are nested between the return yoke layers so that only the muons can reach these detectors and all other charged particles are stopped in the thick iron slabs. The three sets of barrel muon detectors outside of each return yoke layer is shielded by 36, 72 and 108 cm iron absorber[4], respectively, and cover the polar angle range $45^\circ - 135^\circ$. There is one set of muon chambers behind each pole piece which covers the angular range between $30^\circ - 48^\circ$ so that the whole muon detector system covers 85% of the total solid angle. There is a 2.5 cm thick iron outside the outermost m uon chambers for protection and radiation shielding.

The muon detectors are plastic streamer counters operating in a similar manner as the

[4]The mean free path between inelastic collisions (or nuclear interaction length) in iron is 16.8 cm. The total thickness of the iron absorbers is equivalent to $7.2 - 10$ nuclear interaction lengths depending on the direction of the track.

drift chambers in the center of the detector. The counters are 8.3 cm wide and 5 m long and are divided into 8 section as it is shown on Fig. III.14. The plastic housing is coated with graphite inside to provide a cathode for the eight 50 μm diameter silver-plated Cu-Be anode wires. The chambers are filled with 50%$-$ 50 % argon-ethane mixture and the anodes operate at 2.5 kV. The space resolution of one counter is around 2.4 cm.

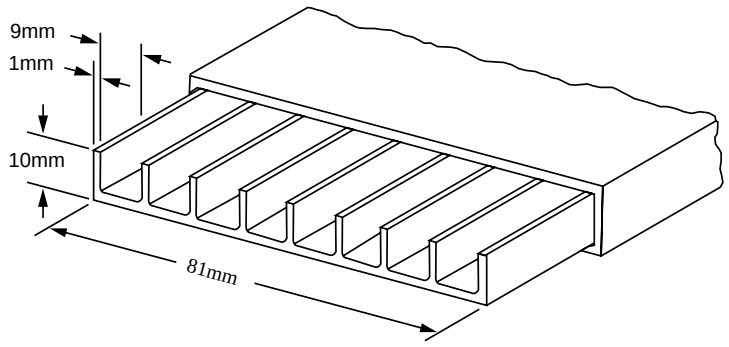

Figure III.14: Structure of a plastic streamer muon chamber.

Each iron gap and the exterior of the iron absorber is instrumented with a detector unit or super-layer composed of three layers of counters (see Fig. III.15) for increased efficiency. Each layer provides hit information in two orthogonal coordinates. The azimuth coordinate of a hit is obtained by the position of the anode, while the coordinate along the counter is determined by charge division read-out at both ends of the anode wires and the copper pickup strips on the exterior of the counters.

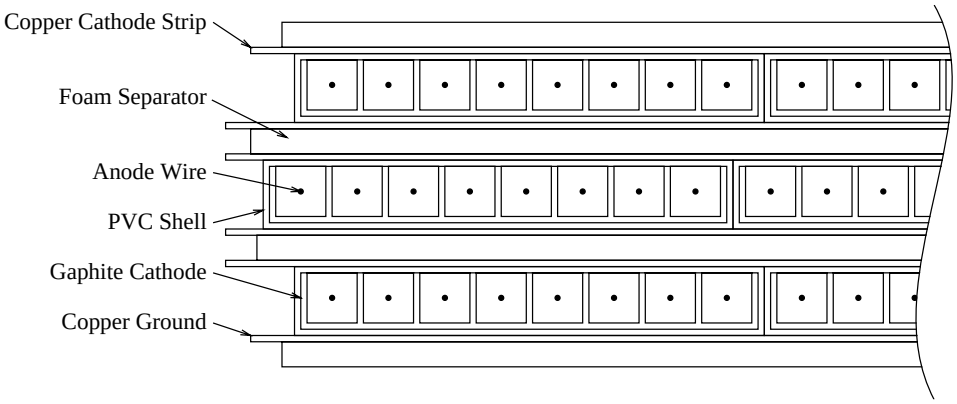

Figure III.15: Cross section of a muon detector super-layer.

III.2.6 CLEO Triggers and Data Acquisition System

Trigger System

Approximately 10 million e^+e^- beam collisions occur in every second. However, it is impossible to record all the data produced at every time a bunch crossing occurs because of two reasons. One reason is the limited storage capabilities; if an 'event' happens thousands of electronic channels can fire above threshold, which means several kB data each time. At the same time, it takes couple of ms to read out and write to disk or tape such amount of data, and the detector can not accept any new data until this procedure is finished resulting in some dead-time for the detector.

On the other hand, the vast majority of the events that occur are noise or uninterested background events and only a couple of them is interesting for us. Therefore, we have to filter out the unwanted events and find only those that are worth to record for future analysis. For this filtering purpose CLEO has developed a three-level trigger system, which is an optimal

combination of hardware and software decisions to recognize certain event characteristics in real time during data taking [56]. Earlier fast and simple hardware filters are supposed to eliminate much of the noise before higher level increasingly sophisticated and more time consuming filters further scrutinize the event. The flow chart of the CLEO trigger decisions is shown on Fig. III.16.

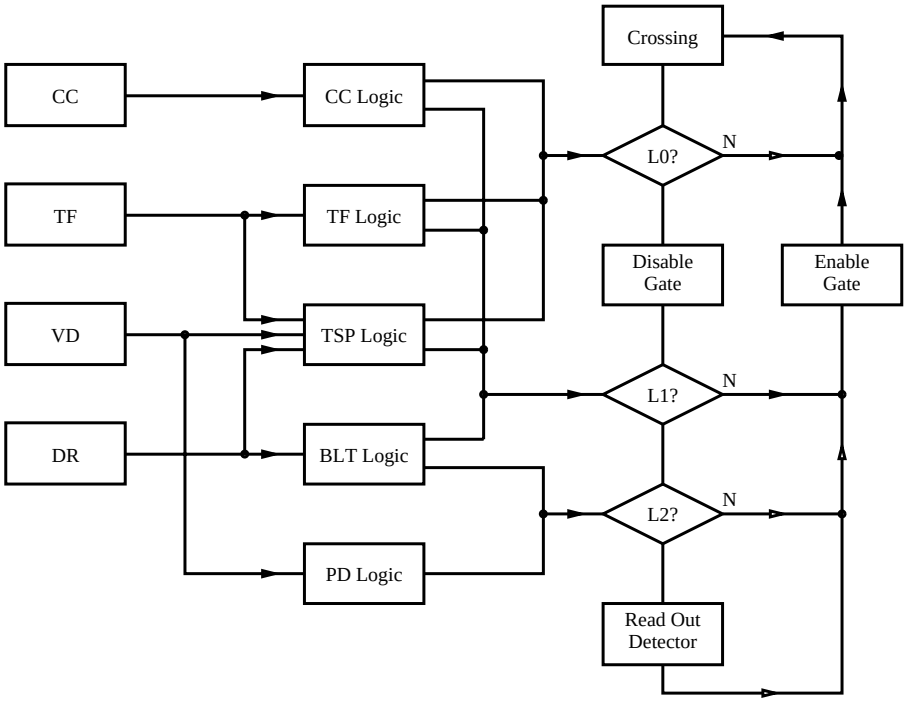

Figure III.16: Block diagram of the CLEO trigger system.

The subsequent levels of trigger are referred as Level0 (L0), Level1 (L1) and Level2 (L2).

L0 is a fast simple discrimination based on the trigger information coming from the time-of-flight scintillators (TF), the electromagnetic calorimeter (CC) and the vertex detector (VD). It is looking for events that might have tracks in them. After L0 the event rate falls down to about 20 kHz. If the L0 trigger requirement is satisfied the detector is frozen and preparation for the next trigger decision begins. It takes about 1 μs to initiate the L1 trigger, which implies a 2% dead time at the 20 kHz L0 rate. The L1 trigger uses crude track information coming from the central drift chamber (DR) in addition to the CC, TF and VD trigger signals. There are several L1 trigger combinations set by the experimenter. If none of these are satisfied the detector resumes data taking. If any of the L1 trigger criteria is met then the corresponding set of L2 criteria is examined in the next step. The L1 trigger reduces the event rate to 30-50 Hz. Initiating the L2 trigger, which uses only vertex detector and drift chamber information, requires $\sim$ 50 μs per event resulting in a dead time $< 0.25\%$. If no proper L2 criteria are met the system is reset and the detector is released to accept a new event, otherwise the data is read out from the detector elements. The total read out takes approximately 10 ms which means $5 - 10\%$ dead time at the L2 trigger rate of $5 - 10$ Hz.

Data Acquisition System

Once an event passed the L2 trigger the signals from the detector electronics must be read out. Analog signals are shaped, amplified and digitized. A final software test of data quality (sometimes called Level3 trigger), which filters out most of the events caused by a beam particle hitting the beam-pipe (beam-wall events) making up typically 25% of the total events passing the L2 trigger is initiated. All data from the sub-detector elements are put into one data record by the event builder, which makes sure that the data in one record comes from the same event trigger. The event builder also formats the data into sequential

(ZEBRA) records and writes them to an online disk. Finally, the data on the disk is copied to tape.

Besides the data flow control, the detector elements should also be monitored and controlled. CESR is not running continuously since the beam intensity is deteriorating with time due to beam-gas collisions and other reasons. After a certain time, usually $45 - 60$ minutes, it is more efficient to fill up and reshape the beams. This procedure, which takes approximately 10 minutes, naturally divides the data collection into separate runs. Data taking must be stopped at the end of each fill and restarted when CESR is topped off and e^+e^- collisions start again. During the injection period, the high voltage supply of the tracking detectors must be turned off. All of these hardware functions and settings are controlled by the data acquisition system (DAQ) which is shown on Fig. III.17.

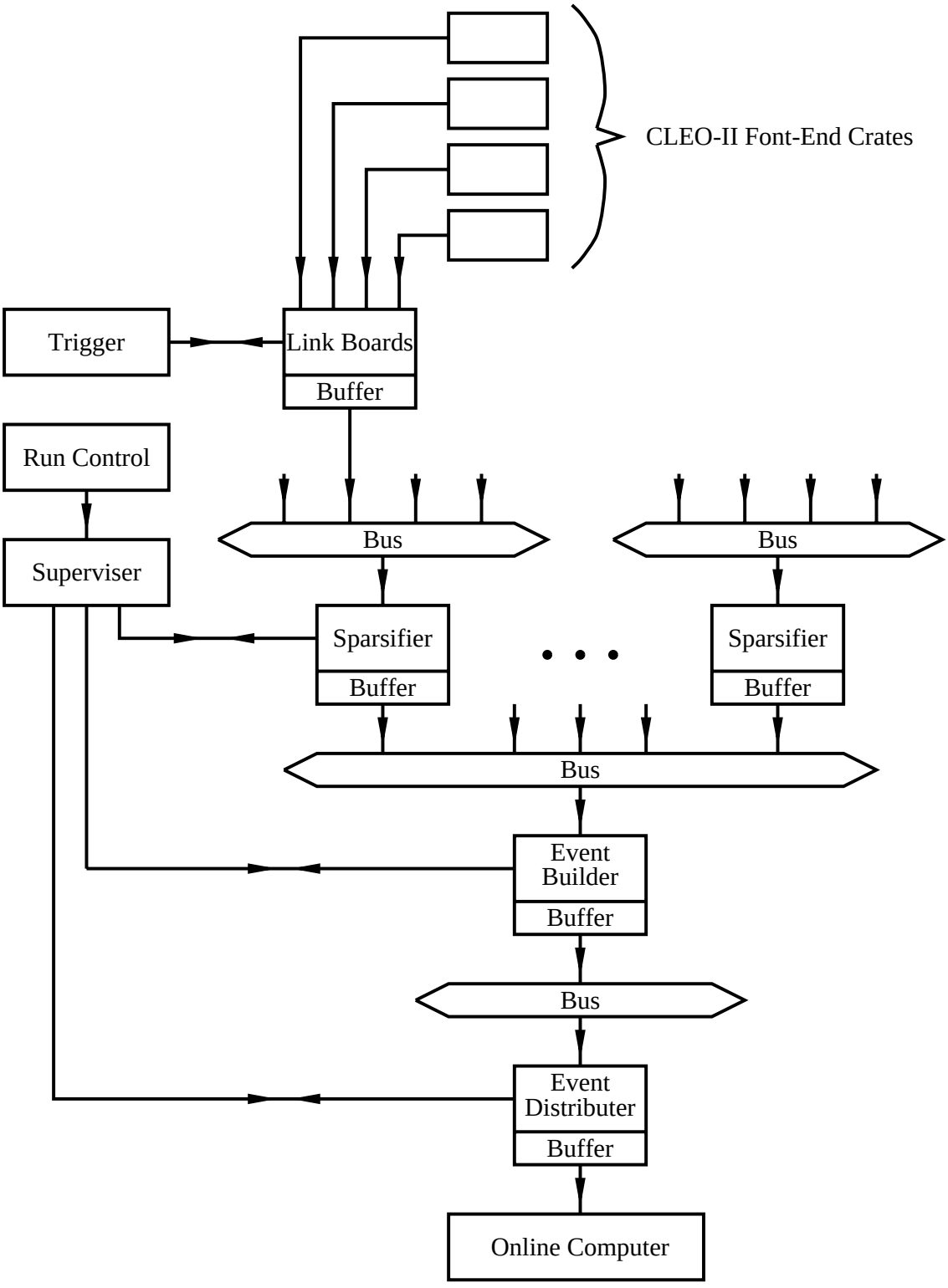

Figure III.17: Block diagram of the CLEO data acquisition system.

CHAPTER IV

DATA SAMPLE

IV.1 Upsilon resonances

The basic physics process taking place in the e^+e^- collision is the annihilation into a virtual photon, which then produces a fermion-antifermion pair. We can get another e^+e^- pair (Bhabha scattering), $\mu^+\mu^-$, $\tau^+\tau^-$ or other QED events, such as $\gamma\gamma$ or $e^+e^-\gamma$. An other common process is the production of a $q\bar{q}$ quark-pair of five different flavors (q=u, d, c, s, b) that are accessible at the energy of CLEO[1]. The most interesting for us is the b-quark which has a mass of around 5 GeV.

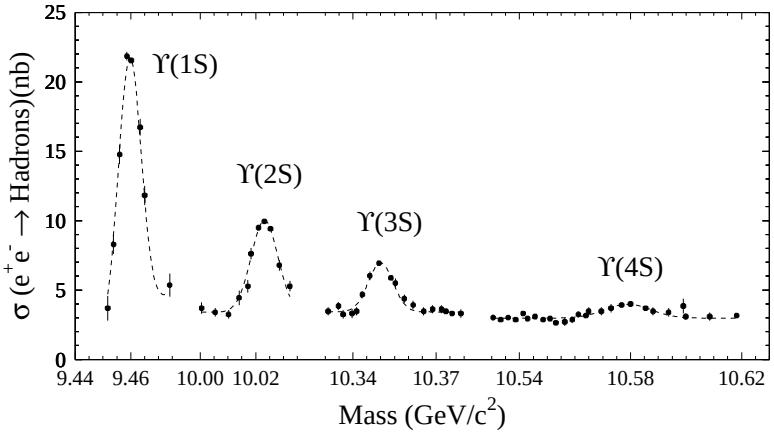

Figure IV.1: Hadron cross section in e^+e^- annihilation as the function of the center of mass energy of the collision in the vicinity of the Upsilon (Υ) resonances.

The b-quark is produced in resonances, the Upsilon (Υ) resonances, which are the massive

[1]The sixth quark, t, is too heavy ($m \approx 173$ GeV) to be produced at the center of mass energy of the collision ($\sqrt{s} \approx 10.5$ GeV)

bound states of a b and an anti-b ($\bar{b}$) quark (bottomium). The first four resonances are depicted on Fig. IV.1, which shows the production cross section of multitrack final states in the energy range $9.44 - 10.62$ GeV. The Upsilon resonances sit on the top of a continuum background, which includes $\tau^+\tau^-$ and $q\bar{q}$ production of the light quarks $q = u, d, c, s$.

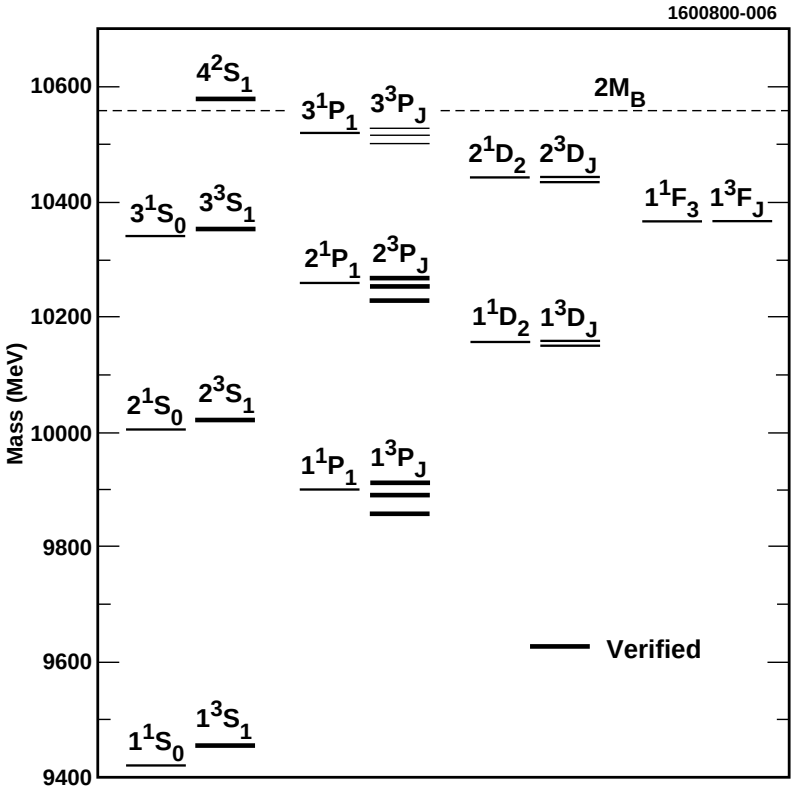

Figure IV.2: Spectrum of the bottomium ($b\bar{b}$) system.

The spectrum of the Upsilon resonances along with other bottomium states is shown on Fig. IV.2. The different $b\bar{b}$ states are distinguished by their quantum numbers, $N^{2S+1}L_J$,

where N is the radial quantum number, S is the spin quantum number, L and J are the quantum numbers associated with the relative orbital angular momentum between the quarks[2] and the total angular momentum of the system $\vec{J} = \vec{L} + \vec{S}$, respectively.

The Upsilon (Υ) resonances are the $^3S_1$ states, in which the quark-pair has zero orbital angular momentum (S-state) and parallel spin ($J = S = 1$). These states are shortly referred as $\Upsilon(1S)$, $\Upsilon(2S)$ etc. The first three Upsilon resonances are relatively long-lived and hence they are narrow resonances compared to the $\Upsilon(4S)$,[3] which lies just above the energy threshold of B and $\bar{B}$ meson production $\sqrt{s} = 2M_B = 10.56$ GeV. This new decay channel

$$\Upsilon(4S) \to B\bar{B},$$

available for the forth resonance makes it short lived and wider than the other three resonances.

IV.2 On-resonance and off-resonance data

Most of the time CESR runs at the energy of the $\Upsilon(4S)$ resonance at $\sqrt{s} = 10.58$ GeV. At this energy the $e^+e^- \to \Upsilon(4S) \to B\bar{B}$ cross section is approximately 1 nb while the continuum production cross section is about $3.5 - 4$ nb (see Fig. IV.1). Therefore, only $\sim 20\%$ of the on-resonance data sample contains $B\bar{B}$ events and the rest is background. In order to study the non-$B\bar{B}$ events in this sample, CERS runs 60 MeV below the $\Upsilon(4S)$ resonance roughly one third of the time to collect an off-resonance data sample, which does not contain any $B\bar{B}$ events.

[2]The notation is the same as in atomic spectroscopy, that is S, P, D, and F denote states with $L = 0, 1, 2, 3\hbar$ orbital angular momentum.

[3]The difference in the width of the resonances are not apparent on Fig. IV.1 because the energy spread of the beam makes the narrow resonances wider.

The data sample is divided into datasets, each of which covers a continuous period of running. The divisions between the datasets are marked by any change in the detector geometry. In this analysis we used the datasets from 4s2 to 4sT given in Table IV.1. One third of the data ending with the 4sG dataset was collected with the CLEO II configuration of the detector. The data collected by the upgraded CLEO II.5 detector begins with the 4sH dataset.

The whole data sample represents an integrated luminosity of 13.8 fb^{-1}. Out of this, 9.2 fb^{-1} was collected on the $\Upsilon(4S)$ resonance and 4.6 fb^{-1} was taken off resonance. We designated an event as on-resonance (off-resonance) if its beam energy is $E_{\rm beam} > 5.285$ GeV ($E_{\rm beam} < 5.280$ GeV). The on-resonance sample contains approximately 9.7 ± 0.2 million $B\bar{B}$ pairs. The uncertainty of this number is related to the variation in the determined cross section from dataset to dataset and the error in the trigger efficiency.

When we are doing B physics we are interested only the $B\bar{B}$ events in the on-resonance data sample. However, we are not able to separate these events from the continuum background. If we hunt for a particular B-meson decay mode we have to chose characteristic variables that show significant difference between the signal and the background events. Of course, if we want to maintain a reasonable signal selection efficiency, especially in case of a very rare decay, it is impossible that the set of selection criteria filters out every background event. Using the off-resonance data sample, which contains only continuum background events, one can model the non-$B\bar{B}$ events in the on-resonance sample and their contribution can be statistically subtracted.

In order to do this continuum subtraction we have to normalize the off-resonance data sample to the statistics of the on-resonance sample. As we know, the rate of a particular process, such as $q\bar{q}$ or tau-pair production, is equal to the product of the luminosity and

Table IV.1: Summary of the CLEO II/II.5 datasets.

Data Set	Dates	Integrated Luminosity (pb^{-1})
4s2	11 NOV, 1990 − 04 JUN, 1991	672.0
4s3	18 SEP, 1991 − 17 FEB, 1992	680.2
4s4	10 APR, 1992 − 26 MAY, 1992	317.5
4s5	09 JUL, 1992 − 05 OCT, 1992	342.7
4s6	03 NOV, 1992 − 19 JAN, 1993	316.5
4s7	16 MAR, 1993 − 06 JUL, 1993	461.3
4s8	01 AUG, 1993 − 27 SEP, 1993	274.4
4s9	22 NOV, 1993 − 10 JAN, 1994	340.1
4sA	20 JAN, 1994 − 28 FEB, 1994	190.8
4sB	19 MAR, 1994 − 16 MAY, 1994	140.9
4sC	16 JUN, 1994 − 15 AUG, 1994	141.5
4sD	15 SEP, 1994 − 09 OCT, 1994	98.0
4sE	09 OCT, 1994 − 01 NOV, 1994	128.8
4sF	03 NOV, 1994 − 28 NOV, 1994	145.9
4sG	19 JAN, 1995 − 09 APR, 1995	456.6
4sH	16 NOV, 1995 − 11 MAR, 1996	521.0
4sJ	03 APR, 1996 − 08 JUL, 1996	677.0
4sK	19 AUG, 1996 − 28 OCT, 1996	595.0
4sL	17 NOV, 1996 − 10 MAR, 1997	1080.6
4sM	05 APR, 1997 − 17 JUN, 1997	531.8
4sN	19 JUN, 1997 − 17 AUG, 1997	714.3
4sP	15 OCT, 1997 − 09 FEB, 1998	1103.6
4sQ	27 FEB, 1998 − 21 APR, 1998	559.9
4sR	21 APR, 1998 − 08 JUN, 1998	499.1
4sS	27 JUN, 1998 − 05 OCT, 1998	1214.3
4sT	10 NOV, 1998 − 15 FEB, 1999	1583.3
Total		13787

the cross section of that process $R = \mathcal{L}\sigma$. The cross section of these processes scales as the inverse square of the center of mass energy of the e^+e^- collision, $\sqrt{s} = 2E_{\rm beam}$,

$$\sigma \propto \frac{1}{s} \propto \frac{1}{E^2_{\rm beam}}. \tag{IV.1}$$

Hence, the normalization factor between the on-resonance and off-resonance sample can be calculated as

$$R = \frac{\sum_{i\in {\rm on-res}} \mathcal{L}_i/E_i^2}{\sum_{i\in {\rm off-res}} \mathcal{L}_i/E_i^2}, \tag{IV.2}$$

where $\mathcal{L}_i$ and E_i are the integrated luminosity and average beam energy of the $i^{\rm th}$ data-run, and the sum in the numerator (denominator) runs over the on-resonance (off-resonance) data-runs with $E_i > 5.285$ GeV ($E_i < 5.280$ GeV). We obtained $R = 1.998$ for the entire data sample, which is consistent to 2.0 within the 2% error of this quantity and therefore we use d the later number in our analysis. The 2% error is due to the systematic uncertainty in the luminosit y of the data samples.

IV.3 Monte Carlo simulation of events

Simulated events play a very important role in the analysis. First of all, this is the only way to model the signal events and to study the signal shapes, such as the momentum and angular distributions of particles. By comparing these shapes to those expected in the background we chose the variables that are most effective to distinguish the signal from the background. In order to minimize the effect of statistical fluctuations and human bias, it is best to minimize exposure to the measured data. Therefore, beside the simulated signal events, we also use simulated background events (with $3-5$ times as much statistics as the measured background) to find the best selection criteria that enhance the signal in the greatest extent relative to the background. Finally, the signal simulation is used to determine

signal selection efficiency.

CLEO uses an elaborate Monte Carlo scheme to generate simulated events that looks just like real data in format. This simulation reproduces the interactions after the e^+e^- collision, the propagation of particles through the detector and their interaction with its material, and the signal processing. These three main steps are described below.

- Event generator: The program called QQ simulates particle production and their decay down to stable particles. The different decay chains are generated randomly but in the correct proportion based on the information provided by the Particle Data Group [53]. However, the user is allowed to modify the decay chains, branching fractions or particle properties to simulate $B\bar{B}$, $q\bar{q}$ or any signal event needed.

- Detector simulation: CLEOG, a package based on GEANT [57], simulates the detector response to the particles generated by QQ. It maintains a database of all the material in the CLEO detector and models how a particle will react to the material. The particle propagates through the material in steps, and each step a random number is thrown to decide how much energy the particle looses and how its direction changes. CLEOG also simulates the response of the detector electronics.

- Event Reconstruction: The detector hits from CLEOG are passed to the standard event reconstruction software, called PASS2, that is used with the real data. The only essential deference compared to the treatment of the data is that detector noise and beam related background are superimposed on the CLEOG output events to make them look more realistic. The noise events are random trigger events taken by CLEO with no beams in the machine, while the beam related background is physics hits stripped from events, such as $e^+e^- \to \mu^+\mu^-$.

The Monte Carlo generated events are recorded in the same format as the data events but they contain extra information that allows us to match reconstructed particles to a generated particle. This information can be used to study if reconstructed signal modes are correct but they can not be used when we determine the signal selection efficiency. The simulated events must be processed in the same way as the data in order to avoid any bias. Although, CLEO's Monte Carlo simulation does a remarkably good job of simulating data, one has to cross-check the MC results with data and correct them if necessary or incorporate the uncertainties into the systematic error appropriately.

A tremendous amount of generic Monte Carlo events that simulate $B\bar{B}$, $q\bar{q}$ and tau-pair events were generated by the combined effort of the collaboration. This data is stored primarily on tapes and copied to staging disks with a turnaround time of $3-4$ weeks, where they are available via a computing farm. However, if one is doing an analysis s/he has to generate signal and specific background events needed that particular analysis.

In order to study our signal shapes and efficiency, we generated 90 thousand events to simulate each of the decay modes, $B^{\pm} \rightarrow \pi^{\pm} f$, $B^{\pm} \rightarrow K^{\pm} f$ and $B^0 \rightarrow K^0_S f$. In each generated events, one of the B mesons was required to decay into the light meson plus the familon, while the other was allowed to decay generically. The familon was defined as a neutral, massless, spin-zero stable particle (similar to a neutrino except for the spin). In case of the charged B decays, half of the signal Monte Carlo forced the B^+ to decay into familon mode, and the other half forced the B^- to decay. 1/3 (2/3) of the events were generated by using the parameters corresponding to the CLEO II (II.5) version of the detector and were properly distributed over the various running conditions so that the simulated sample correctly reflects the real data sample. In addition, we also generated samples to simulate specific rare decay modes of the B mesons, which are not included in the generic $B\bar{B}$ sample,

to further study their contribution to the background.

CHAPTER V

SEARCH FOR $B \to hX^0$ DECAYS

We saw in Chapter II that the off-diagonal coupling of the familon to the flavor current can lead to the decay of the bottom quark to other down-type quarks: $b \to q_d f$ $(q_d = d, s)$. This decay mechanism can induce the decay of the B meson to a lighter pseudoscalar (spin-0 and odd-parity) meson and the familon through *vector-like coupling*. The lowest order Feynmann diagram corresponding to this decay is depicted on Fig. V.1.

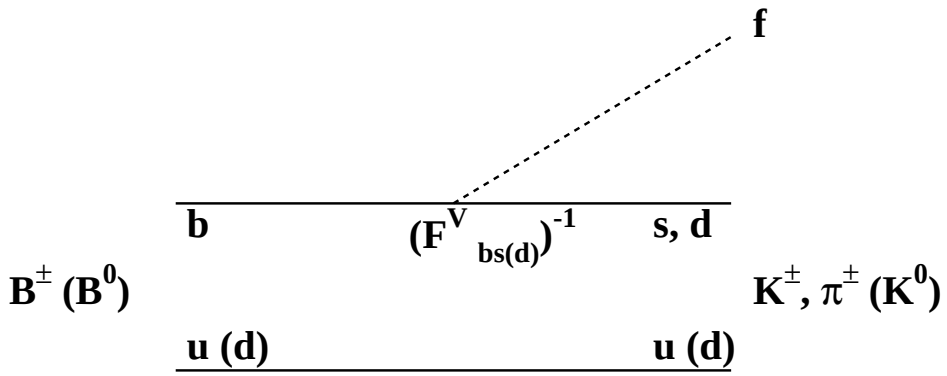

Figure V.1: Feynmann graph for $B \to (\pi, K) f$ decay.

Since the familon interacts very weakly with ordinary matter its detection is hopeless with our detector system. Only the light meson partner of the familon is observable accompanied by a large amount of missing energy associated with the elusive familon. In this chapter, we describe the search for two-body B meson decays into a final state containing a light pseudoscalar meson h and a massless neutral weakly-interacting particle X^0, such as the

familon.

We restricted our analysis for the following decay modes:

- $B^{\pm} \to \pi^{\pm} X^0$,
- $B^{\pm} \to K^{\pm} X^0$, and
- $B^0 \to K^0_S X^0$.

The most relevant properties of the mesons involved in this analysis are summarized in Table V.1 based on Ref. [53]. The charged π and K mesons has a long lifetime and they are easily detectable with the drift chamber. On the other hand, the K^0 meson is neutral and has two manifestations corresponding to the even (K^0_S) and odd (K^0_L) CP eigenstates[1]. As it can be seen from the Table, the K^0_L has a much longer lifetime than the K^0_S and therefore it travels further and most of the time it decays outside the detector. In contrast, the K^0_S can be easily identified through its decay to $\pi^+\pi^-$ (with a relative branching fraction of around 69%), which occurs within a few cm from the primary interaction point. Since CLEO's vertex detector is suitable for finding this secondary vertex with a good efficiency we searched for final states containing only the K^0_S meson decaying to $\pi^+\pi^-$.

V.1 Analysis Strategy

We are looking for events when one of the B mesons produced in the $e^+e^- \to \Upsilon(4S) \to B\bar{B}$ process decays to the desired modes mentioned in the previous section. In such events, one observes the light meson ($h = \pi^{\pm}, K^{\pm}, K^0_S$) plus a number of other particles coming from the decay of the second B.

[1] At least, neglecting a small CP violation effect.

Table V.1: Properties of the mesons. I is the isospin quantum number, J^P is the intrinsic spin and parity quantum number, M is the mass, τ is the mean lifetime and c is the speed of light. The dual entries in the K^0's line correspond to K^0_S / K^0_L.

Meson ($q\bar{q}$)	I	J^P	M [MeV/c^2]	τ [ps]	$c\tau$ [cm]
B^+ ($u\bar{b}$), B^- ($b\bar{u}$)	1/2	0^-	5279	1.653	0.0496
B^0 ($d\bar{b}$), $\bar{B}^0$ ($d\bar{b}$)	1/2	0^-	5279	1.548	0.0464
K^+ ($u\bar{s}$), K^- ($s\bar{u}$)	1/2	0^-	494	12386	371
K^0 ($d\bar{s}$), $\bar{K}^0$ ($s\bar{d}$)	1/2	0^-	498	89.35 / 51700	2.68 / 1551
π^+ ($u\bar{d}$), π^- ($d\bar{u}$)	1	0^-	140	26033	780

Due to the two-body decay structure, the daughter meson from the $B \to hX^0$ decay is produced with a well defined momentum in the center of mass frame of the decaying B (see section II.5), namely

$$p_h^{c.m.} = \frac{1}{2} M_B \left(1 - \frac{m_h^2}{M_B^2}\right) \approx \frac{M_B}{2} = 2.64 \text{ GeV}/c, \tag{V.1}$$

where M_B and m_h are the mass of the B and the light meson, respectively. However, in the lab frame its momentum is spread between $2.48 \lesssim p_h^{lab} \lesssim 2.80$ GeV/c due to Doppler broadening:

$$p_P^{lab} \approx p_P^{c.m.} \left(1 + \frac{p_B}{M_B} \cos\theta_{P-B}\right) \approx p_P^{c.m.} \left(1 + 0.06 \cos\theta_{P-B}\right) \tag{V.2}$$

($p_B \approx 0.32$ GeV/c is the momentum of the B meson and θ_{P-B} is the angle between the directions of the B and the daughter meson in the lab frame). The momentum distribution of reconstructed pions in simulated signal $B^- \to \pi^- f$ events is illustrated on the upper plot of Fig. V.2.

All other particles and photons detected in a signal event must come from the decay of the second B meson. One possible strategy might be to fully reconstruct the second B using some of its hadronic decay modes. Although, this method would reduce the background

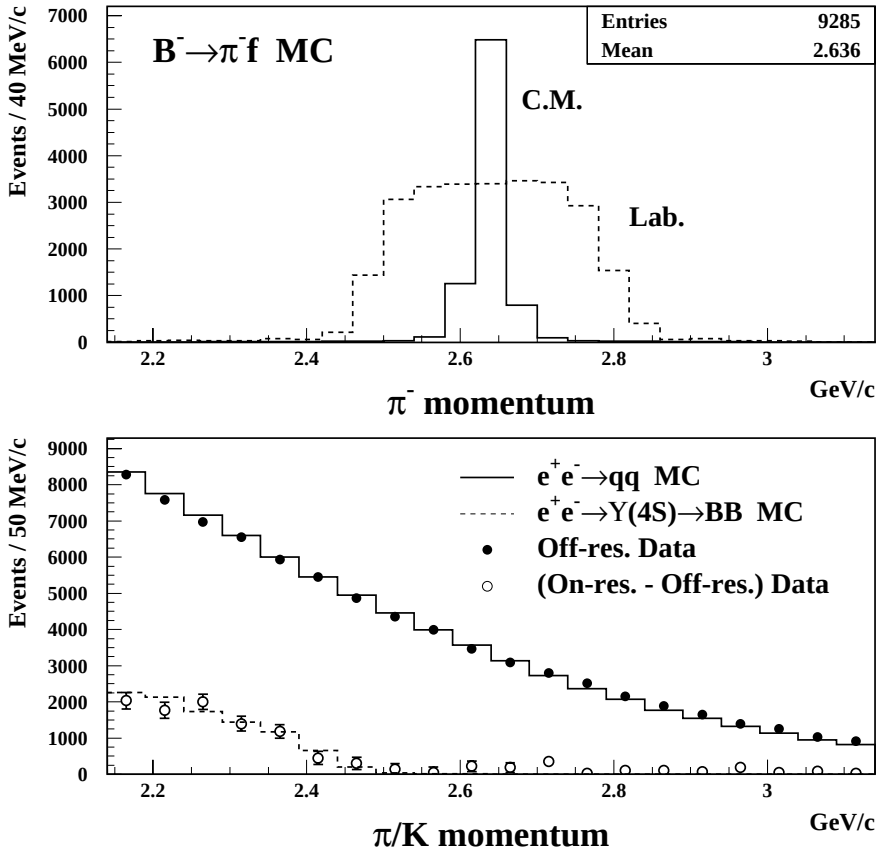

Figure V.2: Momentum distribution of the daughter meson in signal and background. Top: momentum distribution of π^- in the B meson's rest frame (solid) and the lab frame (dashed) for Monte-Carlo simulated $B \to \pi^- f$ sample. Bottom: momentum distribution of the meson candidate in Monte-Carlo simulated background (histograms) and data (dots).

level significantly, it would also seriously limit the sensitivity of the analysis because of the small branching fraction of the appropriate decay modes. Instead, we applied kinematic constraints dictated by energy and momentum conservation to select candidate events. This method relies on the good hermeticity of the CLEO II detector, that is on the fact that most of the particles, which were produced in the e^+e^- collision are detected.

It can be seen on the lower plot of Fig. V.2 that the dominant $b \to c$ decays, which

are simulated in the $B\bar{B}$ Monte-Carlo sample, do not contribute to the momentum range accessible for the light meson between $2.48 - 2.80$ GeV/c. On the other hand, rare $b \to u$ and $b \to s$ processes can produce high momentum π or K mesons, but typically with other energetic particles which will spoil the reconstruction of the other B decay in the event. Decays such as $B^+ \to \pi^+ K_L^0$, $B^+ \to K^+ \nu\bar{\nu}$ and $B^- \to \tau^-(h^-\nu)\bar{\nu}$ will contribute at high momentum but are highly suppressed.

Therefore, the dominant background comes from continuum $e^+e^- \to q\bar{q}$ ($q = u, d, c, s$) events. The contribution of this background can eventually be statistically subtracted using the off-resonance data sample. However, since this background is large enough to overwhelm any signal, it is important to eliminate as much of that as possible and enhance the signal relative to the background. For this purpose, we exploited the difference in the decay topology of $B\bar{B}$ and continuum $q\bar{q}$ events.

V.2 Event Selection

In this section we describe the detailed methods and selection criteria, which we used to choose candidate events out of the tens of millions of events collected with the CLEO II detector.

V.2.1 Particle selection

We accepted events with at least four charged tracks. This criteria eliminates a large portion of the $e^+e^- \to \ell^+\ell^-$ ($\ell = e, \mu, \tau$) events, which makes up approximately 1/3 of the background, and leaves essentially hadronic events only.

The most important signature of the signal events we are hunting for is the presence of a high momentum charged π, K or a K_S^0 decaying subsequently into a $\pi^+\pi^-$ pair. We have to

make sure that the track selected as the daughter meson candidate is well reconstructed and not a spurious or poorly measured track. For this purpose, we essentially used the standard track quality criteria, which were developed by the CLEO collaboration in order to make rare B decay analysis effective [58].

- To avoid that our signal track is a 'ghost' track assembled from unrelated or missed hits in the drift chamber we selected charged particles from the list of well-reconstructed tracks and required to have hits in more than 30% of the tracking layers through which it passes and that the RMS residual for all the hits is between 20 and 600 μm.

- We chose tracks originating near the e^+e^- primary interaction point based on the impact parameter in both $r-\phi$ and $r-z$ plane: we required z-distance ≤ 25 mm and radial distance ≤ 3 mm between the collision point and the point of the track which is closest to the beam axis.

- We rejected electrons as a candidate track based on the log-likelihood (R2ELEC) which combines the specific energy loss (dE/dx) along the track in the drift chamber, the ratio of the associated shower energy deposited in the CsI calorimeter to the track momentum (E/p) and several shower shape variables:

$$R2ELEC = \sum_{variables} \ln\left(\frac{P_e}{P_{not\ e}}\right), \tag{V.3}$$

where P_e ($P_{not\ e}$) is the probability of that the track is (not) an electron. The distribution of this variable for electrons and π, K mesons is shown on Fig. V.3. We required $R2ELEC < 0$ for a candidate track. E/p is the most powerful variable to distinguish electrons from other particles. It is close to 1 for electrons while it is < 1 for hadrons and muons (see Fig. III.13).

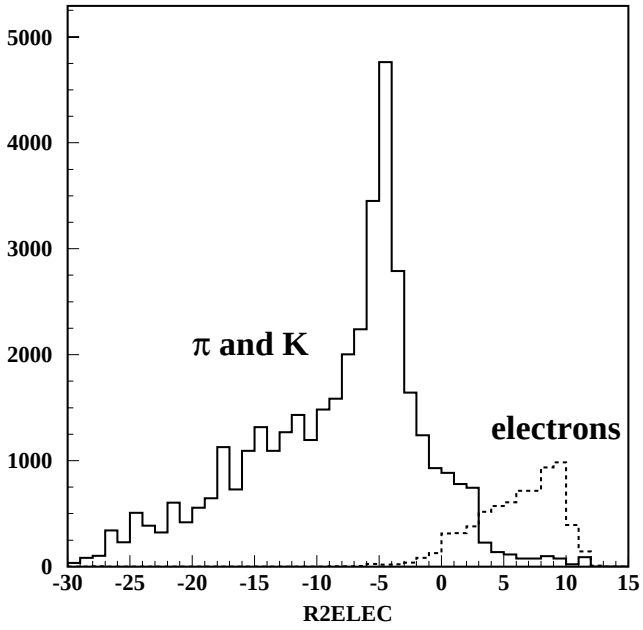

Figure V.3: Electron identification.

Muons were rejected based on the penetration depth in the flux return iron around the detector. We required that to be less than three nuclear interaction lengths.

- One way to distinguish between charged pions and kaons with the CLEO II detector is the specific ionization energy loss (dE/dx) measured in the main drift chamber. This quantity is shown as a function of the particle momentum on Fig. III.9 for different particle types. Although, the distinguishing power between π's and K's is good below 0.7 GeV/c it is less effective above 1.0 GeV/c as it is demonstrated on Fig. V.4. This two plots show the distribution of the variable which measures how many sigma away the truncated mean of the dE/dx distribution of a track is from the expected mean of

pions (left plot) and kaons (right plot):

$$S = \frac{(dE/dx)_{\text{measured}} - (dE/dx)_{\text{expected}}}{\sigma}. \tag{V.4}$$

Since the daughter meson is expected in the momentum range between $2.48 - 2.80$ GeV/c, where the separation between the pions and kaons is practically impossible, we just combined the two charged decay modes by requiring the charged track to be consistent with either the pion or the kaon hypothesis within 2.5 standard deviations (σ).

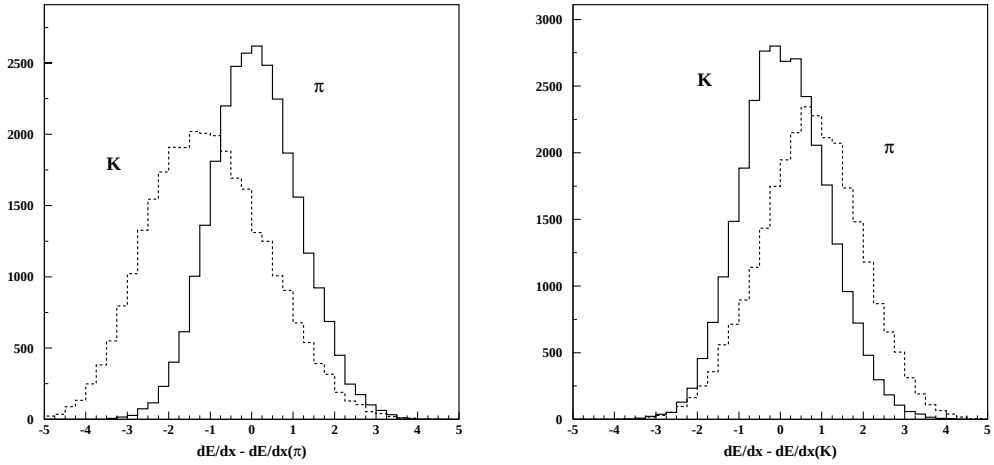

Figure V.4: Specific ionization energy loss with respect to the pion (left) and kaon (right) expectation for tagged π and K tracks with $p_{k/\pi} > 1$ GeV/c in Monte-Carlo simulated samples. The dE/dx difference is measured in σ units.

- We accepted candidate tracks with a polar angle between 26° and 154° with respect to the beam axis ($|\cos\Theta| < 0.9$). This criterion discards tracks near the edge of the drift chamber.

- K^0_S candidates were reconstructed using a pair of π^+ and π^- tracks originating from

a secondary vertex with a clear displacement from the primary interaction point. The invariant $\pi\pi$ mass was required to be within 10 MeV/c^2 of the known K^0_S mass. In addition, the reconstructed K^0_S candidate had to point back to the primary vertex and the number of hits between the primary vertex and the secondary vertex had to be minimal.

- We selected tracks with momentum between 2.1 and 3.1 GeV/c. Tighter criterion on the momentum was determined by a precise optimization procedure described later.

V.2.2 Kinematic requirements for the rest of the event

In our signal events all other particles beside the energetic light meson coming from the $B \to hX^0$ decay must be consistent with the decay of the other B meson. Hence, for an ideal signal event in which all the decay products are observed and perfectly measured

$$\begin{aligned} &E_B = E_{\rm rest}, \\ &\mathbf{p}_B = \mathbf{p}_{\rm rest} \qquad \left(\text{i.e.} \;\; M_B = \sqrt{E_B^2 - \mid \mathbf{p}_{\rm rest} \mid^2}\right), \end{aligned} \tag{V.5}$$

where E_B and M_B are the energy and invariant mass of the B meson, and $(E_{\rm rest}, \mathbf{p}_{\rm rest})$ is the 4-momentum of all detected particles except the light meson (h),

$$E_{\rm rest} = \sum_{i \neq h} E_i \qquad\qquad \mathbf{p}_{\rm rest} = \sum_{i \neq h} \mathbf{p}_i. \tag{V.6}$$

We calculated $E_{\rm rest}$ and $\mathbf{p}_{\rm rest}$ using all well-reconstructed charged tracks as well as the neutral showers which were not matched to a good track (to avoid double counting). Tracks had to satisfy the same track-quality criteria as the signal meson (see previous section) except that they were not required to point back to the primary interaction point. Thus, tracks produced at secondary vertices, such as those from $K^0_S \to \pi^+\pi^-$, $\Lambda^0 \to p^+\pi^-$, and $\gamma \to e^+e^-$

conversion, were counted as well. Since the pion is the most abundant particle occurring in hadronic events we assigned the π mass to all tracks when determining the momentum and energy of the tracks from the kinematic fit. Tracks with momentum above 5.3 GeV/c were discarded. Good showers with energy between 50 MeV and 5.0 GeV were counted if they had a polar angle between 26° and 154° with respect to the beam axis ($|\cos\Theta| < 0.9$). We rejected showers produced in earlier beam crossings.

Since CESR is a symmetric collider the energy of each B meson produced in the process $e^+e^- \to \Upsilon(4S) \to B\bar{B}$ must be equal to the energy of the e^- (e^+) beam. Therefore, we can substitute $E_B = E_{\rm beam}$ in the above expressions to define the beam-constrained B mass and energy difference as our kinematic observables:

$$\begin{aligned} M &= \sqrt{E^2_{\rm beam} - |\,\mathbf{p}_{\rm rest}\,|^2}, \\ \Delta E &= E_{\rm rest} - E_{\rm beam}. \end{aligned} \tag{V.7}$$

For an ideal signal event ΔE must be zero and M must be the known B meson mass 5.28 GeV/c^2.

Despite the fact that the CLEO detector covers almost the total 4π solid angle and has a very good efficiency, not all particles are measured. Charged particles can escape from detection through the beam pipe or interaction with the detector material can distort the measurement or make it impossible. Since the detection efficiency is not 100% and it is worse for low momentum tracks we can miss a particle even if it is within the acceptance of the detector. However, the main source of information loss is related to neutral particles, which are extremely difficult (e.g. neutrons and K^0_L) or entirely impossible to measure (such as neutrinos produced in semileptonic decays of quarks). Therefore, the distribution of M and ΔE is altered with respect to the expectation.

Distribution of M and ΔE for Monte-Carlo generated samples are shown on Fig. V.5.

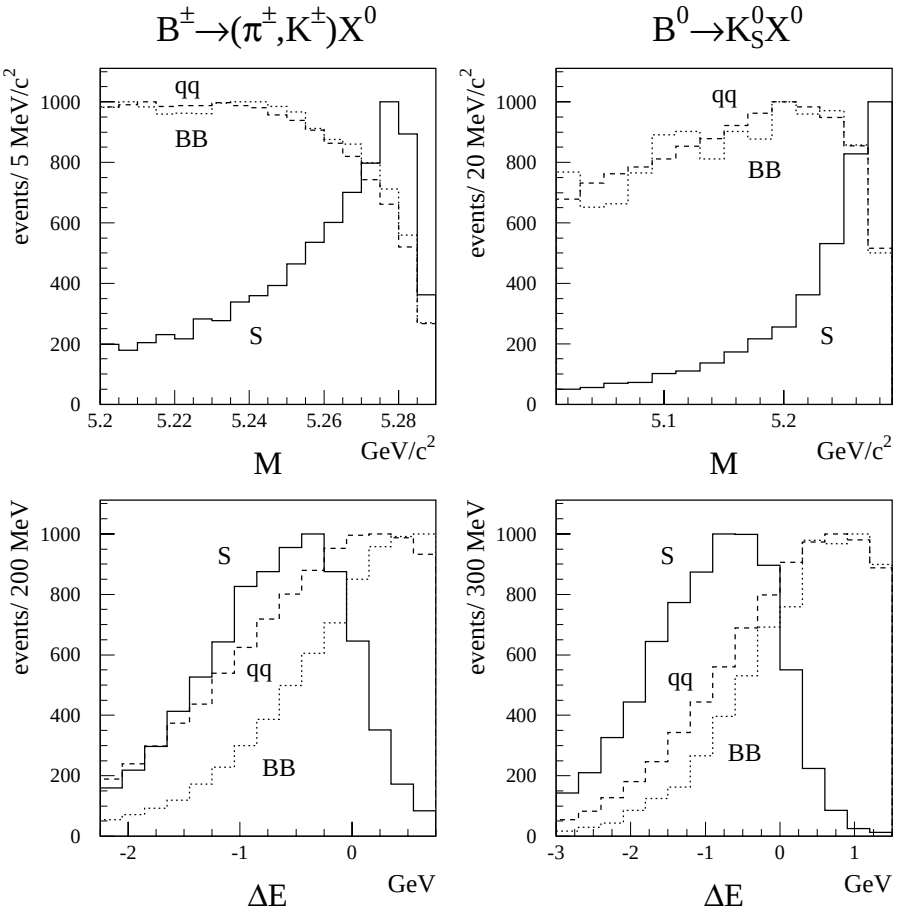

Figure V.5: Distribution of beam constrained mass M (top) and energy difference ΔE (bottom) for signal (S, solid histogram), continuum $e + e^- \rightarrow q\bar{q}$ (dashed histogram) and $B\bar{B}$ (dotted histogram) simulated Monte Carlo samples.

Although, the beam-constrained B mass distribution peaks at 5.28 GeV/c^2 for signal as it is expected, it has a long tail because of the information loss mentioned in the previous paragraph. Due to the same reason, the ΔE distributions are widened and the peak of the signal distribution is shifted below zero. However, there is a clear difference between signal and background, especially in the distribution of M, which can be used to suppress the background resulting from both unwanted $B\bar{B}$ and continuum $q\bar{q}$ events.

V.2.3 Continuum Suppression

As we pointed out in Section V.1 the constraint on the momentum of the signal meson (h) eliminates most of the background coming from B meson decays via the dominant charm decay of the b quark ($b \to cW$), which is simulated in the generated $B\bar{B}$ Monte-Carlo sample. Other than that only rare charmless B decays, proceeding through $b \to uW$ or $b \to q_d$ ($q_d = d, s$) penguin mechanisms, can contribute to the background but these processes are suppressed and have a branching fraction of $\lesssim 10^{-5}$.

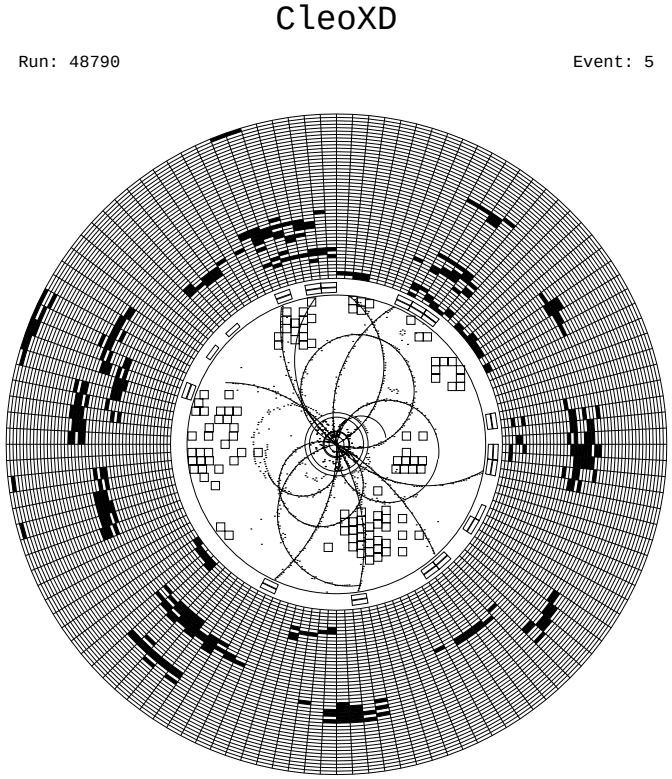

Figure V.6: Distribution of particles in a typical $B\bar{B}$ event. The curves in the central region are reconstructed charged tracks along the hit wires (black dots). The black segments in the outer region represents hits in the electromagnetic calorimeter.

Hence, the main contribution to the background comes from continuum $e^+e^- \to q\bar{q}$

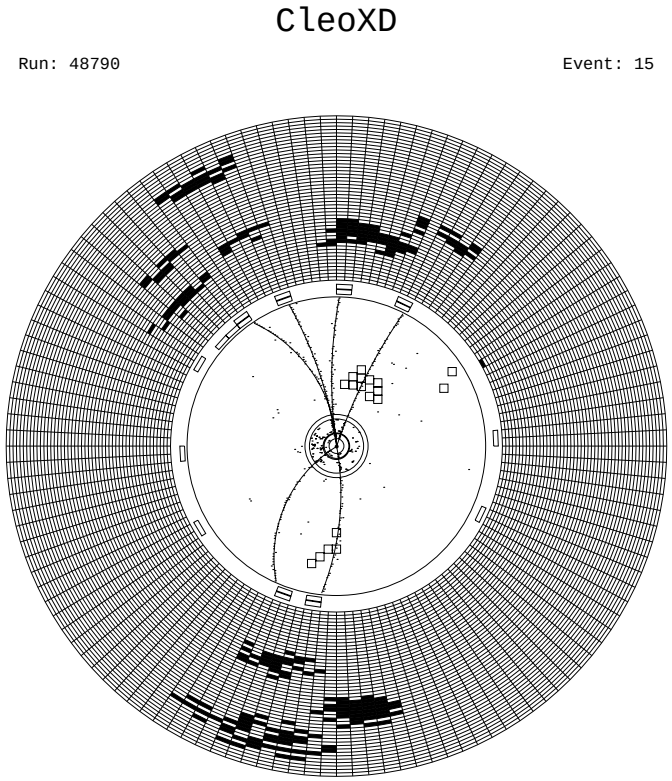

Figure V.7: Distribution of particles in a typical $q\bar{q}$ event. The curves in the central region are reconstructed charged tracks along the hit wires (black dots). The black segments in the outer region represents hits in the electromagnetic calorimeter.

$(q = u, d, c, s)$ events as it was demonstrated on Fig. V.2. In order to suppress this type of background we can take advantage of the difference in the decay distributions of $q\bar{q}$ and signal $B\bar{B}$ events. The B mesons are produced nearly at rest ($p_B \approx 320 MeV/c$) through the decay of the $\Upsilon(4S)$ resonance. Therefore, their decay products can go in any direction resulting in an isotropic event distribution. Distribution of tracks and neutral showers in the detector are shown on Fig. V.6 for a typical $B\bar{B}$ event. In contrast, the two quarks produced in the process $e^+e^- \rightarrow q\bar{q}$ have a substantial amount of momentum because of the small rest mass of the accessible u, d, c and s quarks compared to the total energy of the

reaction (10.58 GeV). After hadronization, the two large momentum quarks produce back to back showers of particles, called jets. This two-jet structure is demonstrated on Fig. V.7.

Event Shape Variables

We can define several event shape variables, which reflect the difference in the event distribution of signal and continuum background, and can be used to enhance the signal to background ratio. We give a short description of those variables, which are used in our analysis.

Momentum flow: We divide the space around the axis defined by the direction of the signal meson into nine concentric double cones as it is shown on Fig. V.8. The i^{th} cone covers the polar angle from $(i-1)10^\circ$ to $i10^\circ$. The momentum flow in each cone is calculated as

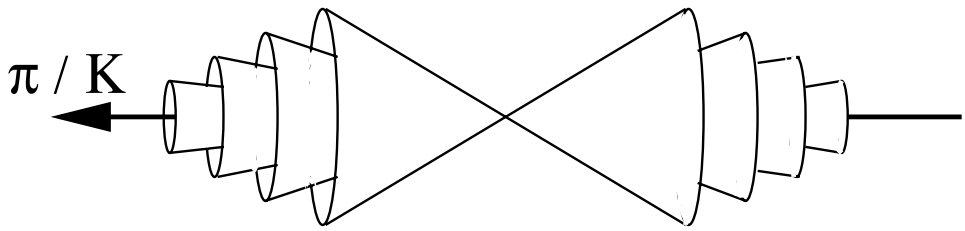

Figure V.8: Illustration of the double cones used to calculate the momentum flow variables. Only four out of the nine cones are shown.

$$\sum_{j \in i^{th}\text{cone}} p_j, \tag{V.8}$$

where the sum runs over all the tracks and showers pointing into the i^{th} cone. We used the same set of tracks and showers, which was selected to calculate the M and ΔE variables of the second B meson. The momentum in the forward and backward cones were combined to end up with nine momentum flow variables.

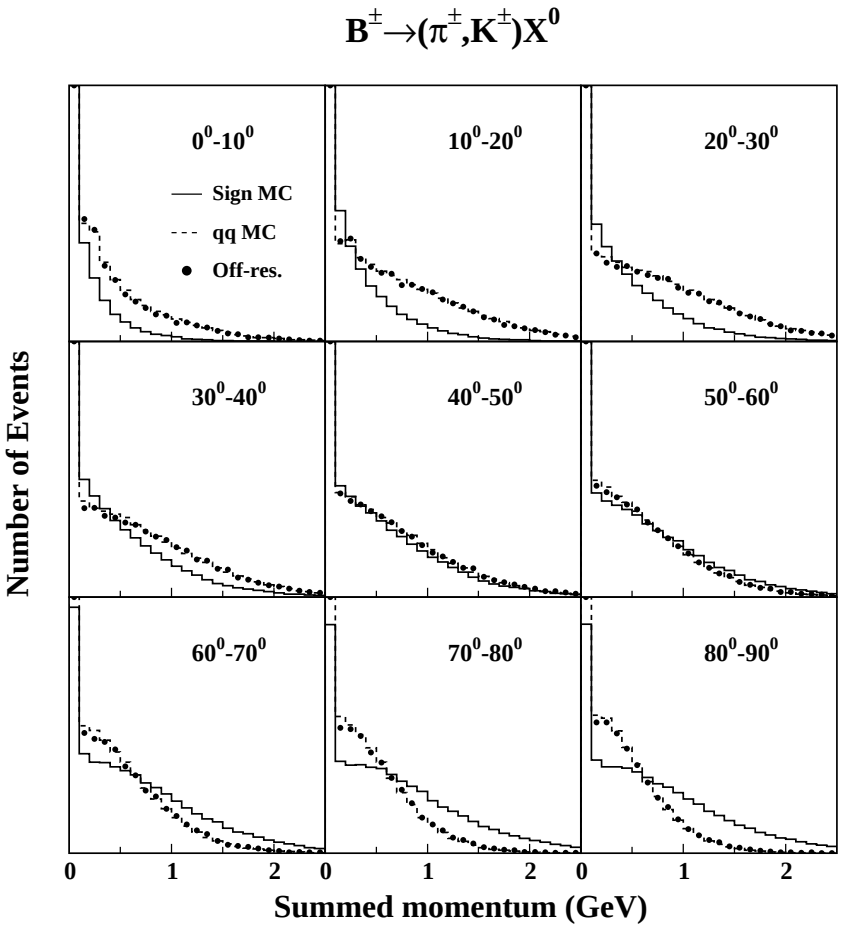

Figure V.9: Distribution of the momentum flow variables in the nine concentric cones for $B^{\pm} \to h^{\pm}X^0$ decay. Dots represent the off-resonance continuum $e^+e^- \to q\bar{q}$ data while the histograms show simulated signal (solid) and continuum background (dashed) for comparison. The histograms are normalized to the area of the data.

Figure V.9 and V.10 show the distribution of these variables for simulated signal and continuum Monte-Carlo events and off-resonance $e^+e^- \to q\bar{q}$ sample. We can note the difference between the signal and continuum background distributions. While the signal events distribute momentum proportional to the solid angle covered by the cone, the $q\bar{q}$ events tend to deposit more momentum along the direction of the signal meson candidate.

$|\cos\Theta_B|$: Θ_B is the flight direction of the B meson with respect to the e^+e^- collision

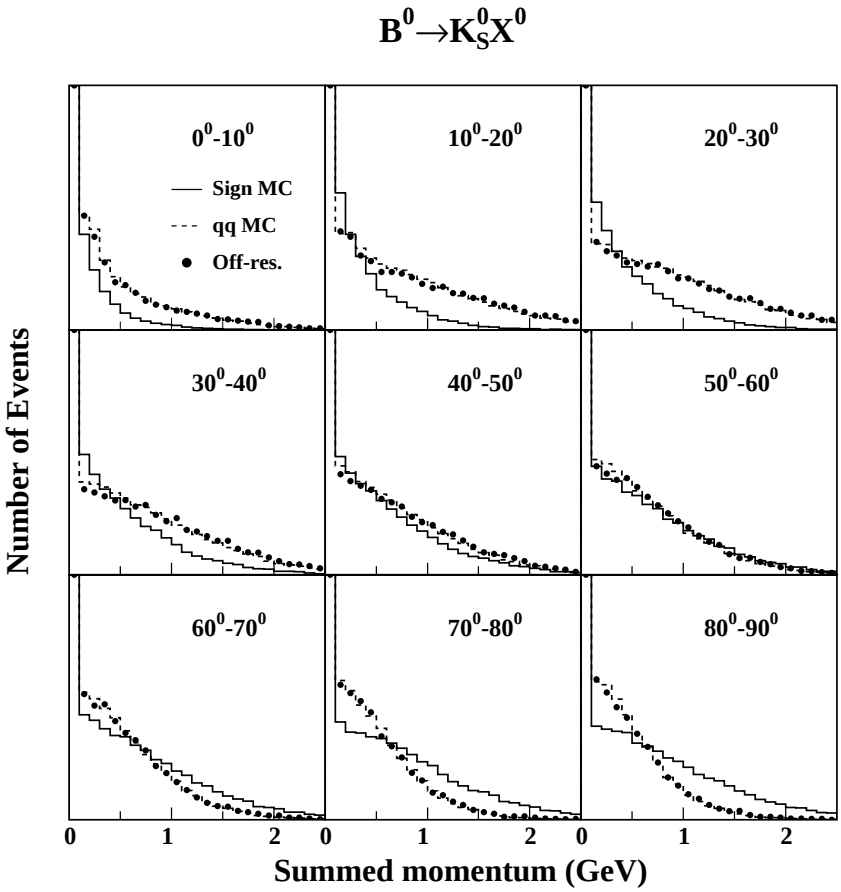

Figure V.10: Distribution of momentum flow variables in the nine concentric cones for $B^0 \to K^0_S X^0$ decay. Dots represent the off-resonance continuum $e^+e^- \to q\bar{q}$ data while the histograms show simulated signal (solid) and continuum background (dashed) for comparison. The histograms are normalized to the area of the data.

("beam") axis. Angular momentum conservation requires the cosine of this angle to exhibit a $1 - \cos^2 \Theta_B$ distribution while the continuum background should have a flat distribution.

Since we are not able to reconstruct the momentum of our B meson decaying to the light signal meson and the undetectable familon, we used the rest of the observed particles in the event to "quasi"-reconstruct the direction of the other B. Unfortunately, the distribution of the other B direction in the signal is flattened as it is shown on Fig. V.11, due to the fact

that the momentum of the B meson is small compared to the daughters' momentum and that the detector and the track-reconstructing software is unable to recover every particle precisely.

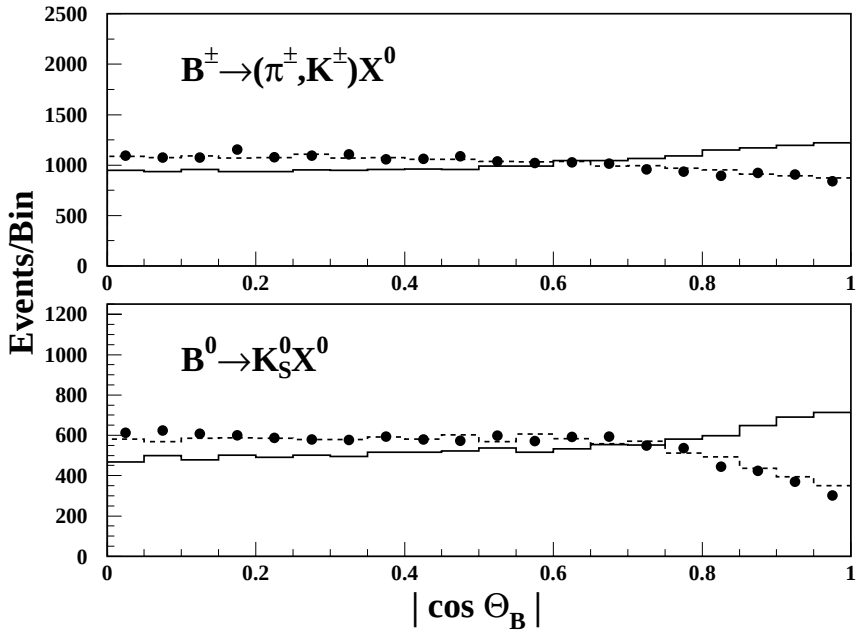

Figure V.11: Distribution of $|\cos\Theta_B|$ variable. Dots represent off-resonance data while the histograms are simulated signal (solid) and continuum $q\bar{q}$ (dashed) Monte-Carlo samples. The histograms are normalized to the area of the data.

Although, the distribution of our $\cos\Theta_B$ variable does not show the characteristics expected for a strictly reconstructed B meson, there is a definite difference between the signal and background distributions, which proved to be useful to suppress the latter.

$|\cos\Theta_h|$: Θ_h is the flight direction of the signal meson with respect to the beam axis. As Fig. V.12 shows the $\cos\Theta_h$ distribution for continuum background peaks around ± 1, that is in the direction of the beam axis, while it is flat for signal events.

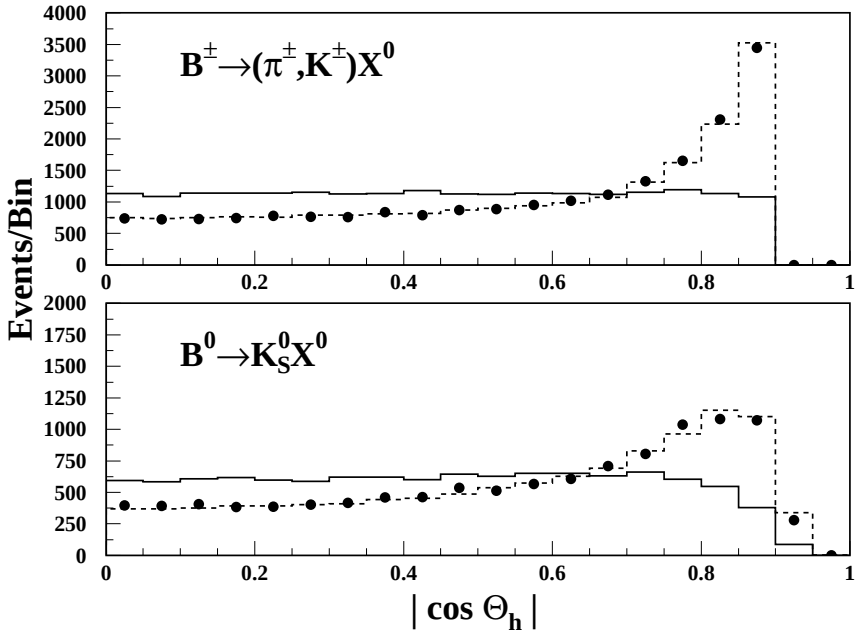

Figure V.12: Distribution of $|\cos\Theta_h|$ variable. Dots represent off-resonance data while the histograms are simulated signal (solid) and continuum $q\bar{q}$ (dashed) Monte-Carlo samples. The histograms are normalized to the area of the data.

The behavior of the background can be explained if we consider that the direction of the signal meson candidate picked from one of the two back-to-back hadron jets must be close to the jet axis. When the jet axis lies close to beam axis one or more particles from the other jet opposite to the signal meson have a good chance to escape from detection through the beam pipe. Therefore, these events can mimic a signal event due to the missing momentum/energy and have a better chance to pass the preliminary kinematic selection criteria on M and ΔE and produce the excess in the $\cos\Theta_h$ distribution around ± 1.

The sharp cut off at 0.9 in the distribution of $|\cos\Theta_h|$ on the plot for $B^{\pm} \to (\pi^{\pm}, K^{\pm})X^0$ is the result of the selection criterion on the signal meson candidate (see section V.2.1). We did not require a similar criterion on the polar angle of the K^0_S candidate. However, the

$|\cos\Theta_{K^0_S}|$ distribution (lower plot on Fig. V.12) gradually approaches zero around 0.9 since reconstruction efficiency gets worse close to the beam axis (the two pions from the subsequent decay of the K^0_S are emitted forward due to its large momentum).

$\boldsymbol{R_2}$: This variable is the second order normalized Fox-Wolfram moment: H_2/H_0. The n^{th} order Fox-Wolfram moment [59] is defined by

$$H_n = \sum_{i,j} \frac{p_i p_j}{E^2} P_n(\cos\Theta_{ij}), \tag{V.9}$$

where we sum over all particle pairs in the event, $p_{i(j)}$ are the momentum of the particles, E is the total energy of the event, P_n is the n^{th} order Legendre polinom and Θ_{ij} is the angle between the momentum vectors. Since $P_0(x) \equiv 1$ it can be seen that H_0 is only a kinematic normalization.

R_2 is close to zero for isotropic events while it approaches 1 as the event gets more jet-like. In the extreme case with two co-linear particles

$$P_2(\cos\Theta) = \frac{1}{2}(3\cos^2\Theta - 1) = 1 \tag{V.10}$$

and it results $R_2 = 1$. The distribution of R_2 for signal and $q\bar{q}$ continuum background is shown on Fig. V.13. As a preliminary selection criteria to skim events we required $R_2 < 0.5$.

$\boldsymbol{|\cos\Theta_{th}|}$: $\Theta_{\rm th}$ is the angle between the direction of the signal meson candidate and the thrust axis of the rest of the event. The thrust axis is defined by the axis (with unit vector $\vec{t}$) on which the sum of the projection of the momentum vectors, $\sum_i \vec{p}_i \cdot \vec{t}$, is the largest. For a single particle it is parallel to the momentum of the particle. In case of two particles it is co-linear with the longer diagonal of the parallelogram spanned by the two momenta.

To define the thrust axis for the rest of the event we used those particles, which were selected to calculate the M, ΔE, and the momentum flow variables earlier. In a $q\bar{q}$ event, the signal meson candidate is picked from the tracks making up the two jets and therefore

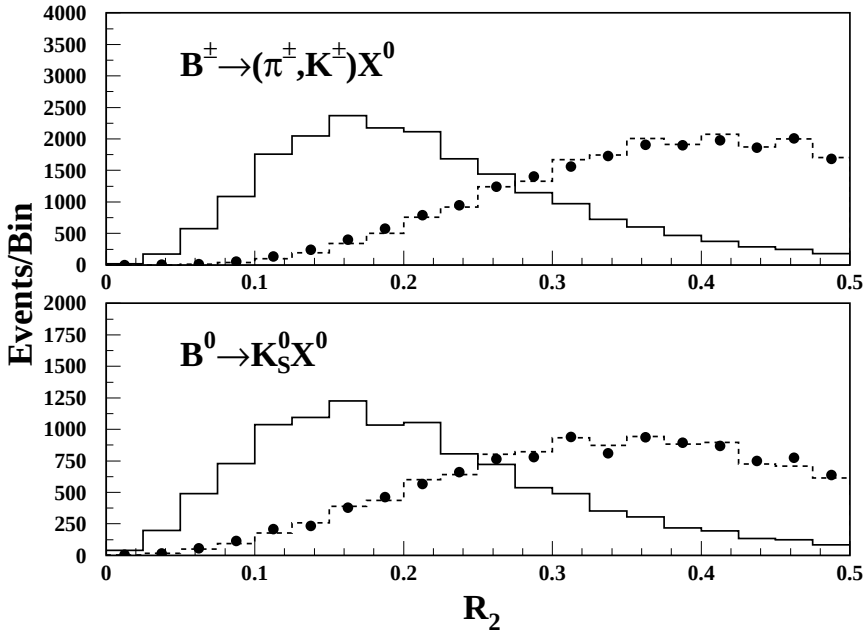

Figure V.13: Distribution of R_2 variable. Dots represent off-resonance data while the histograms are simulated signal (solid) and continuum $q\bar{q}$ (dashed) Monte-Carlo samples. The histograms are normalized to the area of the data.

its direction is strongly correlated with the thrust axis of the rest of the event. Hence, the distribution of $\cos\Theta_{\rm th}$ picks at ± 1 for continuum background. In contrast, because of the small momentum of the B mesons and the nearly isotropic angular distribution of the decay products from the second B meson, the direction of the thrust axis of these particles with respect to the direction of the signal meson candidate coming from the other B is random in $B\bar{B}$ events. Thus, the signal tend to have a flat $\cos\Theta_{\rm th}$ distribution as it is illustrated on Fig. V.14.

$\mathbf{\cos\Theta_{empty-cone}}$: This variable is the cosine of the maximum opening angle of the cone opposite to the direction of the signal meson candidate, in which no other charged track, π^0 or K^0_S was detected (see Fig. V.15). For the purpose to calculate this variable we selected

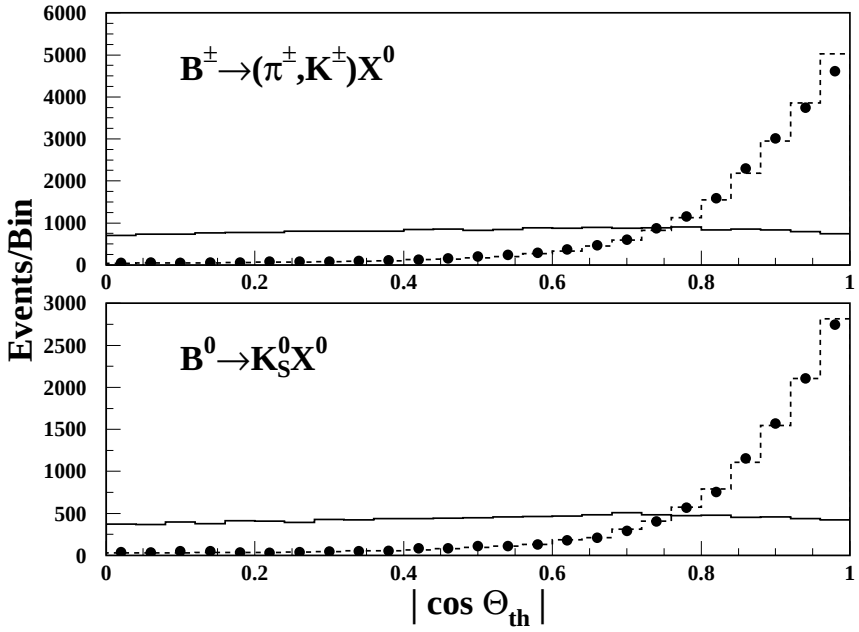

Figure V.14: Distribution of $|\cos\Theta_{\rm th}|$ variable. Dots represent off-resonance data while the histograms are simulated signal (solid) and continuum $q\bar{q}$ (dashed) Monte-Carlo samples. The histograms are normalized to the area of the data.

K^0_S's using the same criteria, which were defined for the signal K^0_S mesons (except the momentum constraint) and we did not take into account the daughter pions as individual charge particles again. The π^0's were reconstructed via their decay to $\gamma\gamma$, which has a $\sim 99\%$ relativ e branching fraction. To eliminate fake $\gamma\gamma$ combinations we accepted candidates with momentum larger than 100 MeV/c and required a satisfactory kinematic fit to the real mass ($\chi^2 \leq 7$).

In a continuum $q\bar{q}$ event the cone opposite to the signal meson is heavily populated with particles from the other jet, while in a signal event it has a quite small probability that one of the decay products from the other B meson enters this cone (see Fig. V.16).

Although, each of the variables described here is capable of distinguishing signal events

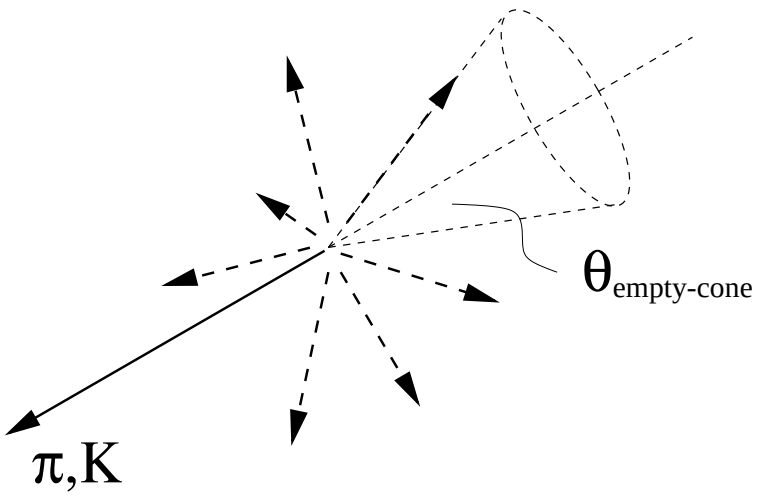

Figure V.15: Illustration of the empty cone. The arrows represent the momenta of particles measured in the detector.

from background to some extent, their individual distinguishing power is strongly limited. In addition, they are correlated with each other, that is if we restrict the values of one variable then the distribution of the others will change. Therefore, it is necessary to combine our numerous shape variables into one single variable, which concentrates the distinguishing power of the individual variables and yields maximal discrimination between the signal and background. At CLEO, the technique of Fisher Discriminant [60] was successfully implemented in several analysis (see for example [61]).

Fisher Discriminant Technique

The Fisher Discriminant is expressed as a linear combination of the input variables (x_i) described in the previous section:

$$\mathcal{F}(x_1, x_2, ..., x_N) = \sum_{i=1}^{N} \alpha_i x_i, \tag{V.11}$$

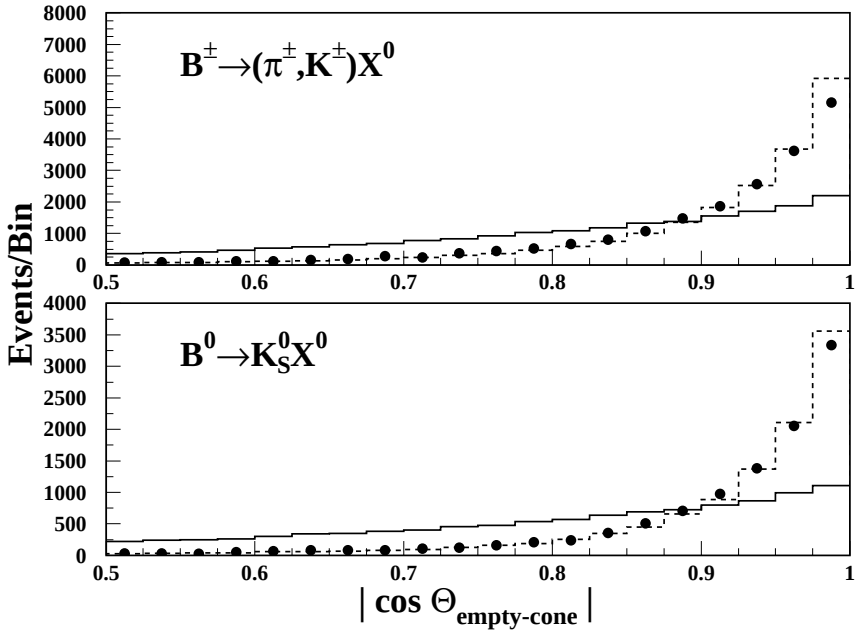

Figure V.16: Distribution of $|\cos\Theta_{\text{empty-cone}}|$ variable. Dots represent off-resonance data while the histograms are simulated signal (solid) and continuum $q\bar{q}$ (dashed) Monte-Carlo samples. The histograms are normalized to the area of the data.

and the linear coefficients α_i are determined as to maximize the separation between the signal and continuum background

$$\alpha_i = \sum_{j=1}^{N} (U^s_{ji} + U^b_{ji})^{-1} \times (\mu^b_j - \mu^s_j), \tag{V.12}$$

where $\mu_j = \langle x_j \rangle$ is the mean of the distribution of the j^{th} variable and U_{ji} is the covariance matrix between the variables

$$U_{ji} = \langle (x_j - \mu_j)(x_i - \mu_i) \rangle = \langle x_j x_i \rangle - \mu_j \mu_i, \tag{V.13}$$

and the superscript s and b denote signal and background, respectively.

In order to demonstrate how the α coefficients separate signal from background we look at the special case when the input variables are uncorrelated for both signal and background,

that is

$$U_{ji} = 0 \qquad (j \neq i). \tag{V.14}$$

Then the covariance matrix becomes diagonal and only the σ^2 variance of each variable's distribution shows up in it

$$U_{ji} = \begin{pmatrix} (\sigma_1)^2 & 0 & 0 & 0 & ... \\ 0 & (\sigma_2)^2 & 0 & 0 & ... \\ 0 & 0 & (\sigma_3)^2 & 0 & ... \\ ... & ... & ... & ... & ... \end{pmatrix} \tag{V.15}$$

since

$$U_{jj} = \langle (x_j - \mu_j)^2 \rangle = (\sigma_j)^2. \tag{V.16}$$

Hence, the combination coefficients are simply given by

$$\alpha_i = \frac{\mu_i^b - \mu_i^s}{(\sigma_i^s)^2 + (\sigma_i^b)^2}, \tag{V.17}$$

that is variables which have larger signal versus background separation (numerator) and smaller variance (denominator) are weighted more heavily in the composition of the Fisher Discriminant.

To determine the α_i coefficients, that is to "tune" the Fisher Discriminant, we need separate signal and continuum $q\bar{q}$ background samples. We do not have too many choices with the signal since the only source is our Monte-Carlo generated sample. Although, for background, we could use the off-resonance data, we decided to use the Monte-Carlo simulated continuum samples instead. The quality of agreement between the distributions of each variable for off-resonance data and the Monte-Carlo simulation justifies this choice. We use the background data samples from off-resonance running as a check only and to determine the systematic error associated with the Fisher selection criterion.

We used only those events, which passed the pre-selection criteria on M, ΔE, R_2 and the tight momentum cut $2.47 < p_{K_S^0} < 2.79$ GeV/c or $2.49 < p_{\pi^\pm,K^\pm} < 2.81$ GeV/c: $44,185$ $B^\pm \to \pi^\pm X^0$ ($32,581$ $B^0 \to K_S^0 X^0$) signal MC events and $140,818$ (46,097) continuum $q\bar{q}$ MC events. The resulting combination coefficients are given in Table V.2 for both decay modes.

Table V.2: Combination coefficients of the variables in the Fisher Discriminant

Variable	$B^\pm \to (\pi^\pm, K^\pm)X^0$	$B^0 \to K_S^0 X^0$
Momentum Flow $(0^\circ - 10^\circ)$	0.775	0.887
Momentum Flow $(10^\circ - 20^\circ)$	0.685	0.876
Momentum Flow $(20^\circ - 30^\circ)$	0.508	0.788
Momentum Flow $(30^\circ - 40^\circ)$	0.260	0.555
Momentum Flow $(40^\circ - 50^\circ)$	0.031	0.307
Momentum Flow $(50^\circ - 60^\circ)$	-0.169	0.106
Momentum Flow $(60^\circ - 70^\circ)$	-0.347	-0.081
Momentum Flow $(70^\circ - 80^\circ)$	-0.456	-0.218
Momentum Flow $(80^\circ - 90^\circ)$	-0.502	-0.283
$\mid \cos\Theta_B \mid$	-0.222	-0.364
$\mid \cos\Theta_P \mid$	0.949	1.129
R_2	1.786	0.730
$\mid \cos\Theta_{\rm th} \mid$	0.520	0.486
$\cos\Theta_{\rm empty-cone}$	0.056	0.239

Figures V.17 and V.18 show the distribution of the Fisher variables for simulated signal and continuum samples as well as for off-resonance data. As we can see the distribution of the Fisher Discriminant is approximately Gaussian (in fact, it is a bifurcated Gaussian) as it is expected from the Central Limit Theorem. The Fisher Discriminant on these figures are normalized to give distributions in the range $0 - 1$. We can see again how well the Monte-Carlo simulates the data. The separation between the signal and background distributions

is around 95% (86%) of the sum of the standard deviations of the two distributions ($\sigma^s + \sigma^b$) in case of the charged (neutral) decay mode.

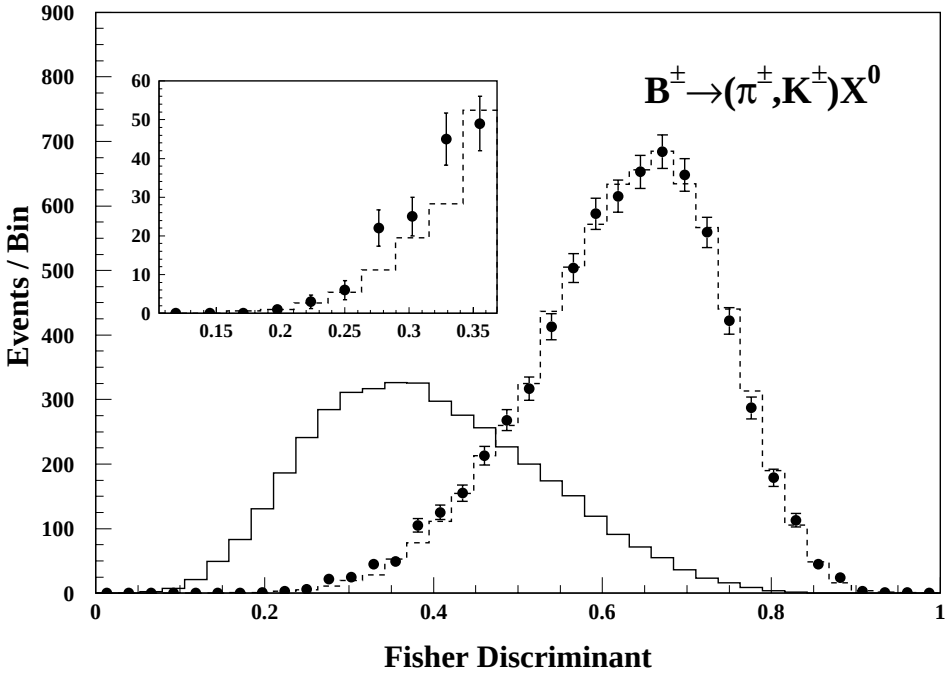

Figure V.17: Distribution of the Fisher Discriminant for $B^{\pm} \to (\pi^{\pm}, K^{\pm})X^0$. Dots represent off-resonance data while the histograms are simulated signal (solid) and continuum $q\bar{q}$ (dashed) Monte-Carlo samples. The histograms for continuum MC is normalized to the statistics of the off-resonance data while the signal distribution is plotted assuming a branching fraction of 3×10^{-3}. Inset shows the left tail of the continuum distribution.

A cut on the Fisher Discriminant represents a hyperplane, which separates signal events from background in the 14-dimensional variable space. Although, this technique relies on the assumption that the signal and background is linearly separable in this space, this seems to be a reasonable assumption considering the distribution of our variables. This is the reason

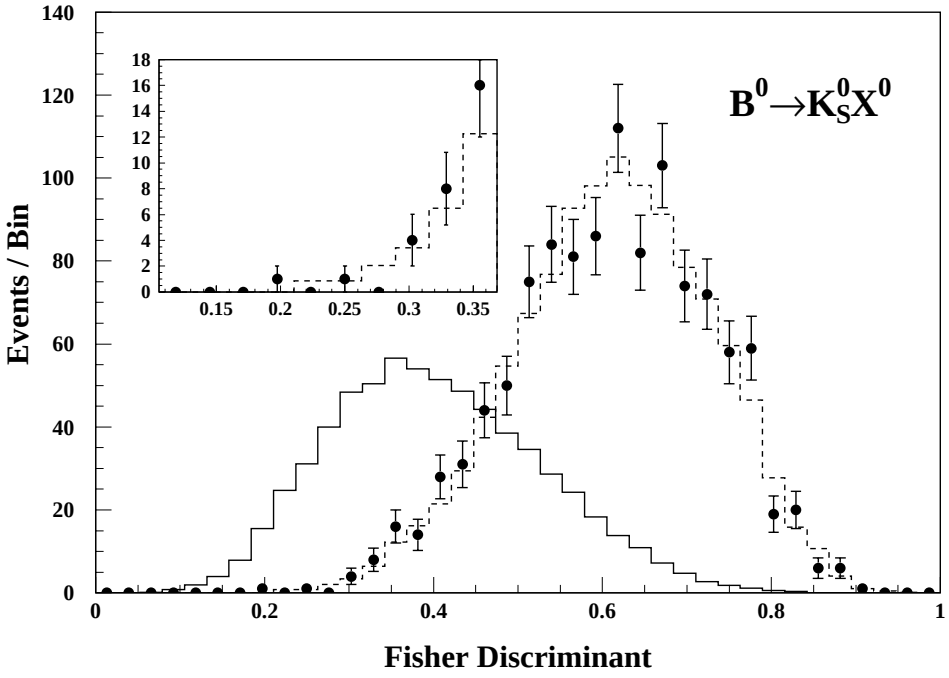

Figure V.18: Distribution of the Fisher Discriminant for $B^0 \to K^0_S X^0$. Dots represent off-resonance data while the histograms are simulated signal (solid) and continuum $q\bar{q}$ (dashed) Monte-Carlo samples. The histograms for continuum MC is normalized to the statistics of the off-resonance data while the signal distribution is plotted assuming a branching fraction of 7×10^{-4}. Inset shows the left tail of the continuum distribution.

why the absolute value of some of the variables (e.g. the cosine of the thrust angle), are taken in the calculation since this transformation makes signal and background linearly separable. However, there are more sophisticated methods, such as those based on neural network, that can use a nonlinear algorithm to improve the separation in those cases when inherent non-linear correlations exist among the input variables. But these methods become more complicated with increasing number of variables, and convergence to a global optimum is not guaranteed and depends on initial conditions. We chose the Fisher Discriminant technique

because of its simplicity and it proved to be as powerful as other methods in several CLEO analysis [62].

V.3 Optimization of Selection Criteria

As we mentioned earlier we applied some loose preliminary criteria on some of the variables in order to reduce the size of the data and get a manageable subset, which can be further studied in a faster and more flexible way. Table V.3 summarizes these criteria for both decay modes.

Table V.3: Summary of the skim cuts.

$B^{\pm} \to (\pi^{\pm}, K^{\pm})X^0$	$B^0 \to K_s^0 X^0$
Good $\pi^{\pm}/K^{\pm}$ candidate	Good K_s^0 candidate
with $2.1 < p_{\pi/K} < 3.1$ GeV/c	with $2.1 < p_{K_s^0} < 3.1$ GeV/c
$R_2 < 0.5$	$R_2 < 0.5$
$M \geq 5.2$ GeV/c^2	$M \geq 5.0$ GeV/c^2
$-3.25 \leq \Delta E \leq 1.0$ GeV	$-3.5 \leq \Delta E \leq 1.0$ GeV

We have decided to do a "cut-and-count" (also known as slice-and-dice) analysis, that is, we set a branching ratio or an upper limit based on the number of events surviving our selection criteria, which are designed to enhance the signal as much as possible relative to the background. To avoid any bias introduced by statistical fluctuations in the data we used Monte-Carlo generated samples in the process of cut optimization. In order to measure quantitatively the effectiveness of a particular cut, we defined a quality factor, which expresses the relative improvement in the signal significance:

$$Q = \frac{G^2_{\text{cut}}}{G^2_{\text{no cut}}}, \tag{V.18}$$

where $G_{\rm cut}$ ($G_{\rm no\ cut}$) is the statistical significance of the signal after (before) the cut is applied.

The signal significance can be expressed as the ratio of the number of signal events to its statistical error

$$G^2 = \frac{S^2}{(\delta S)^2}. \tag{V.19}$$

Let us assume that N events containing S signal and B background were observed in the on-resonance sample: $N = S+B$. The background consists of two components, $B\bar{B}$ events other than our signal and continuum $q\bar{q}$ events, $B = B^{BB} + B^{qq}$ (other continuum processes have a negligible contribution). We can estimate these numbers using the Monte-Carlo samples: $S = \alpha S_{MC}$, $B^{BB} = \beta B^{BB}_{MC}$ and $B^{qq} = \gamma B^{qq}_{MC}$. Then the statistical error on N assuming Gaussian statistics is

$$\begin{aligned}(\delta N)^2 &= (\delta S)^2 + (\delta B)^2 \\ &= \left(\sqrt{\alpha S_{MC}}\right)^2 + \left(\sqrt{\beta B^{BB}_{MC} + \gamma B^{qq}_{MC}}\right)^2 \\ &= \alpha S_{MC} + \beta B^{BB}_{MC} + \gamma B^{qq}_{MC}.\end{aligned} \tag{V.20}$$

On the other hand, to get the number of signal events we have to subtract the estimated background from the observed N events, $S = N - B'$. Note, that $B' = B^{BB} + B^{qq}$ is the same background contribution as above but it is from an independent measurement. We usually subtract the continuum background contribution using the off-resonance sample $B^{qq} = gB^{qq}_{off}$, where g, the statistical normalization between the on-resonance and off-resonance sample, is equal to 2.0 in our case (see Section IV.2). To estimate the $B\bar{B}$ background we have no other choice than the Monte-Carlo sample. The error on B' can be

expressed as

$$\begin{aligned}(\delta B')^2 &= \beta^2(\delta B_{MC}^{BB})^2 + g^2(\delta B_{off}^{qq})^2 \\ &= \beta^2 B_{MC}^{BB} + g^2 B_{off}^{qq} \\ &= \beta^2 B_{MC}^{BB} + g\gamma B_{MC}^{qq},\end{aligned} \tag{V.21}$$

where we used the equivalence $gB_{off}^{qq} = \gamma B_{MC}^{qq}$. Hence the statistical error on the number of signal events is equal to

$$\begin{aligned}((\delta S)^2 &= (\delta N)^2 + (\delta B')^2 \\ &= \alpha S_{MC} + (1+\beta)\beta B_{MC}^{BB} + (1+g)\gamma B_{MC}^{qq},\end{aligned} \tag{V.22}$$

and then the signal significance is

$$G^2 = \frac{(\alpha S_{MC})^2}{\alpha S_{MC} + (1+\beta)\beta B_{MC}^{BB} + (1+g)\gamma B_{MC}^{qq}}. \tag{V.23}$$

The normalization factors (α, β, γ) used to scale the simulated samples to the data together with the total event numbers are summarized in Table V.4. To estimate the number of signal events in the on-resonance data sample we assumed a reasonable signal branching fraction on the order of 10^{-5}. We checked that the cut quality (Q) is not too sensitive to this value: the optimum cut values hardly change if we choose a branching ratio below 10^{-4}. The number of $q\bar{q}$ events in the on-resonance sample takes into account that approximately 2/3 of the continuum background is due to hadronic events and the rest results from QED processes, which are not modeled in the simulated $q\bar{q}$ sample.

We optimized the selection criteria on the momentum of the signal meson ($p_{\rm meson}$), the kinematic variables of the other B meson (M and ΔE) and the Fisher Discriminant ($\mathcal{F}$) composed from the shape variables. We selected cuts with maximum improvement in the quality factor Q. The cuts were studied both individually and in combination with all the

Table V.4: The number of events in the full data and Monte-Carlo samples and the scale parameters between them.

	$B^{\pm} \to (\pi^{\pm}, K^{\pm})X^0$			$B^0 \to K_s^0 X^0$		
	Signal	BB	$q\bar{q}$	Signal	BB	$q\bar{q}$
MC	180×10^3	32.1×10^6	97×10^6	90×10^3	30.4×10^6	94×10^6
On-res. Data	97	9.7×10^6	31×10^6	97	9.7×10^6	31×10^6
Scales	0.00054	0.30	0.32	0.0011	0.32	0.33

other cuts. The following six figures show the normalized distribution of the variables together with the dependence of the quality factor Q on the cut value while all the other variables are restricted at their best values. The optimum cut values are given in Table V.5 for both decay modes. The somewhat looser cuts in case of the neutral mode resulted from the cleaner K_S^0 identification.

Table V.5: Optimized selection criteria.

Variable	$B^{\pm} \to (\pi^{\pm}, K^{\pm})X^0$	$B^0 \to K_s^0 X^0$
p_{meson} [GeV/c]	$2.49 - 2.81$	$2.47 - 2.79$
M [GeV/c^2]	> 5.245	> 5.24
ΔE [GeV]	$-2.1 - +0.3$	$-3.0 - +0.4$
$\mathcal{F}$	< 0.29	< 0.33

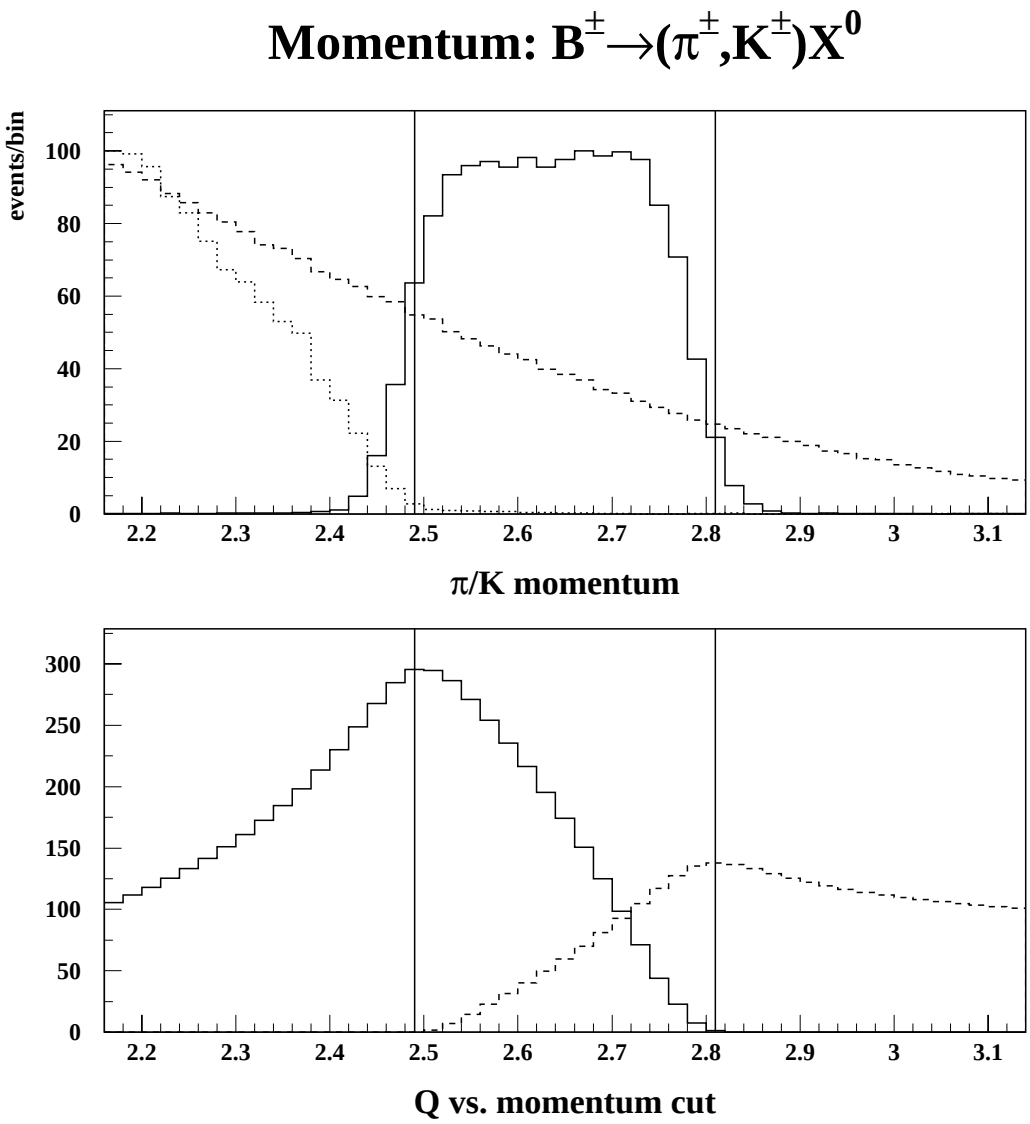

Figure V.19: Optimization of the selection criteria on the signal meson's momentum for $B^{\pm} \to (\pi^{\pm}, K^{\pm})X^0$ decay. The upper plot shows the momentum distribution of the signal meson candidate in simulated signal (solid), $B\bar{B}$ (dotted) and continuum $q\bar{q}$ (dashed) Monte-Carlo samples. The lower plot shows the quality factor (Q) as the function of the cut value for the low-momentum cut (solid) and the high-momentum cut (dashed). The vertical lines represent the optimal cuts between which we accepted events.

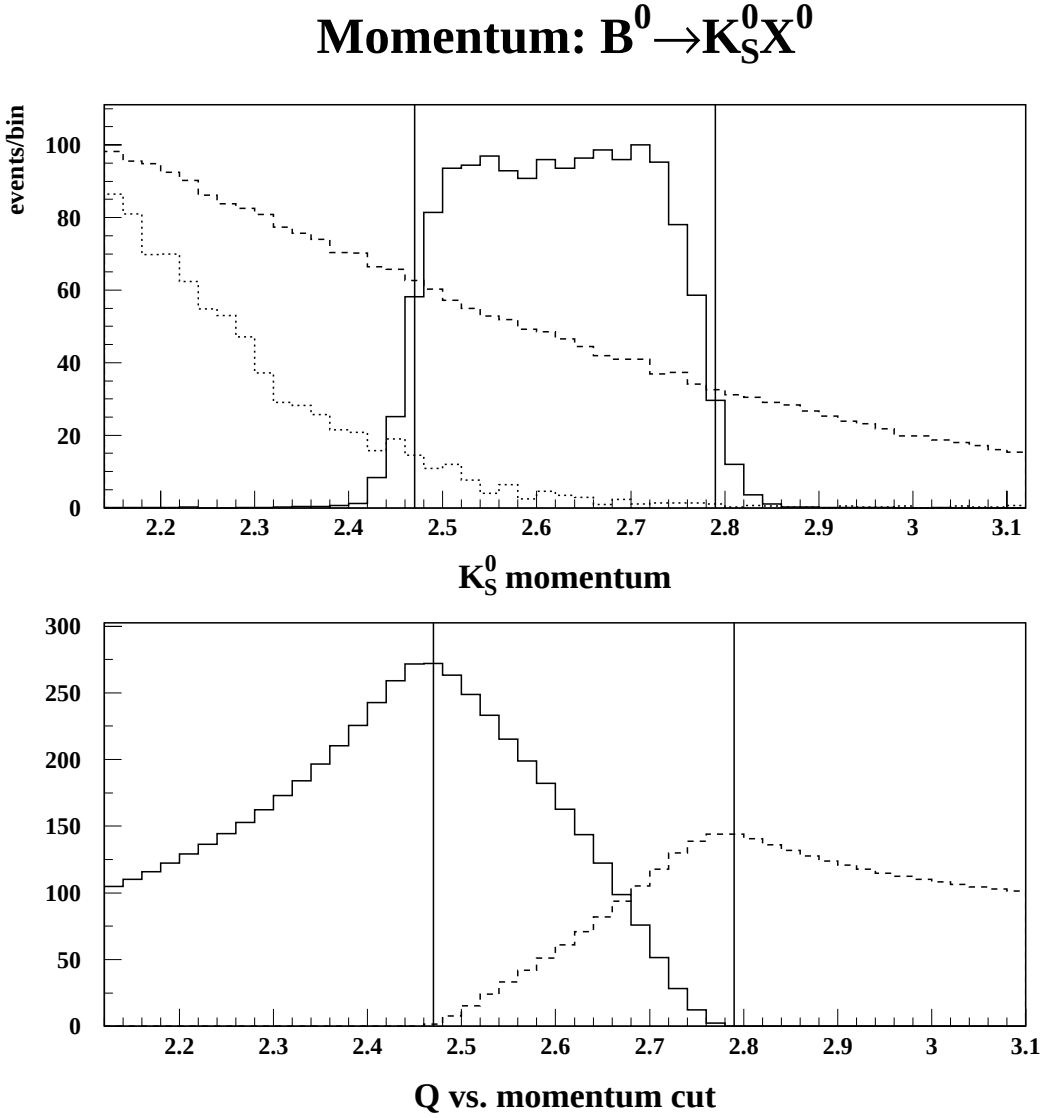

Figure V.20: Optimization of the selection criteria on the signal meson's momentum for $B^0 \to K^0_S X^0$ decay. The upper plot shows the momentum distribution of the signal meson candidate in simulated signal (solid), $B\bar{B}$ (dotted) and continuum $q\bar{q}$ (dashed) Monte-Carlo samples. The lower plot shows the quality factor (Q) as the function of the cut value for the low-momentum cut (solid) and the high-momentum cut (dashed). The vertical lines represent the optimal cuts between which we accepted events.

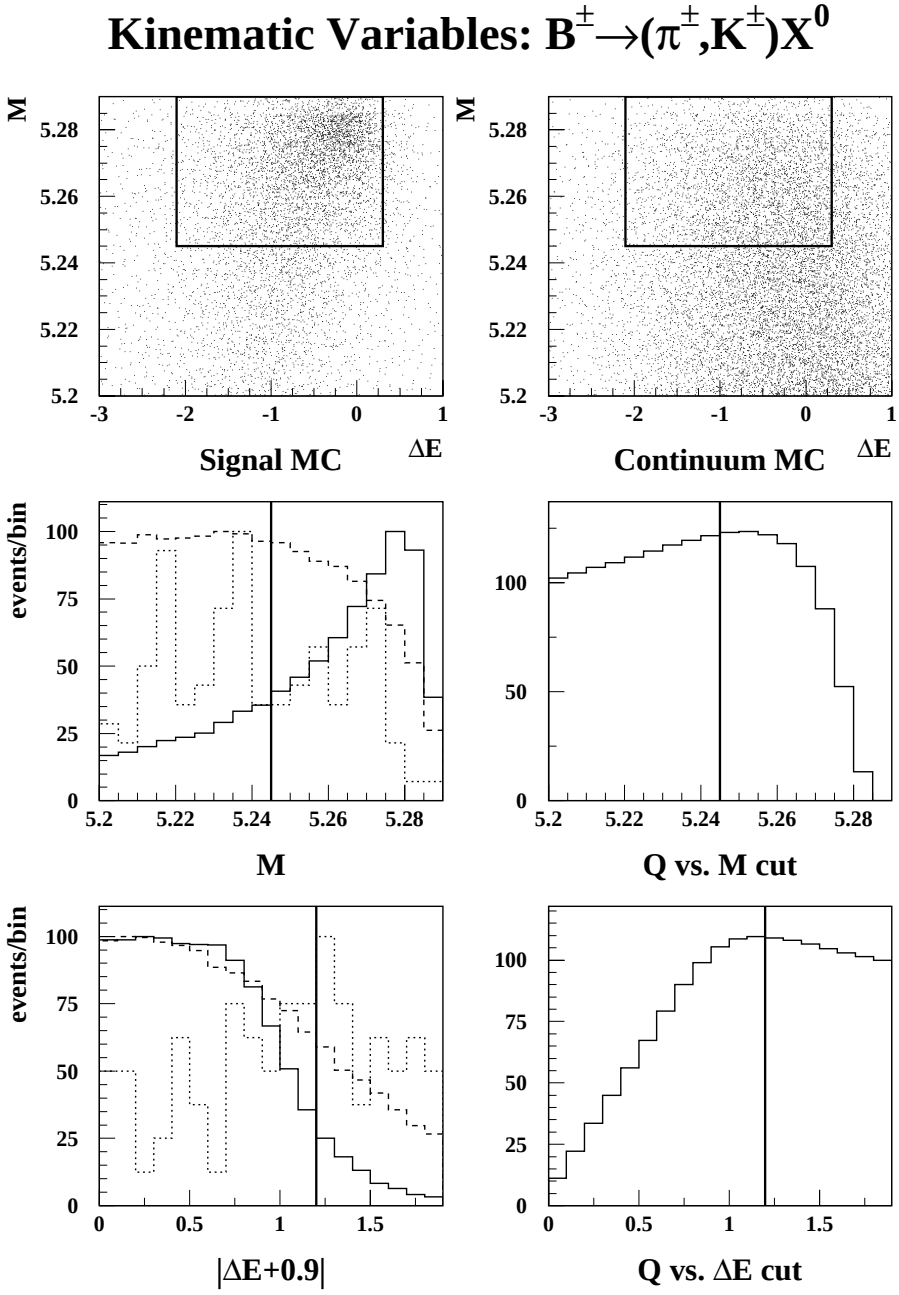

Figure V.21: Optimization of the selection criterion on the M and ΔE for $B^{\pm} \rightarrow (\pi^{\pm}, K^{\pm})X^0$ decay. The topmost plots show the two-dimensional scattered distribution of Monte-Carlo simulated signal (left) and continuum $q\bar{q}$ (right) events in the $M - \Delta E$ plane. The box represents the optimal cut. Events outside the box were rejected. One-dimensional distributions of M and ΔE variables for different Monte-Carlo samples (notation is the same as on Fig. V.19) are shown together with dependence of the quality factor Q on the cut value. The vertical lines represent the optimal cut.

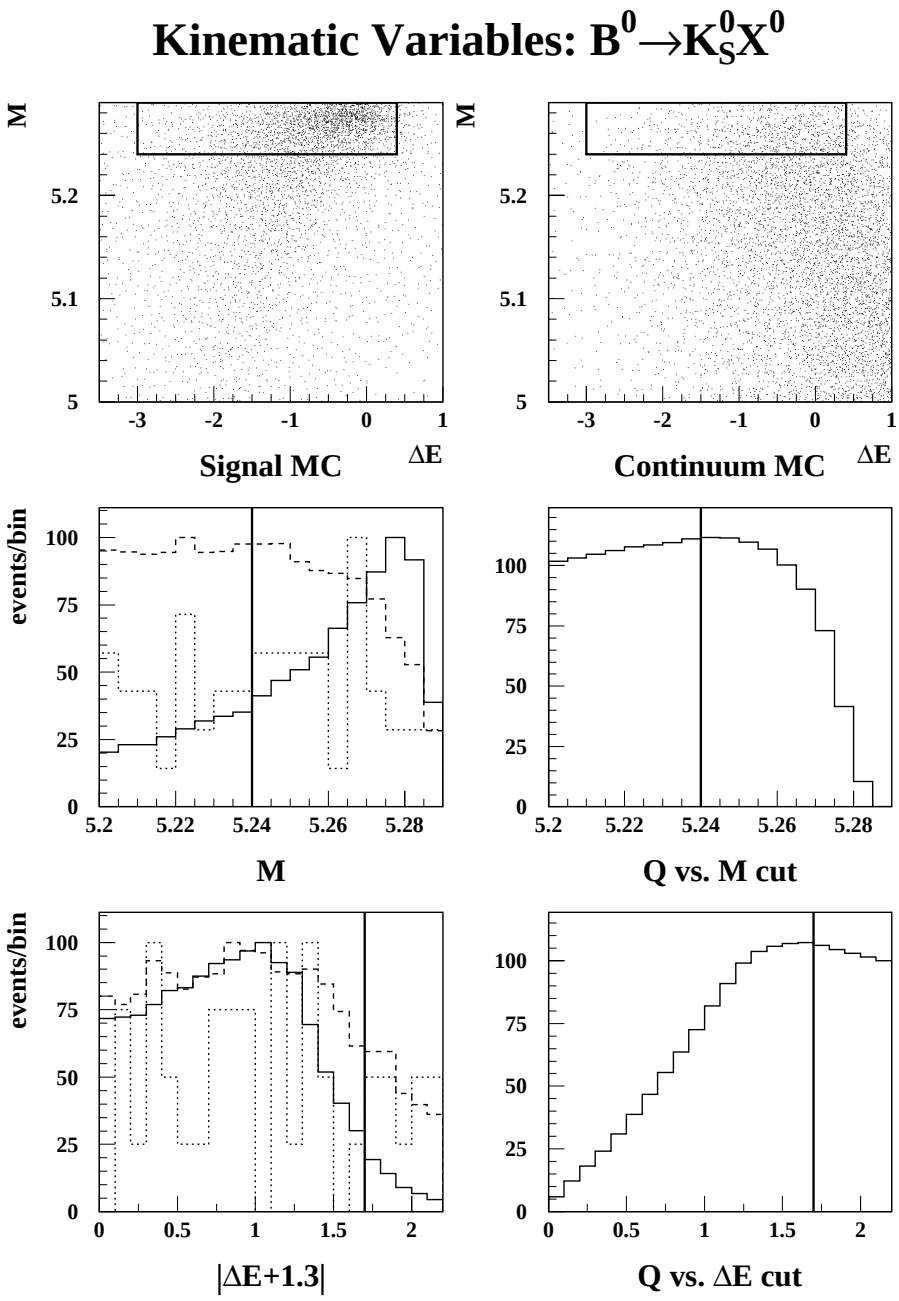

Figure V.22: Optimization of the selection criterion on the M and ΔE for $B^0 \to K^0_S X^0$ decay. The topmost plots show the two-dimensional scattered distribution of Monte-Carlo simulated signal (left) and continuum $q\bar{q}$ (right) events in the $M - \Delta E$ plane. The box represents the optimal cut. Events outside the box were rejected. One-dimensional distributions of M and ΔE variables for different Monte-Carlo samples (notation is the same as on Fig. V.19) are shown together with dependence of the quality factor Q on the cut value. The vertical lines represent the optimal cut.

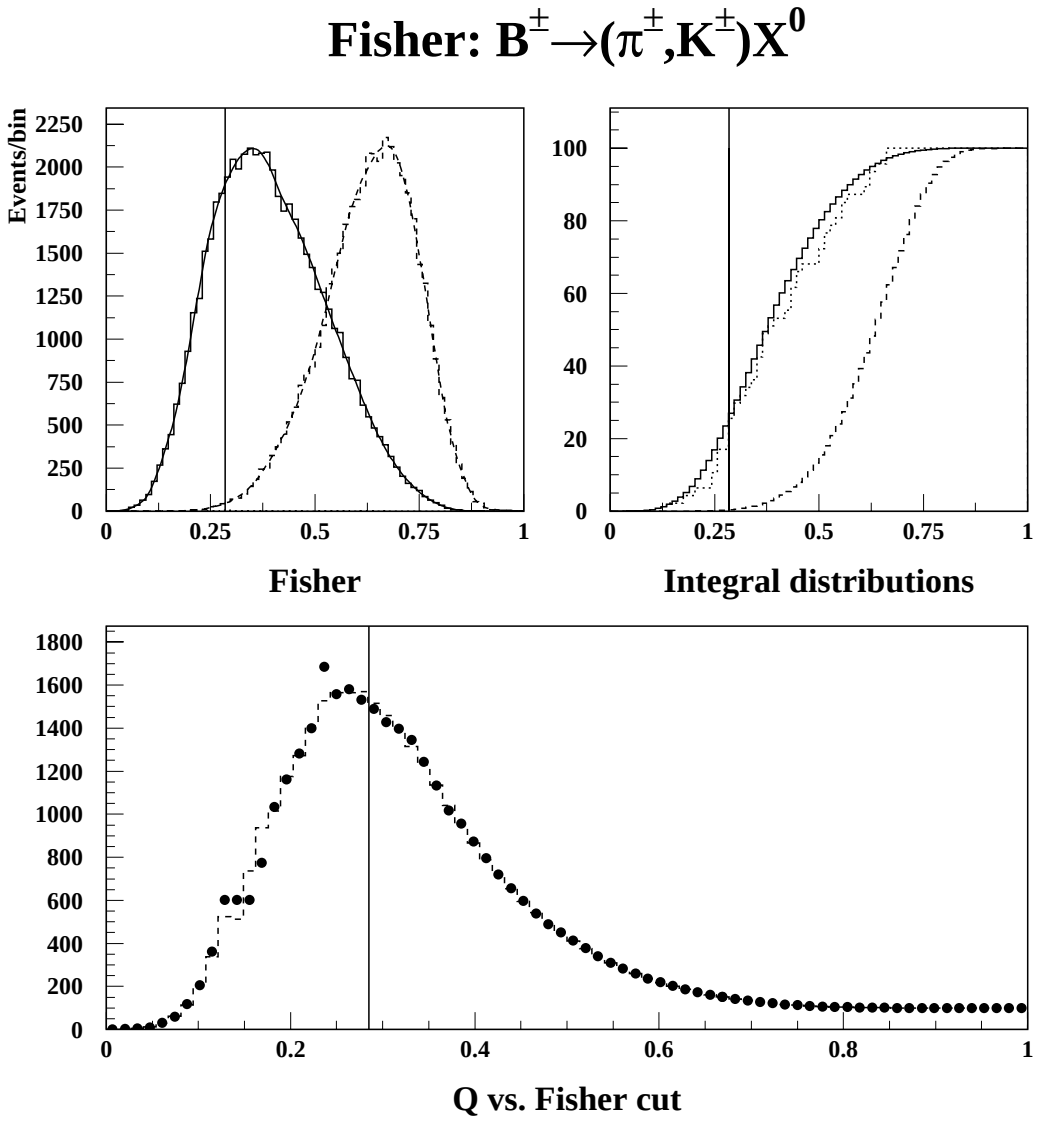

Figure V.23: Optimization of the selection criterion on the Fisher variable for $B^{\pm} \rightarrow (\pi^{\pm}, K^{\pm})X^0$ decay. The left plot on the top shows the distribution of the Fisher discriminant for signal (solid) and continuum $q\bar{q}$ (dashed) Monte-Carlo samples. The overlapping curves show the smoothed histograms. Here the distributions are not normalized to have the same height and therefore the $B\bar{B}$ background is not visible. On the right integral distributions are shown (dotted histogram shows the $B\bar{B}$ background distribution). The lower plot shows the quality factor as a function of the cut value. The dots (dashed histogram) represents the dependence resulting from using the original (smoothed) distributions.

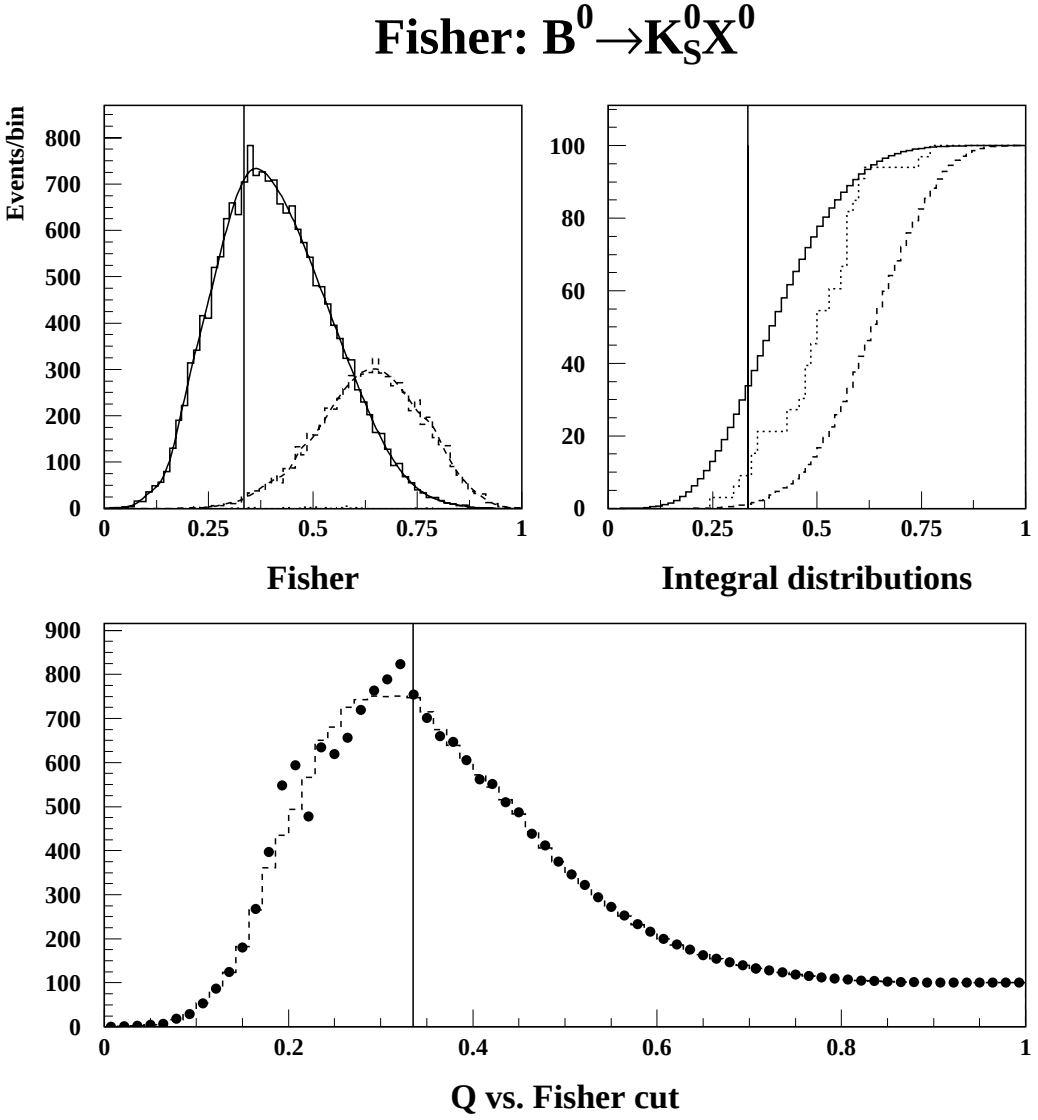

Figure V.24: Optimization of the selection criterion on the Fisher variable for $B^0 \to K^0_S X^0$ decay. The left plot on the top shows the distribution of the Fisher discriminant for signal (solid) and continuum $q\bar{q}$ (dashed) Monte-Carlo samples. The overlapping curves show the smoothed histograms. Here the distributions are not normalized to have the same height and therefore the $B\bar{B}$ background is not visible. On the right integral distributions are shown (dotted histogram shows the $B\bar{B}$ background distribution). The lower plot shows the quality factor as a function of the cut value. The dots (dashed histogram) represents the dependence resulting from using the original (smoothed) distributions.

V.4 Event yields

Tables V.6 and V.7 list the number of events passing our optimized selection requirements applied consecutively one after the other in on-resonance, off-resonance data, and simulated signal MC samples. The overall signal selection efficiency determined by using simulated signal Monte-Carlo sample is $7.2 \pm 0.1\%$ for the charged B decay mode and $6.6 \pm 0.1\%$ for the neutral B mode, where the error is statistical only.

Table V.6: Number of events passing each consecutive selection criteria in the $B^{\pm} \to (\pi^{\pm}, K^{\pm})X^0$ analysis.

	On-res.	Off-res.	MC Signal
Total events	57 million	23 million	180,000
Pre-selected events	157,919	73,671	90,211
Momentum selection	41,981	20,437	83,592
M_B and ΔE selection	14,243	7,073	55,024
Fisher selection	74	32	12,896

Table V.7: Number of events passing each consecutive selection criteria in the $B^0 \to K^0_S X^0$ analysis.

	On-res.	Off-res.	MC Signal
Total events	57 million	23 million	90,000
Pre-selected events	64,207	31,230	36,953
Momentum selection	18,675	9,224	34,720
M_B and ΔE selection	2,330	1,135	17,725
Fisher selection	44	14	5,973

Figure V.25 shows the momentum distribution of the signal meson candidate in on-resonance (filled dots) and off-resonance (empty dots) data samples along with the expected distribution from simulated samples (histograms) after all selection criteria except for the tight momentum constraint on the signal meson candidate were applied. The distributions of the off-resonance data and simulated MC events are normalized to the statistics of the on-resonance sample based on beam energy and luminosity (see Section IV.2 how these are determined). The arrows enclose the interesting momentum range in which we counted events. The number of on-resonance (off-resonance) events in the selected signal box is 74 (32) in case of the $B^{\pm} \to (\pi^{\pm}, K^{\pm})X^0$ and 44 (14) in case of the $B^0 \to K^0_S X^0$ analysis.

The distribution of the events in the 2-dimensional $M - \Delta E$ plain is shown on the two top plots of Fig. V.26 and V.27 for on-resonance (left) and off-resonance data after all other cuts were applied. The lower plots demonstrate the projected M (left) and ΔE (right) distributions for the on-resonance samples (dots with error bars) together with the Monte-Carlo predictions (histogram), which are the proper combination of $q\bar{q}$ and $B\bar{B}$ events scaled to the components of the on-resonance data.

V.5 Background

The largest contribution to the events observed in the on-resonance sample comes from $e^+e^- \to q\bar{q}$ process and it can be statistically subtracted using the off-resonance sample. However, we have to check for other possible sources, which can contribute to the background, beside the continuum $q\bar{q}$ events.

The analysis of 32 (30) million generic $B\bar{B}$ MC events, which contains only B decays governed by the dominant $b \to cW$ process, found only 8 (3) events in the signal region of the $B^{\pm} \to (\pi^{\pm}, K^{\pm})X^0$ ($B^0 \to K^0_S X^0$) analysis. It translates into ~ 2.4 and ~ 1.0 expected

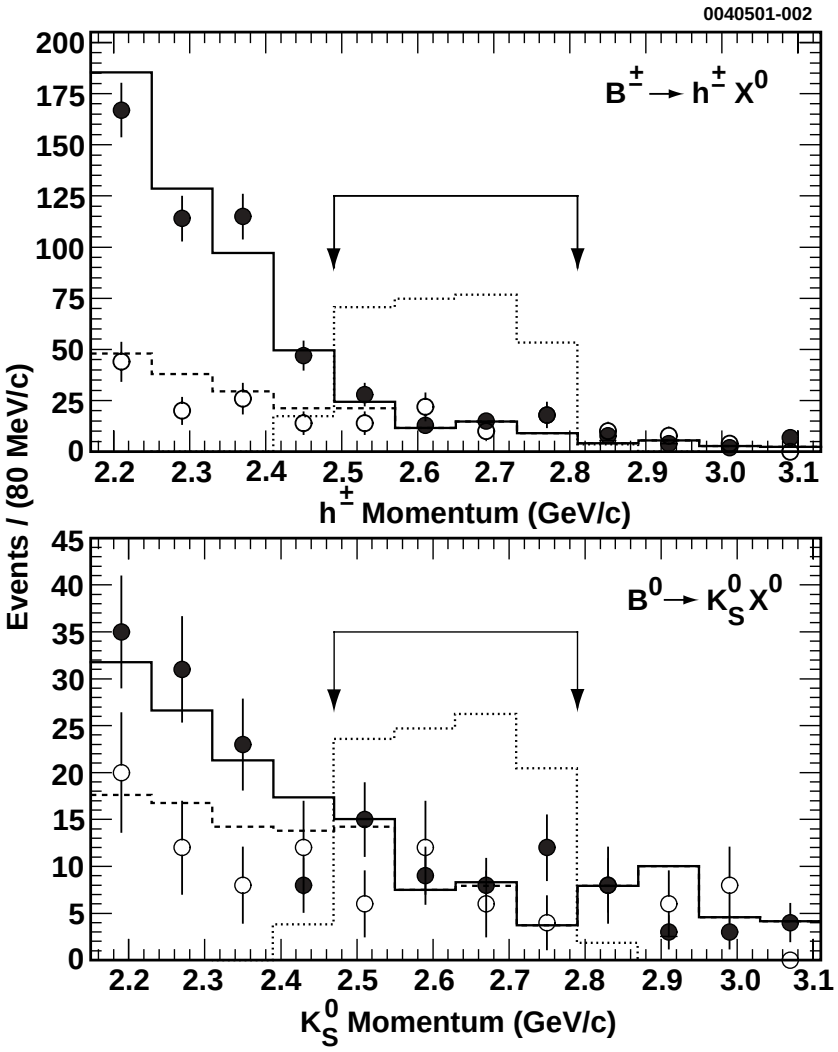

Figure V.25: Momentum distribution of the signal meson in data and MC samples.

events contributing to the yield of the charged and neutral decay mode, respectively. In most of the cases (8 out of the total 11 $B\bar{B}$ simulated events) an energetic light meson produced in the decay of a D meson coming from $B \to D\ell\nu$ semileptonic decay played the role of our signal meson that together with the accompanying neutrino having a large momentum ($p \sim 1.8 - 2.1$ GeV/c) and opposite direction to the meson could mimic our signal signature.

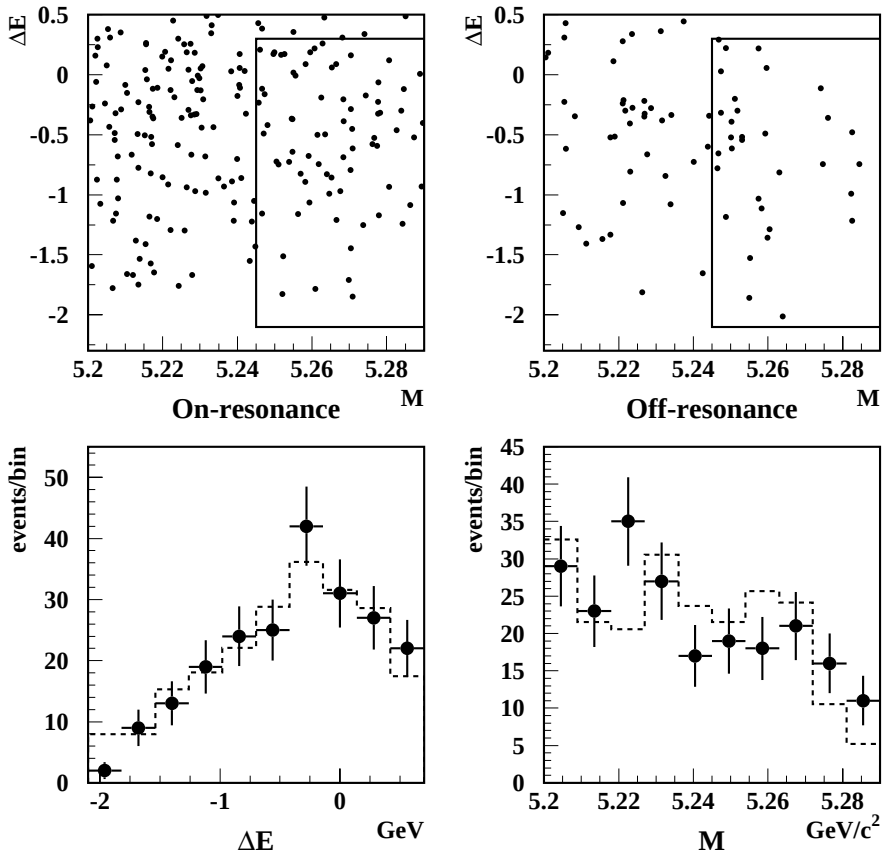

Figure V.26: Distribution of $B^{\pm} \rightarrow (\pi^{\pm}, K^{\pm})X^0$ candidate events in $M - \Delta E$ plain and one-dimensional projections.

Other B decay modes like $B \rightarrow \rho/\omega/\pi\ell\nu$ and $B \rightarrow hh$ ($h = \pi, K$) that are not simulated in the generic Monte-Carlo sample can occasionally fake our signal and contribute to the background. These decays proceed through $b \rightarrow uW$ charged current or $b \rightarrow s$ penguin mechanism, which are suppressed with respect to the $b \rightarrow cW$ diagram, and considered to be rare, however, their branching ratio can reach up to $10^{-3} - 10^{-4}$ in case of the semileptonic modes and 10^{-5} in case of the hadronic modes. In order to study the impact of these decays

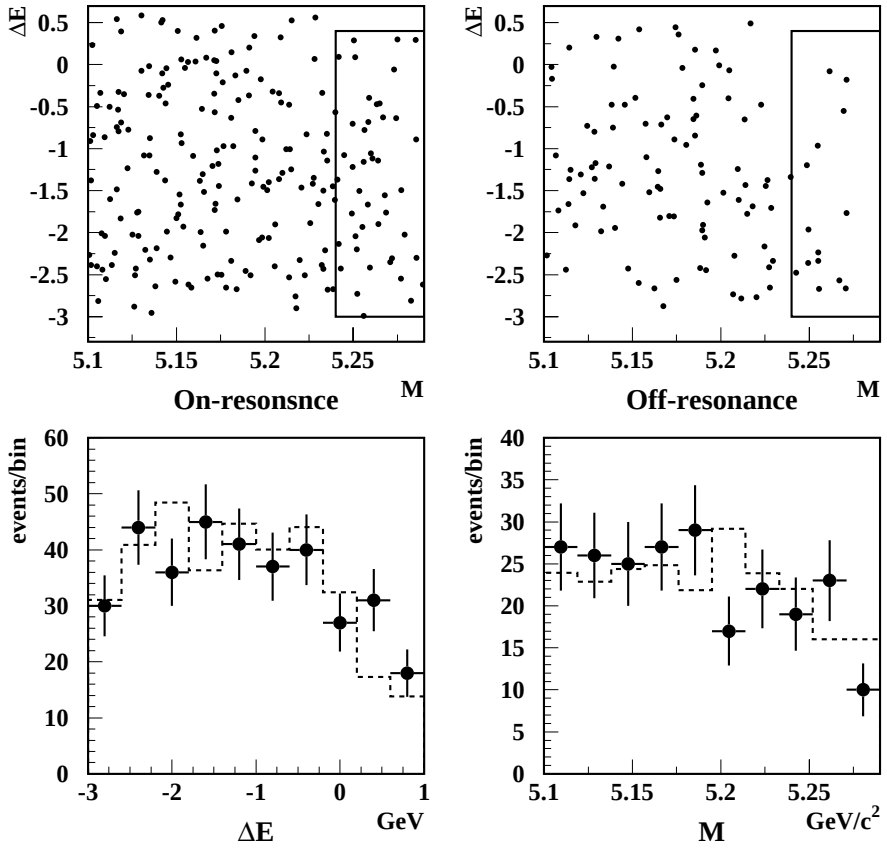

Figure V.27: Distribution of $B^{\pm} \to K^0_S X^0$ candidate events in $M - \Delta E$ plain and one-dimensional projections.

for our analysis we generated 5000 MC events to simulate several two-body final states containing $\pi\pi$ $K\pi$ and KK mesons and 10000 events leading to $B \to \pi/\rho e^+ \nu_e$ decays.

The main characteristic differences between these decays and the signal are demonstrated on the following three figures. On Fig. V.28, we can see that the signal meson candidate in semileptonic decays has a much wider distribution due to the three-body decay structure and only the high momentum tail of the distribution interferes with our signal region. Figures

V.29 and V.30 show the distribution of some of the shape variables (R_2, $\cos\Theta_{\rm thrust}$ and $\cos\Theta_{\rm empty-cone}$) as well as the kinematic variables M and ΔE for selected two-body hadronic decays and signal events. Based on these observables our analysis code is able to discriminate against these events effectively even if a neutral pion or K^0_S accompanies the energetic charged meson. However, as it is apparent on Fig. V.29, characteristics of events with a final state $h^{\pm}K^0_L$ are very close to those of the signal due to the fact that the long living K^0_L is able to escape from detection, and therefore, they can mimic our signal signature.

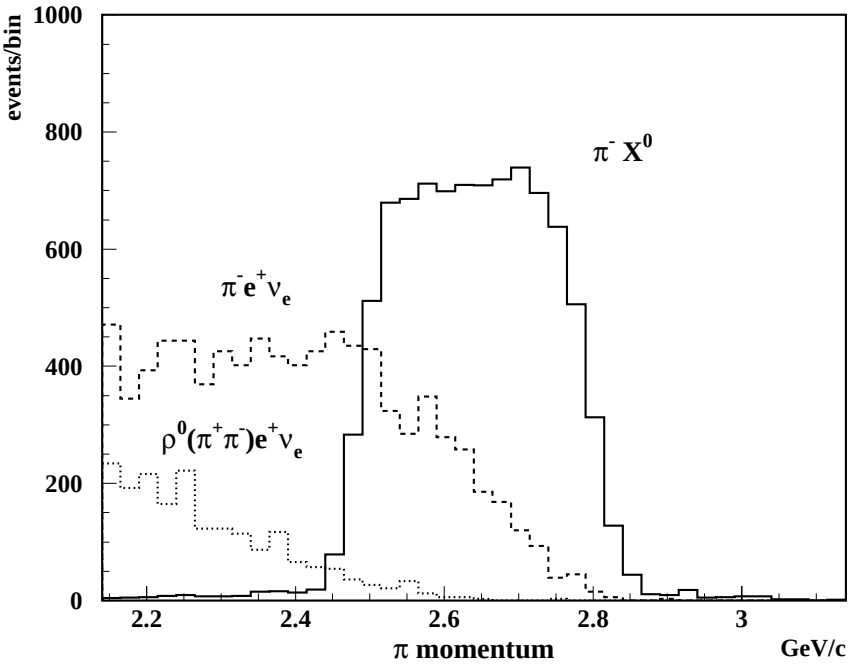

Figure V.28: Momentum distribution of the meson candidate in signal and semileptonic MC samples.

Tables V.8 and V.9 summarize the branching ratio ($\mathcal{B}$) of the different B decays together

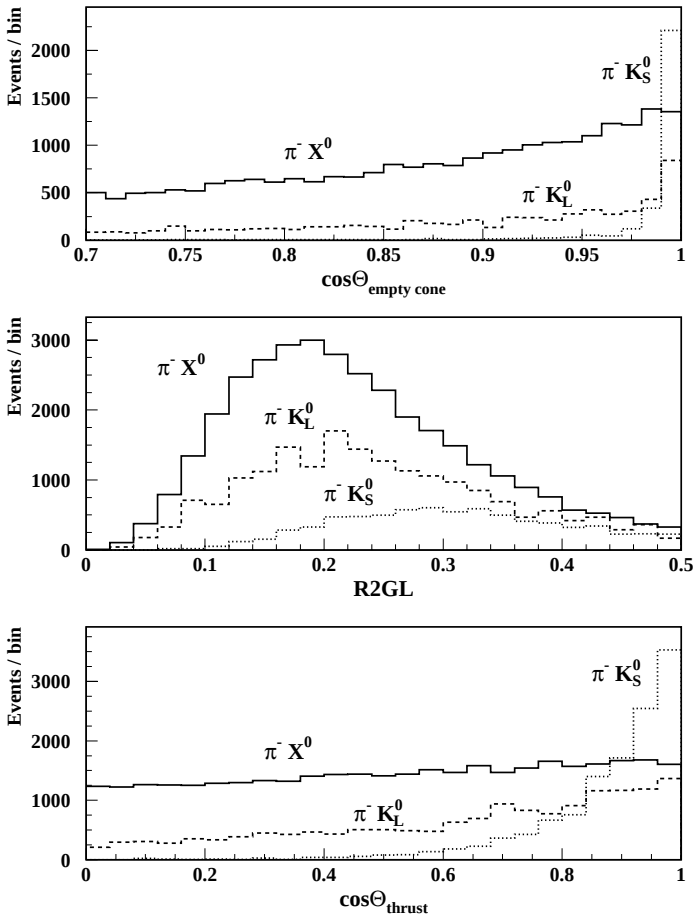

Figure V.29: Distribution of selected shape variables in signal and $B \to \pi K^0$ MC samples. Final states with the different K^0 components are plotted separately.

with the selection efficiency (ε) and the estimated contribution to the observed events. Although, this estimate is very unreliable due to the large uncertainty in the branching ratios it is evident that its contribution is at least an order of magnitude less than the continuum background. To derive a conservative upper limit on $B \to hX^0$ we neglected the background contribution due to B meson decays.

Since tau pair production ($e^+e^- \to \tau^+\tau^-$) rate is almost as high as the $B\bar{B}$ production

Table V.8: Expected contribution of different B decay modes to the observed events in the $B^{\pm} \to (\pi^{\pm}, K^{\pm})X^0$ analysis. $\mathcal{B}$ branching fractions are taken from [53, 63].

Decay mode	ε	$B_r(\times 10^{-5})$	Expected events
$b \to cW$		≈ 2.4	
$B^{\pm} \to \pi^{\pm}\pi^0$	0.16%	< 1.27	< 0.2
$B^{\pm} \to K^{\pm}\pi^0$	0.16%	$1.16^{+0.30+0.14}_{-0.27-0.13}$	< 0.3
$B^{\pm} \to \pi^{\pm}K^0$	2.2%	$1.82^{+0.46}_{-0.40} \pm 0.16$	< 5.0
$B^{\pm} \to K^{\pm}K^0$	2.2%	< 0.51	< 1.1
$B^0 \to \pi^+\pi^-$	0.04%	$0.43^{+0.16}_{-0.14} \pm 0.05$	≈ 0
$B^0 \to K^{\pm}\pi^{\mp}$	0.04%	$1.72^{+0.25}_{-0.24} \pm 0.12$	< 0.1
$B^0 \to K^+K^-$	0.04%	< 0.19	≈ 0
$B^0 \to \pi^-\ell^+\nu$	0.12%	18 ± 6	< 2.7
$B^{\pm} \to \rho^0(\pi^+\pi^-)e^{\pm}\nu$	$< 0.01\%$	< 21	≈ 0

Table V.9: Expected contribution of different B decay modes to the observed events in the $B^0 \to K^0_S X^0$ analysis. $\mathcal{B}$ branching fractions are taken from [53, 63].

Decay mode	ε	$\mathcal{B}(\times 10^{-5})$	Expected events
$b \to cW$			≈ 1.0
$B^0 \to \pi^0 K^0$	0.08%	$1.46^{+0.59+0.24}_{-0.51-0.33}$	< 0.2
$B^{\pm} \to \pi^{\pm}K^0$	$< 0.01\%$	$1.82^{+0.46}_{-0.40} \pm 0.16$	≈ 0

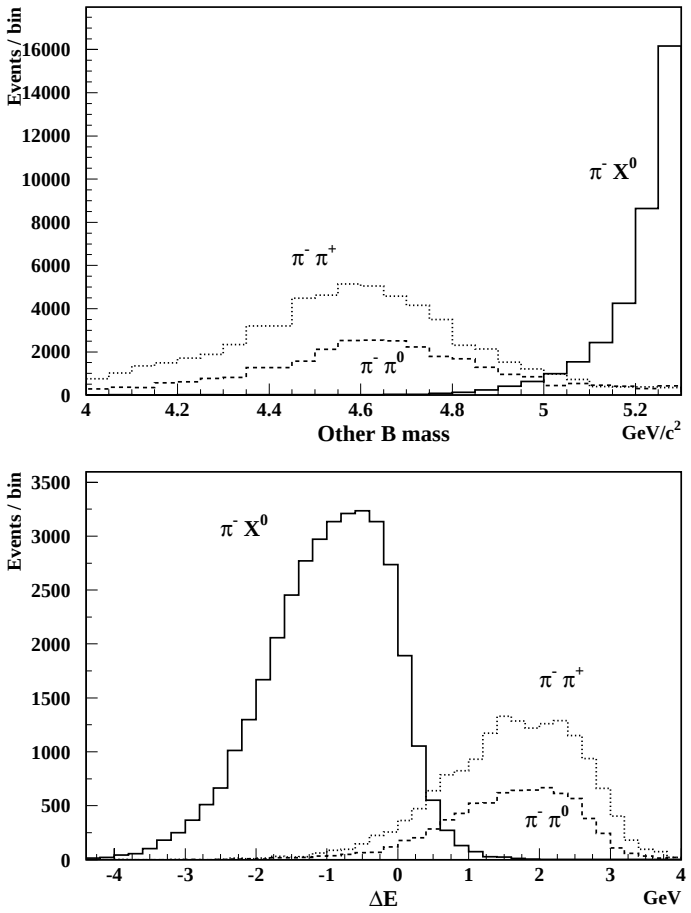

Figure V.30: Distribution of M and ΔE in signal and $B \to \pi\pi$ MC samples.

rate at the energy of the $\Upsilon(4S)$ resonance and tau leptons prefer to decay into charged meson(s) accompanied by a neutrino we also studied the background contribution from this source. We found that no events out of 12 million simulated tau MC events passed our selection criteria.

V.6 Systematic error

We determined the signal selection efficiency (ε) of our analysis using Monte-Carlo generated events. It is very important to make sure that the simulated events correctly represent the data. This is a very hard task since we lack any real signal events to which we could compare our signal MC simulation and therefore, we have to use indirect methods to quantify the uncertainty in the selection efficiency. We try to identify more or less independent sources of uncertainty and determine what variation they cause in the final efficiency and add their effects in quadrature to get the final systematic error. The different components of the systematic error and their contribution are summarized in Table V.10. The cuts on the fisher discriminant and the kinematic variables (M and ΔE) have the largest contribution to the systematic error.

Table V.10: Summary of systematic errors in the signal efficiency.

Systematic contribution	$B^{\pm} \to (\pi^{\pm}, K^{\pm})f$	$B^0 \to K_s^0 f$
Charged track(s)	1%	2%
dE/dx cut	2%	-
K_s^0 finding	-	3%
Momentum	1%	1%
M_B and ΔE	6%	6%
Fisher	11%	16%
Signal MC $1/\sqrt{N}$	1%	1%
Total	13%	18%

First, we selected hadronic events with at least three well reconstructed charged tracks and shape parameter $R_2 < 0.5$. The systematic error due to this selection is negligible compared to others and we neglect it.

We next search for a well reconstructed charged π/K track or K^0_S decaying to $\pi^+\pi^-$. Although, the track reconstruction efficiency is high, tracks can be lost for a variety of reasons such as interaction with the detector material, decay in flight, noisy/inefficient wire or confusion due to overlapping tracks. This raises the question whether the Monte Carlo simulation of the detector response reliably models these inefficiencies. Intensive studies at CLEO showed that the combined track finding and fitting efficiency is correctly reproduced by the Monte Carlo to better than 1% [64]. Therefore, we assigned a conservative 1% systematic error to each charged track that we used as a signal meson coming from the $B \to hX^0$ decay and added these errors linearly (i.e. 2% error in case of the signal $K^0_S \to \pi^+\pi^-$). Due to the dE/dx cut on the charged meson candidate and additional uncertainty in the reconstruction of the K^0_S vertex we add a 2% and 3% error in quadrature to the tracking efficiency error to arrive a total fractional uncertainty of 2.2% and 3.6% in the $\pi^\pm/K^\pm$ and K^0_S tracks, respectively.

The efficiency of the tight momentum cut on the signal meson is 91.6% and 93.9% in case of the charged and neutral decay mode, respectively. We assigned a 1% systematic error to this cut.

We next consider the error due to the selection criteria on the kinematic variables M and ΔE. If the shape of the signal in the Monte Carlo is not well modeled then we get an incorrect efficiency: a wider (narrower) peak leads to lower (higher) efficiency than the actual value. In a similar analysis that set upper limits on the leptonic decays of the B mesons $B^\pm \to \ell^\pm \nu_\ell$ ($\ell = e, \mu, \tau$) at CLEO [65] the authors searched for a single lepton and calculated the beam constrained mass $M = \sqrt{E^2_{\rm beam} - (\mathbf{p}_{\rm rest})^2}$ and energy difference $\Delta E = E_{\rm rest} - E_{\rm beam}$ from the rest of the event in a similar way as we do. They checked the shape of the M and ΔE distribution using two independent samples: the sample of fully reconstructed B tags (in

which one of the B meson decay was reconstructed) and the sample of $B \to D^* \ell \nu$ decays. In their check the reconstructed B meson played the role of the signal B, and M and ΔE were calculated from the remaining particles in the event. They compared data to the Monte Carlo simulation and concluded that the agreement is satisfactory.

Namely, they found that the average difference in the width of the ΔE distribution between the data and Monte Carlo was 8% . We could check how the yield of the signal in our Monte Carlo simulation changes if we changed the width of our ΔE distribution by 8% . This is equivalent to change the width of our cut with the same amount. We found that the yield changes by 1.9% (1.5%) in case of the charged (neutral) decay analysis. The shape of the mass distributions was compared in the same analysis [65] by taking the ratio of data and Monte Carlo distributions and fit the result with a straight line. They found the average slope to be -1.4. A change in the slope of the M distribution in our signal Monte Carlo with the same amount resulted in a 6.0% (5.6%) change in the signal yield in the charged (neutral) decay mode. We took the changes in the yields as the systematic error associated with the ΔE and M cut and add them in quadrature to arrive at a total error of 6.3% and 5.8% in case of the $B^{\pm} \to (\pi^{\pm}, K^{\pm}) X^0$ and $B^0 \to K^0_S X^0$ analysis, respectively.

We estimated the systematic error due to the uncertainty in the signal shape of the Fisher Discriminant in a similar manner. We compared the distributions resulting from off-resonance data to that from continuum Monte Carlo and adopted the same uncertainty for the signal. The change in the yield due to the appropriate change in the cut value gave the systematic error.

We fitted the Fisher distributions after all other restrictions were applied to a bifurcated

Gaussian parametrized as

$$F(x) = N \begin{cases} \exp\left(-\frac{(x-x_0)^2}{2\sigma_L^2}\right) & \text{if } (x < x_0) \\ \exp\left(-\frac{(x-x_0)^2}{2\sigma_R^2}\right) & \text{if } (x > x_0) \end{cases} . \quad \text{(V.24)}$$

The fitted parameters such as the center of the distribution (x_0), the left and right side standard deviations (σ_L, σ_R) are given in Table V.11. The results of the fits are displayed on Fig. V.31 for off-resonance data (top), continuum (middle) and signal (bottom) Monte Carlo. The agreement between the off-resonance data and the continuum ($q\bar{q}$) Monte Carlo

Table V.11: Fisher Discriminant fit results.

		Off-res. Data	$q\bar{q}$ MC	Signal MC
$B^{\pm} \to (\pi^{\pm}, K^{\pm})f$	x_0	0.679 ± 0.003	0.679 ± 0.001	0.333 ± 0.001
	σ_L	0.145 ± 0.002	0.141 ± 0.001	0.089 ± 0.001
	σ_R	0.075 ± 0.002	0.076 ± 0.001	0.162 ± 0.001
$B^0 \to K_s^0 f$	x_0	0.630 ± 0.011	0.636 ± 0.004	0.345 ± 0.002
	σ_L	0.131 ± 0.007	0.134 ± 0.002	0.093 ± 0.001
	σ_R	0.100 ± 0.007	0.096 ± 0.002	0.155 ± 0.001

is excellent. The fractional difference in the center of the distributions between data and MC is less than 1% for both decay modes. To be conservative we assumed a 2% error as the uncertainty in the center of the signal distribution when we calculated the change in the yield. The quadrature sum of the fractional differences in the standard deviations of the distributions is 3.1% and 4.7% in case of the charged and neutral decay mode, respectively. We assigned twice as much error to standard deviation of the signal distribution.

Instead of shifting the distribution or changing its shape with the required amount we simply moved the cut value with the appropriate absolute amount to calculate the change in the signal yield and we add the resulting fractional differences in quadrature to get the total

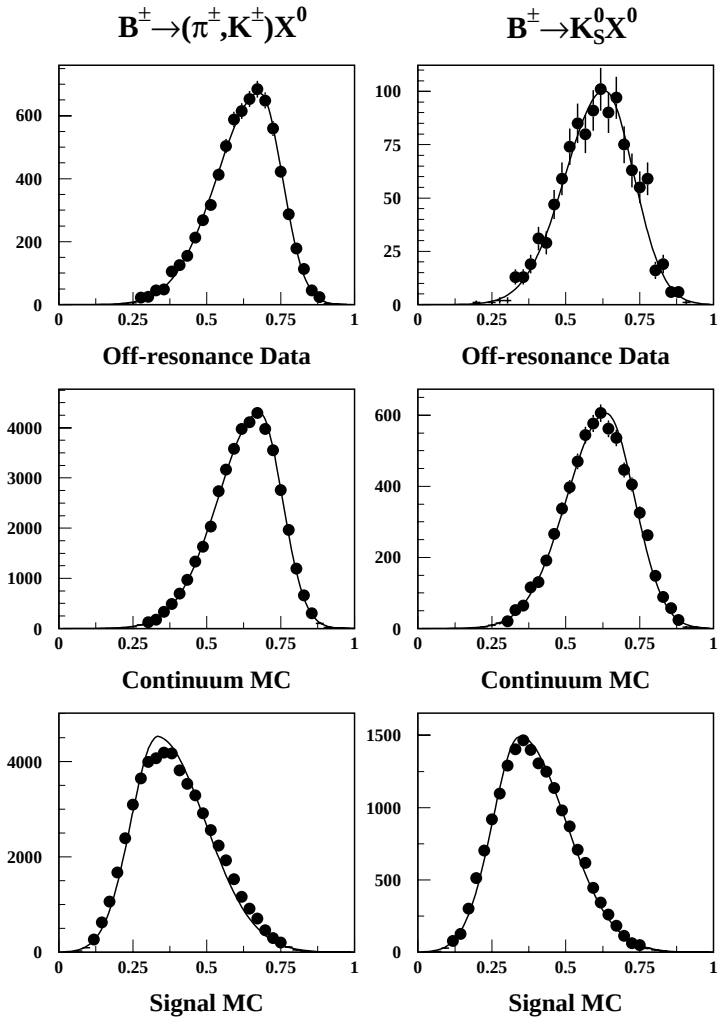

Figure V.31: Fit to the Fisher ($\mathcal{F}$) distributions.

change. The yield changed by 6.8% (9.1%) in case of the charged (neutral) decay mode due to the shift of the cut with an amount equivalent to the error of the central values of the distributions. Since we cut only one side of the Fisher distribution therefore we shifted the cut value with half of the amount corresponding to the error on the total sigma ($\sigma_L + \sigma_R$). This shift resulted in 9.0% (13.2%) change in the yield of the charged (neutral) decay. The total change that we associated with the error of the Fisher selection is 11.3% and 16.0% .

Finally, the limited signal Monte Carlo statistics of the signal samples contributes to the error with 0.9% and 1.3% for the neutral B and charged B decay channels, respectively.

The total systematic error in the efficiency is 13.2% and 17.5% for the $B^{\pm} \to (\pi^{\pm}, K^{\pm})X^0$ and $B^0 \to K^0_S X^0$ channels, respectively.

V.7 Upper limit on the branching ratio

We calculate the branching ratio based on the formula

$$B = \frac{N_{\rm on} - RN_{\rm off}}{\varepsilon N_B}, \tag{V.25}$$

where $N_{\rm on}$ and $N_{\rm off}$ are the observed events in the signal region in the on-resonance and off-resonance data samples, respectively, R is the normalization coefficient between the on-resonance and off-resonance samples, ε is the signal selection efficiency and N_B is the total number of charged and neutral B mesons in the data sample.

We assumed equal production of charged and neutral B meson pairs from the decay $\Upsilon(4S) \to B\bar{B}$ and we did not assign an error to this assumption. This is consistent with a recent measurement of the production ratio $f_{+-}/f_{00} = 1.04 \pm 0.07(\text{stat}) \pm 0.04(\text{syst})$ published by the CLEO Collaboration [66]. Hence, the total number of charged (neutral) B mesons in the denominator of the above equation is equal to the number of the $B\bar{B}$ pairs in our data sample $N_B = (9.7 \pm 0.2) \times 10^6$ and we assigned the same error to N_B that is associated with the error in the number of B meson pairs (see Section IV.2).

As we saw in Section IV.2 the statistical normalization of the off-resonance sample to the on-resonance one is consistent with 2.0 and the error is estimated to be 2% .

When we calculated the branching ratio we took into account these errors besides the statistical error ($\sqrt{N}$) in the number of observed events and the systematic error in the signal

selection efficiency (ε). The resulting central values are

$$\mathcal{B}(B^{\pm} \to (\pi^{\pm}, K^{\pm})X^0) = (1.4 \pm 2.1) \times 10^{-5} \tag{V.26}$$

$$\mathcal{B}(B^0 \to K^0_S X^0) = (2.5 \pm 1.7) \times 10^{-5} \tag{V.27}$$

The error in the branching ratio is dominated by the statistical uncertainty in $N_{\rm on}$ and $N_{\rm off}$.

In order to derive a 90% confidence level upper limit on the branching ratio we used the unified frequentist approach proposed by Feldman and Cousins [67] and adopted by the Particle data Group [53]. This method is the generalization of the classical confidence belt construction so that it yields intervals that automatically switch over from upper limits to two-sided intervals as the signal becomes more statistically significant. We applied the method recommended for the branching ratio with Gaussian error, when $\mathcal{B}$ is physically bounded to non-negative values. The resulting upper limits are

$$\mathcal{B}(B^{\pm} \to (\pi^{\pm}, K^{\pm})X^0) < 4.9 \times 10^{-5} \tag{V.28}$$

$$\mathcal{B}(B^0 \to K^0_S X^0) < 5.3 \times 10^{-5} \tag{V.29}$$

These limits constrain new physics leading to two-body B meson decays involving any massless neutral weakly-interacting particle X^0.

V.8 Constraint on the Family Symmetry Breaking Scale $F^V_{bs(d)}$

We can apply the above upper limits to the case when X^0 is a familon to obtain a lower bound on the family symmetry breaking scale (F) normalized by the generators of the symmetry group (T_{ij}) and with the relative strength of the vector coupling (g_V):

$$F^V_{\rm bd(s)} = \frac{F}{g_V T_{bd(s)}}. \tag{V.30}$$

This quantity is related to the partial decay rate Γ_f (and branching fraction) by the formula (see Section II.5)

$$F^V_{bd(s)} = \left[\frac{M_B^3}{16\pi}\beta^3\frac{|\ F_1(0)\ |^2}{\Gamma_f}\right]^{1/2} = \left[\frac{M_B^3}{16\pi}\ |\ F_1(0)\ |^2\ \frac{\tau_B}{\mathcal{B}}\right]^{1/2}, \tag{V.31}$$

where τ_B is the lifetime of the B meson (see Table V.1) and we substituted for $\beta^3 = (1 - m^2_{\pi/K}/M^2_B)^3 \approx 1$. We choose the value of the form factor to be $F_1(0) = 0.25$ that gives the most conservative lower limit on the family symmetry breaking scale.

The limit on the B^0 decay to K^0_S together with the fact that $\mathcal{B}(B^0 \to K^0 f) = 2\mathcal{B}(B^0 \to K^0_S f)$ gives a a constraint

$$F^V_{bs} > 6.4 \times 10^7 \text{GeV}. \tag{V.32}$$

If we assume that the familon couples to the d and s quark with the same strength (i.e. $F^V_{bs} = F^V_{bd}$) then $\mathcal{B}(B \to \pi f) = \mathcal{B}(B \to K f) = \frac{1}{2}\mathcal{B}(B \to (\pi, K) f)$ and our upper limit on the charged decay mode gives a little bit higher bound

$$F^V_{bd(s)} > 1.3 \times 10^8 \text{GeV}. \tag{V.33}$$

CONCLUSION

A tremendous effort has been devoted to find the deep physical reason for the existence of the mass hierarchy and weak mixing among the quarks and leptons. Despite the enormous amount of data accumulated during the past three decades we still appear to be far from the true understanding of the family structure of fermions and the origin of particle generations (families).

A possible explanation based on a spontaneously broken continuous global family symmetry was suggested by Reiss [29] and Wilczek [27]. One of the most important consequence of the spontaneous breakdown of this family symmetry is the existence of neutral massless Nambu-Goldstone bosons, called familons. Familons can have flavor-conserving as well as flavor-changing couplings with the fermions and the coupling strength is suppressed by the energy scale at which the flavor symmetry is broken. In contrast to the first two generations, experimental constraints on familons coupled to the third generation of fermions are quite modest, the only weak constraint is in the leptonic sector from $\tau^- \to \ell^- X^0$ ($\ell = e, \mu$) decay.

Familons associated with a broken family symmetry are also motivated by cosmological scenarios, such as big-bang nucleosynthesis and large scale structure formation, with a tau neutrino decaying to a lighter neutrino and a massless boson.

Flavor-changing couplings between the b quark and the familon (f) would lead to the decay $B \to hf$ ($h = \pi, K$) through vector coupling and $B \to Vf$ ($V = \rho, K^*$) through axial coupling. We have searched for the two-body decay of the B meson to a light pseudoscalar meson $h = \pi^\pm, K^\pm, K^0_S$ and a massless neutral weakly-interacting particle X^0 such as the familon. We find no significant signal by analyzing a data sample containing 9.7 million $B\bar{B}$ mesons collected with the CLEO detector at the Cornell Electron Storage Ring, and set a

90% C.L. upper limit of 4.9×10^{-5} and 5.3×10^{-5} on the branching fraction for the decays $B^{\pm} \to h^{\pm} X^0$ and $B^0 \to K_S^0 X^0$, respectively. These upper limits correspond to a lower bound of approximately 10^8 GeV on the family symmetry breaking scale (with vector coupling) for the third generation of quarks.

The results of this analysis was submitted to and accepted by the Physical Review Letters for publication [68]. In addition, preliminary results were presented at the APS April Meeting 2000 [69].

Appendix A

PROOF OF THE GOLDSTONE THEOREM

In this appendix we give a general proof of the Goldstone Theorem (Section I.4) for the case of classical scalar fields using the same arguments as in Chapter 11 of [48]. Three other proof can be found in [70].

We start with the Lagrangian of a theory involving several scalar fields $\phi^i(x)$

$$\mathcal{L} = \frac{1}{2}\sum_i (\partial_\mu \phi^i)^2 - V(\phi^i). \tag{A.1}$$

The lowest energy configuration is a set of constant fields $\phi^i(x) = \phi_0^i$ that minimizes the potential $V(\phi^i)$:

$$\left.\frac{\partial V}{\partial \phi^i}\right|_{\phi_0^i} = 0. \tag{A.2}$$

The small oscillations around this lowest energy configuration can be parametrized by $\phi^i(x) = \phi_0^i + \chi^i(x)$. Then, the potential $V(\phi^i)$ can be expressed in terms of the shifted fields χ^i as

$$V(\phi^i) = V(\phi_0^i) + \frac{1}{2}\sum_i \sum_j \left(\frac{\partial^2 V}{\partial \phi^i \partial \phi^j}\right)_{\phi_0} \chi^i \chi^j + ... \tag{A.3}$$

and the Lagrangian reads

$$\mathcal{L} = \frac{1}{2}\sum_i (\partial_\mu \chi^i)^2 - \frac{1}{2}\sum_i \sum_j \left(\frac{\partial^2 V}{\partial \phi^i \partial \phi^j}\right)_{\phi_0} \chi^i \chi^j + O(\chi^3) \tag{A.4}$$

plus an irrelevant constant. From this form we can see that the symmetric positive semi-definite matrix

$$\left(\frac{\partial^2 V}{\partial \phi^i \partial \phi^j}\right)_{\phi_0} = m_{ij}^2 \tag{A.5}$$

in the quadratic term is the mass matrix, whose eigenvalues give the masses for the fields χ^i. We can show that, every continuous symmetry of the Lagrangian that is not a symmetry of the vacuum (ϕ_0^i) gives rise to a zero eigenvalue of the above mass matrix, that is, the corresponding field is a massless excitation.

A general continuous symmetry transformation of the ϕ^i fields can be expressed as $\phi^i \rightarrow \phi^i + \Theta\mathcal{F}^i(\phi)$, where $\mathcal{F}^i(\phi)$ is an arbitrary functional of the fields and Θ is an infinitesimal parameter. If we restrict the fields to be constant fields, then the kinetic (derivative) terms in the Lagrangian given by Eq. A.1 vanish and the invariance of the Lagrangian under the transformation requires

$$V(\phi^i) = V\left(\phi^i + \Theta\mathcal{F}^i(\phi)\right) \approx V(\phi^i) + \Theta\sum_i \mathcal{F}^i(\phi)\frac{\partial V}{\partial \phi^i}, \tag{A.6}$$

that is,

$$\sum_i \mathcal{F}^i(\phi)\frac{\partial V}{\partial \phi^i} = 0. \tag{A.7}$$

If we differentiate this equation with respect to ϕ^j and set $\phi = \phi_0$ then we obtain

$$\sum_i \left(\frac{\partial \mathcal{F}^i(\phi)}{\partial \phi^j}\right)_{\phi_0}\left(\frac{\partial V}{\partial \phi^i}\right)_{\phi_0} + \sum_i \mathcal{F}^i(\phi_0)\left(\frac{\partial^2 V}{\partial \phi^j \partial \phi^i}\right)_{\phi_0} = 0. \tag{A.8}$$

The first term is zero since the V potential has a minimum at $\phi = \phi_0$ (see Eq. A.2). Therefore, the second term must be zero as well:

$$\sum_i \left(\frac{\partial^2 V}{\partial \phi^j \partial \phi^i}\right)_{\phi_0} \mathcal{F}^i(\phi_0) = 0. \tag{A.9}$$

This is trivial if $\mathcal{F}^i(\phi_0) = 0$, $\forall i$, that is, for transformations that leave the vacuum unchanged: $\phi_0^i \rightarrow \phi_0^i + \Theta\mathcal{F}^i(\phi_0) = \phi_0^i$, $\forall i$. On the other hand, if $\mathcal{F}^i(\phi_0)$ is not a zero-vector, that is, the transformation is not a symmetry of the vacuum (ϕ_0), then the vector $\mathcal{F}^i(\phi_0)$ is a non-trivial eigenvector of the mass matrix with zero eigenvalue. QED.

Appendix B

STUDY OF THE DECAYS $B \to \tau\nu_\tau$ AND $B \to K\nu\bar{\nu}$

The decays $B^\pm \to \tau^\pm\nu_\tau$ followed by a subsequent decay of the tau-lepton to $\pi^\pm\nu_\tau$ and $B^\pm \to K^\pm\nu\bar{\nu}$ have a very similar experimental signature: a charged meson, π or K respectively, is accompanied by two invisible neutrinos. Our original analysis aimed to search for the decay $B^\pm \to h^\pm X^0$ is somewhat sensitive to both of these decay modes since the neutrinos are invisible for the detector and we did not make an attempt to separate π and K signal mesons from each other. However, the signal selection efficiency of our selection criteria for these decay modes is much smaller since the light meson has a much wider momentum distribution in contrast to the case of the two-body decay $B^\pm \to h^\pm X^0$ (see Fig. B.3), and therefore, the strict momentum cut on the signal meson eliminates a large portion of these events.

The purely leptonic decays of charged mesons to lepton plus its neutrino such as the $B^\pm \to \tau^\pm\nu_\tau$ decay provide a unique opportunity to study the weak decay process in a clean environment without the effect of strong interactions in the final state. In the Standard Model, the leptonic decays proceed primarily through the annihilation of the constituent quarks of the meson into a virtual $W^\pm$ boson as it is schematically shown on Fig. B.1. The branching ratio of the $B^\pm \to \ell^\pm\nu_\ell$ ($\ell = e, \mu, \tau$) decay has a simple dependence on the B meson decay constant f_B, which parameterizes the overlap of the quark wavefunctions in the meson, and the CKM matrix element V_{ub}. Both f_B and V_{ub} are the subject of considerable experimental and theoretical effort, but are currently known with an accuracy of only $20 - 30\%$. If V_{ub} is obtained from other measurements, than the precise measurement of the

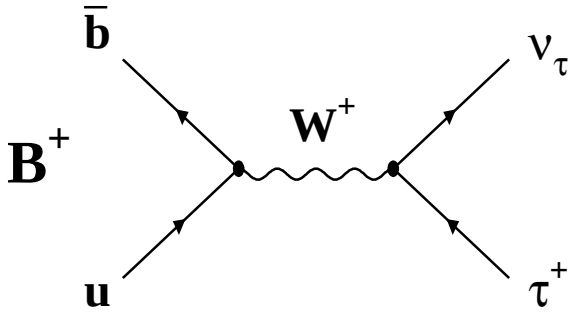

Figure B.1: Feynmann graph for $B^+ \to \tau^+\nu_\tau$ decay.

$B \to \ell\nu_\ell$ branching ratio may be the only way to determine the decay constant f_B with small theoretical uncertainty.

However, the expected value of $\mathcal{B}(B \to \tau\nu_\tau)$ is very small, in the range $(1-10)\times 10^{-5}$, and the branching ratio of the decay to μ and e are even smaller by two and seven orders of magnitude, respectively, because of the enhanced helicity suppression due to the lightness of these leptons[1]. Therefore, with the current experimental technique the $B \to \tau\nu_\tau$ decay can be the only accessible purely leptonic decay despite of that the $B \to \mu/e\nu$ decays have much less background and higher reconstruction efficiency[2].

On the other hand, the decay $B \to \tau\nu_\tau$ could proceed through annihilation of the constituent quarks into a Higgs boson according to the Type II two Higgs doublet model, in which the u- and d-type quarks acquire their masses from the interaction with two separate

[1]Since the B meson is a spin-zero particle the leptons emerging from its decay must have anti-parallel spins to conserve angular momentum. However, the (anti-)neutrinos has only one, left- (right-) handed, helicity state available, therefore, the charged (anti-)lepton is forced to an unfavorable right- (left-) handed helicity state. The unfavored helicity state is suppressed by a factor proportional to m^2/M_B^2.

[2]The modification of the analysis of the latter decay modes by adding a hard gamma photon to the final state [71] can also be used to get experimental information on f_B. According to theoretical calculations, the branching ratio of the decays $B \to \ell\nu\gamma$ ($\ell = e, \mu$) can reach 5×10^{-6} [72] since helicity suppression does not occur when the spin-0 B meson becomes a spin-1 B meson via emitting a γ photon before annihilation into $\ell + \nu$ [73].

Higgs-fields [74]. Such a mechanism could enhance the decay rate significantly. Therefore, experimental bounds on the the $B \to \tau\nu_\tau$ branching ratio could probe physics beyond the Standard Model as well.

Currently, the best upper limit on $\mathcal{B}(B^\pm \to \tau^\pm\nu_\tau)$ comes from three measurements in the $Z^0 \to b\bar{b}$ system ranging from $(5.7-16)\times 10^{-4}$ [75]. CLEO recently published a search using full event reconstruction in the $\Upsilon(4S) \to B\bar{B}$ system, which resulted in a 90% confidence level upper limit of 8.4×10^{-4} [76].

The decay $B^\pm \to K^\pm\nu\bar{\nu}$ proceeds through the flavor changing neutral current induced $b \to s\nu\bar{\nu}$ decay governed by a single left handed operator obtained from Z^0 electroweak penguin and box diagrams (Fig. B.2), where the dominant contribution corresponds to a top quark intermediate state. This makes the decay very sensitive for possible new physics since

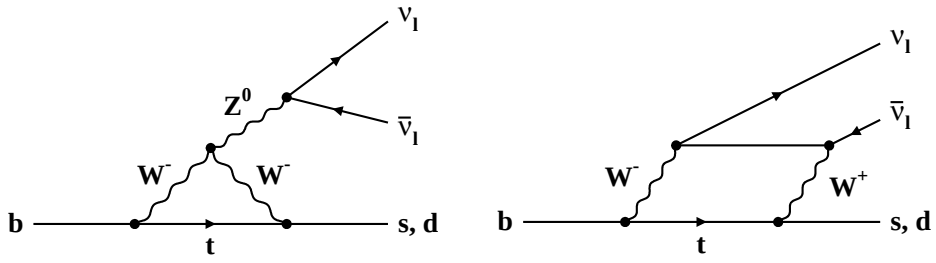

Figure B.2: Electroweak penguin (left) and box (right) mechanism for $b \to s(d)\nu\bar{\nu}$ decay.

their contribution can be manifested only in the modification of this operator or introducing a new right handed operator. The expected rate for $b \to s\nu\bar{\nu}$ is an order of magnitude lower than for $b \to s\gamma$, which is predicted to be $(3.5 \pm 0.3) \times 10^{-4}$. Experimental limits on the inclusive $b \to s\nu\bar{\nu}$ was set by ALEPH ($< 7.7 \times 10^{-4}$) [46], while limit on the exclusive $B \to K^*\nu\bar{\nu}$ ($< 1.0 \times 10^{-3}$) and $B \to K\nu\bar{\nu}$ ($< 2.4 \times 10^{-4}$) were measured by DELPHI [77]

and CLEO [76], respectively.

We estimate the selection efficiency of our analysis for the $B^{\pm} \to \tau^{\pm}(\pi^{\pm}\nu)\nu$ and $B^{\pm} \to K^{\pm}\nu\bar{\nu}$ events by using simulated Monte Carlo events. We generated $90,000$ $\Upsilon(4S) \to B^{+}B^{-}$ events in which one of the B meson was forced to decay to $K\nu\bar{\nu}$ with all the three neutrino flavors being equally represented, while the other B was allowed to decay generically. Half of the sample was generated with the B^{+} decaying to the signal mode, and the other half simulated the B^{-} decay. We used 3-body phase space and a constant matrix element in the event generator since it gives essentially the same result (see [76]) as the matrix elements defined in Ref. [52]. In case of the $B \to \tau\nu_{\tau}$ analysis, $45,000$ events were generated in the decay chain $\Upsilon(4S) \to B^{+}B^{-}$, followed by $B^{-} \to \tau^{-}\bar{\nu}_{\tau}$, and followed by $\tau^{-} \to \pi^{-}\nu_{\tau}$. In both cases, 1/3 (2/3) of the events were generated by using parameters corresponding to the CLEO II (CLEO II.V) detector and they were distributed appropriately over the various running conditions.

However, there is a small kinematic difference between the two decays, which is apparent on the momentum distribution of the daughter mesons on Fig. B.3. Due to angular momentum conservation and the fact that the (anti-)neutrino has only left- (right-) handed helicity state available, the τ^{-} (τ^{+}) from the $B \to \tau\nu_{\tau}$ decay is fully polarized with its spin pointing along (opposite) its momentum. In the subsequent decay $\tau \to \pi\nu_{\tau}$ the neutrino prefers to be emitted with its spin aligned with the tau spin in the τ's rest frame because the pion has zero spin. As a result, the neutrino tends to be emitted in opposite to the tau direction and the pion gets most of the boost from the tau momentum [78]. Therefore, the pion from $B \to \tau(\pi\nu_{\tau})\nu_{\tau}$ decay tends to have larger momentum than the kaon from the $B \to K\nu\bar{\nu}$ decay where no such a polarized intermediate state occurs. We generated the tau's in the correct polarization state during the MC simulation.

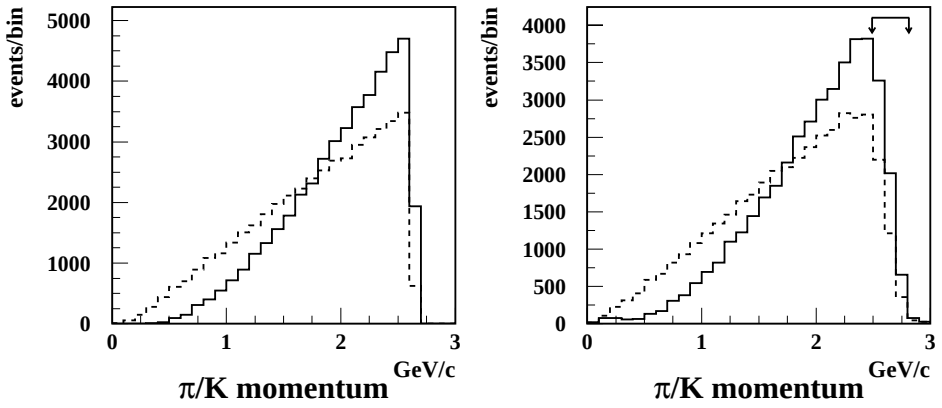

Figure B.3: Momentum distribution of the mesons in $B \to \tau(\pi\nu)\nu$ (solid) and $B \to K\nu\bar{\nu}$ (dashed) decays. The plot on the left shows the distribution in the rest frame of the B meson while the plot on the right show the distributions in the lab frame. The sharp cutoff at 2.64 GeV/c on the left is smeared by the motion of the B ($p_B = 0.34$ GeV/c) on the right. The arrows on the right plot indicate the accepted momentum region.

The selection efficiency of our $B^{\pm} \to h^{\pm}X^0$ analysis for $B \to \tau(\pi\nu_\tau)\nu_\tau$ and $B \to K\nu\bar{\nu}$ events is 1.2% and 0.8% , respectively. We assigned the same systematic error to the components of the efficiency as in the $B^{\pm} \to h^{\pm}X^0$ analysis except for that the uncertainty due to the finite MC sample is higher, 4% , resulting in a 14% overall uncertainty in the efficiency. The branching ratio was calculated by the formula

$$\mathcal{B} = \frac{N_{\rm on} - RN_{\rm off}}{\varepsilon N_B}, \tag{B.1}$$

but in case of the $B \to \tau\nu$ mode we multiplied the denominator with an extra factor of 0.118, the relative branching fraction of the $\tau \to \pi\nu$ decay [53], which has not been taken into account in the MC simulation of the decay chain. Using the number of observed events $N_{\rm on} = 74 \pm 8.6$ and $N_{\rm off} = 32 \pm 5.7$ along with $R = 2.0 \pm 0.04$ and $N_B = (9.7 \pm 0.2) \times 10^6$,

the central values of the branching ratio are

$$\mathcal{B}(B \to K\nu\bar{\nu}) = (1.3 \pm 1.8) \times 10^{-4}, \tag{B.2}$$

$$\mathcal{B}(B \to \tau\nu_\tau) = (0.73 \pm 1.04) \times 10^{-3}. \tag{B.3}$$

The upper limits at 90% confidence level are determined by the unified frequentist approach for Gaussian distributed data close to a physical boundary [67, 53]:

$$\mathcal{B}(B \to K\nu\bar{\nu}) < 4.3 \times 10^{-4} \tag{B.4}$$

and

$$\mathcal{B}(B \to \tau\nu_\tau) < 3.2 \times 10^{-3}. \tag{B.5}$$

[1] D. Griffiths, *Introduction to elementary particles*, John Wiley & Sons, 1987; F. Halzen and A. D. Martin, *Quarks and leptons: An introductory course in modern particle physics*, John Wiley & Sons, New York, 1984; D. H. Perkins, *Introduction to high energy physics*, Addison Wesley Publ., 1987.

[2] Super-Kamiokande Collaboration, Y. Fukuda *et al.*, Phys. Rev. Lett. **81**, 1562 (1998).

[3] SNO Collaboration, Q. R. Ahmad *et al.*, Phys. Rev. Lett. **87**, 071301 (2001).

[4] LEP Collaboration, Phys. Lett. B **276**, 247 (1992).

[5] K. A. Olive, Phys. Rep. **190**, 307 (1990).

[6] D. Karlen, "*Experimental status of the standard model*", Prepared for 29th International Conference on High-Energy Physics (ICHEP 98), Vancouver, British Columbia, Canada, 23-29 Jul 1998.

[7] M. Schmelling, "*Status of the strong coupling constant*", hep-ex/9701002. Talk presented at the 28th International Conference on High-energy Physics (ICHEP 96), Warsaw, Poland, 25-31 Jul 1996. Published in ICHEP 96:91-102.

[8] D. Abbaneo *et al.*, LEP Eloctroweak Working Group, "*A combination of preliminary electroweak measurements and constraints on the standard model*", Preprint CERN-PPE/96-183 (1996).

[9] C. Quigg, *Gauge theories of the strong, weak and electromagnetic interactions*, Benjamin-Cummings Publ. Comp Inc., 1983; T. P. Cheng and L. F. Li, *Gauge theory of elementary particle physics*, Oxford Univ. Press, 1991.

[10] M. Gell-Mann and Y. Neeman, *The eightfold way*, W. A. Benjamin Inc., New York, NY, 1964.

[11] S. L. Glashow, Nucl. Phys. **22**, 579 (1961).

[12] D. Gross and F. Wilczek, Phys. Rev. D **8**, 3633 (1973); S. Weinberg, Phys. Rev. Lett. **31**, 494 (1973); H. Fritzsch, M. Gell-Mann, and H. Leutwyler, Phys. Lett. B **47**, 365 (1973).

[13] S. Weinberg, Phys. Rev. Lett. **19**, 1264 (1967); A. Salam, in *Elementary particle physics* (Nobel Symp. N.8), Ed. N. Svartholm, Almqvist and Wiksells, Stockholm 1968, p.637.

[14] S. Glashow, J. Iliopoulos, and L. Maiani, Phys. Rev. D **2**, 1285 (1970).

[15] V. L. Ginzburg and L. D. Landau, J. Exp. Theoret. Phys. USSR **20**, 1064 (1950).

[16] Y. Nambu, Phys. Rev. Lett. **4**, 380 (1960); J. Goldstone, Nuovo Cimento **19**, 154 (1961).

[17] P. W. Higgs, Phys. Lett. **12**, 132 (1964); F. Englert and R. Brout, Phys. Rev. Lett. **13**, 321 (1964); G. S. Guralnik, C. R. Hagen, and I. W. B. Kibble, Phys. Rev. Lett. **13**, 585 (1964); P. W. Higgs, Phys. Rev. **145**, 1156 (1966); T. W. B. Kibble, Phys. Rev. **155**, 1554 (1967).

[18] G. Arnison *et al.*, UA1 Collaboration, Phys. Lett. B **122**, 103 (1983); M. Banner *et al.*, UA2 Collaboration, Phys. Lett. B **122**, 476 (1983).

[19] R. Barate *et al.*, ALEPH Collaboration, CERN-EP/2000-138, submitted to Phys. Lett. B; hep-ex/0011045.

[20] M. Kobayashi and T. Maskawa, Prog. Theor. Phys. **49**, 652 (1973).

[21] N. Cabibbo, Phys. Rev. Lett. **10**, 531 (1963).

[22] BaBar Collaboration, B. Aubert *et al*, Phys. Rev. Lett. **87**, 091801 (2001); Belle Collaboration, K. Abe *et al*, Phys. Rev. Lett. **87**, 091802 (2001).

[23] L. Wolfenstein, Phys. Rev. Lett. **51**, 1945 (1983).

[24] H. Georgi and S. Glashow, Phys. Rev. Lett. **32**, 438 (1974).

[25] H. Georgi, in *Particles and fields - 1974*, Ed. C. Carlson, AIP Press, New York 1975.

[26] M. Gell-Mann, P. Ramond, and R. Slansky, in *Supergravity*, Eds. P. van Neiuwenhuisen and D. Freedman, North Holland, Amsterdam 1979, p. 315; T. Yanagida, *Proc. of the workshop on unified theory and baryon numbers in the universe*, Eds. O. Sawada and A. Sugamoto, KEK 1979.

[27] F. Wilczek, Phys. Rev. Lett. **49**, 1549 (1982).

[28] G. B. Gelmini, S. Nussinov, and T. Yanagida, Nucl. Phys. **B219**, 31 (1983)

[29] D. B. Reiss, Phys. Lett. B **115**, 217 (1982).

[30] Y. Chikashige, R. N. Mohapatra, and R. D. Peccei, Phys. Lett. B **98**, 265 (1981); G. B. Gelmini and M. Roncadelli, Phys. Lett. B **99**, 411 (1981); C. S. Aulakh and R. N. Mohapatra, Phys. Lett. B **119**, 136 (1982).

[31] R. D. Peccei, hep-ph/9606475.

[32] R. D. Peccei and H. R. Quinn, Phys. Rev. Lett. **38**, 1440 (1977); Phys. Rev. D **16**, 1791 (1977).

[33] S. Weinberg, Phys. Rev. Lett. **40**, 223 (1978); F. Wilczek, Phys. Rev. Lett. **40**, 271 (1978).

[34] D. Chang and G. Senjanović, Phys. Lett. B **188**, 231 (1987).

[35] S. Hannestad, Phys. Rev. D **57**, 2213 (1998), and references therein.

[36] D. A. Dicus, E. W. Kolb and V. Teplitz, Phys. Rev. Lett. **39**, 168 (1977); M. Fukugita and T. Yanagida, Phys. Lett. B **144**, 386 (1984); G. Gelmini, Phys. Lett. B **146**, 311 (1984); M. S. Turner, G. Steigman and L. Krauss, Phys. Rev. Lett. **52**, 2090 (1984); S. Dodelson, G. Gyuk and M. S. Turner, Phys. Rev. Lett. **72**, 3754 (1994); M. White, G. Gelmini and J. Silk, Phys. Rev. D **51**, 2269 (1995); S. Bharadwaj and S. K. Sethi, astro-ph/9707143.

[37] J. L. Feng *et al.*, Phys. Rev. D **57**, 5875 (1998).

[38] E. G. Adelberger *et al.*, Ann. Rev. Nucl. and Part. Sci. **41**, 269 (1991); E. Fishbach and C. Talmadge, Nature **356**, 207 (1992).

[39] H-Y. Cheng, Phys. Rev. D **36**, 1649 (1987).

[40] E787 Collaboration, S. Adler *et al.*, Phys. Rev. Lett. **79**, 2204 (1997).

[41] A. Jodidio *et al.*, Phys. Rev. D **34**, 1967 (1986).

[42] R. D. Bolton *et al.*, Phys. Rev. D **38**, 2077 (1988).

[43] K. Choi and A. Santamaria, Phys. Rev. D **42**, 293 (1990).

[44] CLEO Collaboration, R. Ammar *et al.*, Phys. Rev. D **49**, 5701 (1994).

[45] ARGUS Collaboration, H. Albrecht *et al.*, Z. Phys. C **68**, 25 (1995).

[46] ALEPH Collaboration, Talk presented at the International Conference on High Energy Physics (ICHEP '96), Warsaw, Poland, 25-31 July 1996, PA10-019.

[47] Z. G. Berezhiani and M. Yu. Khlopov, Z. Phys. C **49**, 73 (1991); Z. G. Berezhiani, M. Yu. Khlopov, and R. R. Khomeriki, Yad. Fiz. **52**, 538 (1990).

[48] M. E. Peskin and D. V. Schroeder, *An introduction to quantum field theory*, Addison-Wesley Publ., Reading, MA 1995.

[49] X-Y. Pham and Q. Ho-Kim, *Elementary particles and their interactions: concepts and phenomena*, Springer Verlag, 1998.

[50] M. Wirbel, B. Stech, and M. Bauer, Z. Phys. C **29**, 637 (1985).

[51] D. Melikhov and B. Stech, Phys. Rev. D **62**, 014006.

[52] P. Colangelo *et al.*, Phys. Lett. B **395**, 339 (1997); Phys. Rev. D **53**, 3672 (1996).

[53] D. E. Groom *et al.* (PDG), Eur. Phys. J. C **15**, 1 (2000).

[54] CLEO Collaboration, Y. Kubota *et al.*, Nucl. Instrum. Methods Phys. Res., Sect. A **320**, 66 (1992).

[55] T. Hill, Nucl. Instrum. Methods Phys. Res., Sect. A **418**, 32 (1998).

[56] CLEO Collaboration, C. Bebek *et al.*, Nucl. Instrum. Methods Phys. Res., Sect. A **302**, 261 (1991).

[57] R. Brun *et al.*, GEANT 3.15, CERN Report No. DD/EE/84-1, (1987).

[58] J. Fast *et al.*, "*Rare-B hadronic analysis standards*", CBX 98-41 (1998), (CLEO internal).

[59] G. C. Fox and S. Wolfram, Phys. Rev. Lett. **41**, 1581 (1978).

[60] R. A. Fisher, "*The use of multiple measurements in taxonic problems*", Annals of Eugenics **7**, 179 (1936); M. G. Kendall and A. Stuart, *The advanced theory of statistics*, Vol. III, Chapter 44, 2nd Ed., Hafner Publishing, NY, 1968.

[61] CLEO Collaboration, D. M. Asner *et al.*, Phys. Rev. D **53**, 1039 (1996).

[62] F. Würthwein and J. Alexander, "*Details on continuum supression as used in the analysis of* $B^0 \to K^+\pi^-$ *and* $B^0 \to pi^+\pi^-$", CBX 93-41 (1993), (CLEO internal).

[63] CLEO Collaboration, D. Cronin-Hennessy *el al.*, hep-ph/0001010.

[64] B. Berger, "*Tracking efficiency studies II.*", CBX 00-32 (2000), (CLEO internal); J. Urheim, "*Track-finding study using tau decays*", CBX 99-53 (1993), (CLEO internal); K. Bloom, R. Patterson and P. Drell, "*Absolute track-finding efficiency measurements with embedded tracks*", CBX 96-101 (1996), (CLEO internal); D. Besson, "*Charged particle tracking systematic errors in* $B\bar{B}$ *events*", CBX 96-01 (1996), (CLEO internal).

[65] CLEO Collaboration, M. Artuso *et al.*, Phys. Rev. Lett. **75**, 785 (1995); D. Cinabro *et al.*, "*A search for* $B^- \to \tau^-\nu_\tau$", CBX 94-55 (1994), (CLEO internal); G. Brandenburg, "*A search for the leptonic decays* $B \to \mu\nu_\mu$ *and* $B \to e\nu_e$" CBX 95-13 (1995), (CLEO internal).

[66] CLEO Collaboration, J. P. Alexander *et al.*, Phys. Rev. Lett. **86**, 2737 (2001).

[67] G. J. Feldman and R. D. Cousins, Phys. Rev. D **57**, 3873 (1998).

[68] CLEO Collaboration, R. Ammar *et al.*, submitted to Phys. Rev. Lett.

[69] I. Dankó, "*Search for familon in B meson decays*", Talk presented at the APS April Meeting 2000, Long Beach, CA.

[70] J. Goldstone, A. Salam, and S. Weinberg, Phys. Rev. **127**, 965 (1962).

[71] CLEO Collaboration, T. E. Browder *et al.*, Phys. Rev. D **56**, 11 (1997).

[72] D. Atwood, G. Eilam and A. Soni, Mod. Phys. Lett. **A11**, 1001 (1996); G. Korchemsky, D. Pirjol and T-M. Yan, Phys. Rev. D **61**, 114510 (2000).

[73] G. Burdman, T. Goldman, and D. Wyler, Phys. Rev. D **51**, 111 (1995).

[74] W.-S. Hou, Phys. Rev. D Brief Report **48**, 2342 (1993).

[75] ALEPH Collaboration, D. Buskulic *et al.*, Phys. Lett. B **343**, 444 (1995); L3 Collaboration, M. Acciari *et al.*, Phys. Lett. B **396**, 327 (1997); DELPHI Collaboration, P. Abreu *et al.*, CERN-EP/99-162 submitted to Phys. Lett. B (1999).

[76] CLEO Collaboration, T. E. Browder *et al.*, Phys. Rev. Lett. **86**, 2950 (2001).

[77] DELPHI Collaboration, W. Adam *et al.*, Preprint CERN-PPE/96-67 (1996).

[78] D. Cowen and J. Urheim, "*Studying* $B^- \to \tau^- \bar{\nu}_\tau$ *using fast pions from* $\tau^- \to \pi^- \nu_\tau$.", CBX 92-118 (1992), (CLEO internal).